Charting NeuLAND: Towards multi-neutron reconstruction with the New Large Area Neutron Detector
and
The virtual γ-ray spectrometer G4Horus

Inaugural-Dissertation
zur
Erlangung des Doktorgrades
der Mathematisch-Naturwissenschaftlichen Fakultät
der Universität zu Köln

vorgelegt von
Jan Mayer
aus Bergisch Gladbach

Verlag Dr. Hut, München

2018

Berichterstatter:	Prof. Dr. Andreas Zilges Prof. Dr. Hans Ströher

Tag der mündlichen Prüfung: 23. Oktober 2018

ABSTRACT

This thesis presents work on the New Large Area Neutron Detector NeuLAND, which will be used at the upcoming Facility for Antiproton and Ion Research (FAIR), Germany. Assembly steps for detector modules are described, followed by experiments performed with the NeuLAND Demonstrator in Japan. The detector is also assembled virtually for Monte Carlo simulations, including a conversion process from energy depositions to experimental look-alike events. This detector response is in good agreement with experimental data from Japan. Performance and behavior of newly developed reconstruction methods are mapped out for different detector sizes. These algorithms can reconstruct multiplicity and primary interaction points for many incoming neutrons. In addition, the groundwork for event reconstruction with neural networks is laid.

In the second part, the GEANT4 application G4Horus is presented, which implements a virtual version of the HORUS γ-ray spectrometer used at the Institute for Nuclear Physics, University of Cologne. The high purity germanium (HPGe) detectors in this spectrometer are often used to measure γ-rays from 5 MeV to 10 MeV. No standardized calibration sources are available at these energies, and the efficiency calibration is challenging. G4Horus alleviates this problem with easy to use efficiency simulations. More complex experiments with particle detectors and respective data analysis procedures can be understood and improved with matching simulations. Here, G4Horus provides listmode data with simulated particle-γ coincidences.

Zusammenfassung

In dieser Dissertation werden Arbeiten an dem New Large Area Neutron Detector NeuLAND vorgestellt, welcher in der Facility for Antiproton and Ion Research (FAIR), Deutschland, zum Einsatz kommt. Die Montage der Detektormodule und Experimente mit dem NeuLAND-Demonstrator in Japan werden vorgestellt. Für Monte-Carlo-Simulationen wurde der Detektor auch virtuell aufgebaut, wobei insbesondere ein Umwandlungsprozess von einzelnen Energiedepositionen zu Ereignissen mit experimentellem Charakter bedeutend ist. Diese Detektorantwort ist in guter Übereinstimmung mit experimentellen Daten aus Japan. Weiterhin wurden Leistung und Verhalten von neu entwickelten Rekonstruktionsmethoden für unterschiedliche Detektorgrößen untersucht. Diese Algorithmen können Anzahl und primäre Interaktionspunkte für viele eingehende Neutronen rekonstruieren. Zudem wurde der Grundstein für die Ereignisrekonstruktion mit neuronalen Netzen gelegt.

Im zweiten Teil wird die Geant4-Anwendung G4Horus präsentiert, eine virtuelle Version des HORUS γ-Spektrometers, welches am Institut für Kernphysik der Universität zu Köln verwendet wird. Die hochreinen Germaniumdetektoren (HPGe) in diesem Spektrometer werden häufig zur Messung von γ-Strahlen zwischen 5 MeV und 10 MeV benutzt. Bei diesen Energien stehen keine standardisierten Kalibrierungsquellen zur Verfügung, was die Effizienzkalibrierung zu einer Herausforderung macht. G4Horus kann diese mit einfach zu bedienenden Effizienzsimulationen verbessern. Darüber hinaus können komplexere Experimente mit Teilchendetektoren und entsprechenden Datenanalyseverfahren mit passenden Simulationen verstanden und verbessert werden. Hierfür stellt G4Horus Daten mit simulierten Teilchen-γ-Koinzidenzen zur Verfügung.

CONTENTS

PREFACE

Detectors are vital for nuclear and particle physics. For their discovery of the atomic nucleus, Rutherford, Geiger, and Marsden used a zinc sulfide scintillator as detector and their eyes as data acquisition [1, 2]. Since then, detection systems have evolved enormously, and with them our knowledge of matter.

Particle interactions are often not deterministic but statistically distributed. For example, it is not possible to predict where, how, or even if a single γ-quant will interact with the medium it passes through. Given many γ-rays however, one can show that the intensity decreases exponentially with larger distance. Other particles with multiple possible decay paths and various possible reactions in different materials form systems too complex to describe analytically.

Monte Carlo simulations can overcome these limitations: "A Monte Carlo technique is any technique making use of random numbers to solve a problem." [3, p. 1147]. For nuclear physics, this means rolling the dice to choose an interaction. The respective interaction probabilities must be crafted to reflect reality. One might say: God does roll the dice. We can build our own dice and check if they match.

Computer codes like GEANT4 provide interaction implementations which have been proved and tested and used for many experiments [4]. In this thesis, two detector systems for uncharged particles are investigated with Monte Carlo methods: The neutron detector NeuLAND and the γ-ray detector array HORUS.

PART I.

CHARTING NEULAND: TOWARDS MULTI-NEUTRON RECONSTRUCTION WITH THE NEW LARGE AREA NEUTRON DETECTOR

> “We have no interest in simply making something just
> twice as good as an existing thing.
> We desire 10, 100, 1000 times better.”
>
> *Paolo Giubellino*[a]

---

[a] During his talk *Status of the FAIR Project* [5]

CHAPTER 1.

INTRODUCTION

Once completed, the New Large Area Neutron Detector NeuLAND will allow to detect high energy neutrons between 100 MeV to 1000 MeV with outstanding capabilities in terms of efficiency and resolution [6].

Once completed, it will be used for the *Universe in the Laboratory*: The Facility for Antiproton and Ion Research (FAIR), located in Darmstadt, Germany [7]. At FAIR, radioactive ion beams produced by in-flight projectile fragmentation are separated by the Super-FRS fragment separator [8, 9]. These beams drive experiments researching NUclear STructure, Astrophysics, and Reactions (NUSTAR) [10–12]. Other scientific pillars of FAIR are antiproton interactions (PANDA) [13, 14], atomic and plasma physics (APPA) [15], and compressed baryonic matter (CBM) [16, 17]. One major part of NUSTAR is the Reactions with Relativistic Radioactive Beams (R^3B) program, where NeuLAND provides high-resolution time-of-flight neutron spectrometry at high efficiency with its $19\,\mathrm{m}^3$ of active scintillator.

This part of the thesis deals with the construction and performance of NeuLAND in hardware and software. First, the manufacturing process of the detector elements is described in Chapter 2. Several experiments at GSI (Germany) and at RIKEN (Japan) utilized these elements, a short overview is presented in Chapter 3. The focus in Chapter 4 lies on Monte Carlo simulations, which are embedded in the software and data flow concepts. In Chapter 5 and Chapter 6, the simulation itself, its post-processing, and the comparison to experimental data is discussed. Traces left behind by neutron interactions, gathered in clusters (Chapter 7), can be exploited for event reconstruction in different ways.

As only parts of the detector will be available for the upcoming experiments in FAIR Phase 0, the feasibility of several experiments is at risk. Within the scope of this thesis, methods for multi-neutron reconstruction have been developed and analyzed for the full and partial detector. These different reconstruction algorithms are discussed in Chapter 8. In addition, first experiments with neural networks for event reconstruction were performed, see Chapter 9.

1.1. The R^3B experiment

In the upcoming R^3B experiment, short lived exotic isotopes far away from stability can be studied in inverse kinematics with beam energies up to 1 GeV per nucleon. The broad physics program includes many different topics: The evolution of the collective response of exotic nuclei, the dipole strength at the particle threshold, unbound states and multi-neutron configurations in exotic systems, and others. An in-depth presentation of the science cases is given in [7].

The setup for the experiments in FAIR Phase 0 is shown in Figure 1.1. It is based on the experience with the predecessor setup R^3B/LAND [18, 19] and composed of many independent detectors. The ensemble allows to measure reactions with complete kinematics. The beam is tracked by a thin scintillating start detector before it impinges on the main reaction target, for example a large liquid nitrogen target for (p,2p) reactions or a lead target for Coulomb excitation. Some fragments, mostly protons, diverge from the beam axis and are detected by the Si-Tracker just behind the target. In addition, the CALIFA calorimeter surrounds the target and measures light particles and γ-rays [20]. Beam like heavy fragments and fast protons are bend away from the 0° axis by the superconducting dipole magnet GLAD and tracked with a set of scintillator fiber detectors and scintillator walls. The chargeless neutrons are unaffected by the magnetic field and follow the strait path until they hit NeuLAND.

The invariant mass method is often used with this type of setup [22]. For example, the relative energy E_{rel}, which is the invariant mass minus the sum of the rest masses,

$$E_{rel} = \left(\left| \sum_i \mathbf{P}_i \right| - \sum_i m_i \right) c^2, \tag{1.1}$$

is a measure for the decay energy of unbound states. For the invariant mass, the four-momenta $\mathbf{P}_i$ of all participating particles must be known — in the case of neutrons, this is the role of NeuLAND.

1.2. NeuLAND

NeuLAND is built out of organic scintillator bars with a square profile of 5 cm by 5 cm and a length of 250 cm [6]. At both ends, a conic taper over 10 cm allows the connection of a photomultiplier tube. The bars are arranged to so-called double planes: 50 horizontal and 50 vertical bars create a face area of 250 cm by 250 cm. Construction details are presented in Chapter 2. The final detector will consist of 30 double planes with a total of 3000 scintillator bars and 6000 channels.

The momenta of neutrons are determined via time-of-flight measurements: Thin detectors in front of the target give a start signal to the system. From the time difference to the detection

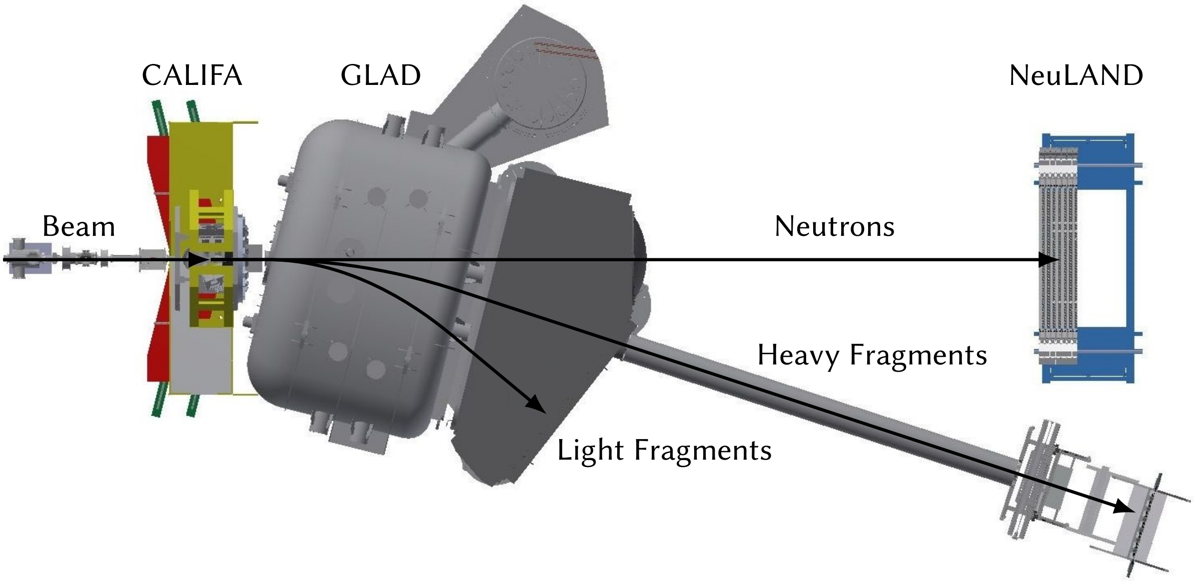

FIGURE 1.1.: The R^3B setup in FAIR Phase 0: The beam, coming from the left, hits the target surrounded by the CALIFA demonstrator. The superconducting dipole magnet GLAD bends the charged reaction products into a vacuum chamber. Protons and other light particles are detected by detectors inside the vacuum chamber. Beam-like heavy fragments continue through a pipe and hit several tracking detectors. Neutrons are detected by NeuLAND. (Adapted from D. Körper, 2018. Used with permission [21].)

in NeuLAND, the four-momenta and kinetic energy of neutrons can be obtained. Here, the kinetic energy determined by the time-of-flight is referred to as E_{ToF}:

$$E_{ToF} = (\gamma - 1)m_n c^2 \tag{1.2}$$

In the predecessor LAND [18], passive iron sheets increased the conversion from neutrons to detectable, charged particles. The scientific requirements on momentum resolution for the new R^3B setup translate into a spatial resolution of $\sigma_{x,y,z} \leq 1.5\,\text{cm}$ for NeuLAND, which lead to the highly granular design of fully active material. Together with an absolute time resolution of $\sigma_t \leq 150\,\text{ps}$, excellent excitation-energy resolutions can be achieved. The resolution depends on the flight distance and the beam energy. At the high energy setup at FAIR, the distances between the target and NeuLAND can vary from 14 m to 35 m.

Full reconstruction of events with several neutrons is a key feature of NeuLAND. One main physics motivation and simulation test case is the reconstruction of excitation energies for very exotic heavy nuclei like ^{132}Sn and beyond with high accuracies and the search for possible tetra-neutron configurations, which require the individual detection of all four neutrons with high precision [6].

Chapter 2.

Construction

The NeuLAND detector consists out of independent, self-contained units called *double planes*. Each double plane contains 100 scintillator bars, also called *paddles*, which are mounted in a frame and equipped with photomultiplier tubes at each end. Several teams from the Goethe University Frankfurt, the TU Darmstadt, the University of Cologne and the GSI itself manufactured the detector elements over several years. At the time of writing, 11 out of the 30 planned double planes have been produced, with two more under construction.

The assembly process can be split into four tasks, of which the first three can be completed independently. These tasks are described in this chapter, forming a sufficiently extensive how-to guide. All tasks are labor intensive and exceedingly repetitive but can and must be optimized to a high degree.

2.1. Paddle quality tests

The paddles are made from organic RP-408 (BC408 equiv.) plastic scintillator, wrapped in a reflective aluminum foil and a black tape finish. *Rexon Components Inc.*[1] (Cleveland, Ohio) and Eljen Technology[2] (Sweetwater, Texas) manufacture these bars to order.

Each individual scintillator is tested at GSI for light generation and transmission: An LED is embedded in a soft, transparent plastic pad on a photo multiplier dud and mounted dry to one end of the scintillator. A real photo multiplier is mounted with optical gel at the other end. Each paddle end must be cleaned and overlapping wrapping removed beforehand. The mounts are connected using four ropes with springs, pressing both apertures firmly against the paddle. Data is taken until enough statistics is achieved (less than 10 min). Figure 2.1 shows a resulting pulse height spectrum, in which two peaks can be identified: A narrow peak at high energy from the pulsed LED and a wide, low intensity peak below from cosmic muons.

---

[1] `http://www.rexon.com`

[2] `http://eljentechnology.com`

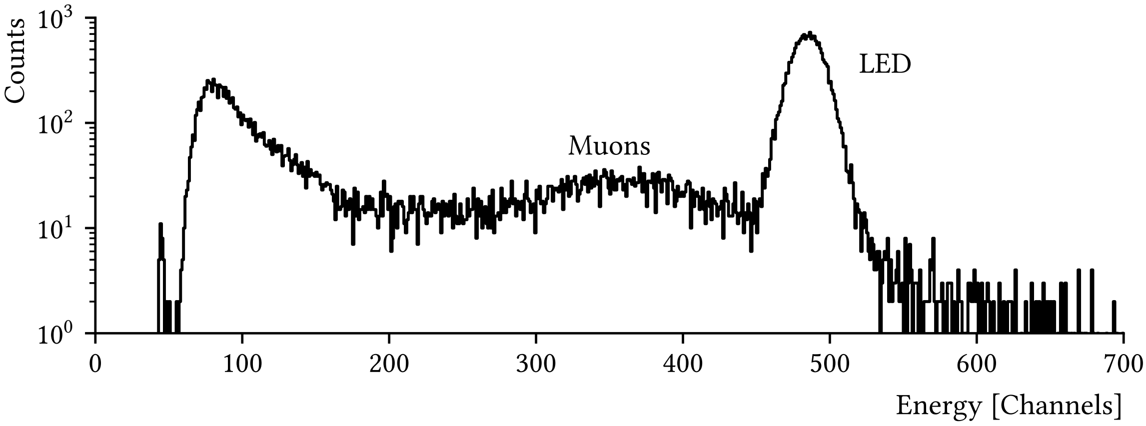

FIGURE 2.1.: Typical paddle quality test spectrum. Muon and LED peaks are fitted, and their positions compared to a recently measured standard paddle spectrum.

The peak positions in the spectrum correspond to light transmission and emission, respectively. As the system is not calibrated, the measured peak positions are compared to a reference paddle. After about five paddles, the reference paddle is measured again to account for possible shifts in the detection system.

A single person can handle the measurement process, preparing the next paddle and evaluating spectra while the data acquisition is running. A full cycle can be handled per hour, contributing over 20 man-hours per double plane. The paddles are sorted by light emission, with the best placed in the center of the double planes.

From 2012 to 2014, paddle quality was often insufficient, see Figure 2.2. Early 2014, almost 90 bars had to be rejected (production dates 2013-08 and 2014-01) after light emission measurements with cosmic muons were introduced as the main site acceptance test criterion [23]. Test processes on manufacturer side were adjusted, and no bar had to be rejected from the last deliveries. However, quality still varies between 120% to 160%, thus tests will remain necessary.

2.2. PHOTOMULTIPLIER PREPARATION

The photo multiplier tubes (PMTs) are purchased effectively off-the-shelf from the Japanese manufacturer *Hamamatsu Photonics*[3] (Hamamatsu, Shizuoka). They consist of the tube itself, housing photo cathode and dynodes under vacuum, and two compact electronics boards connected via long voltage-distributing rods. Slightly different types, e.g., with active base,

---

[3] `http://www.hamamatsu.com`

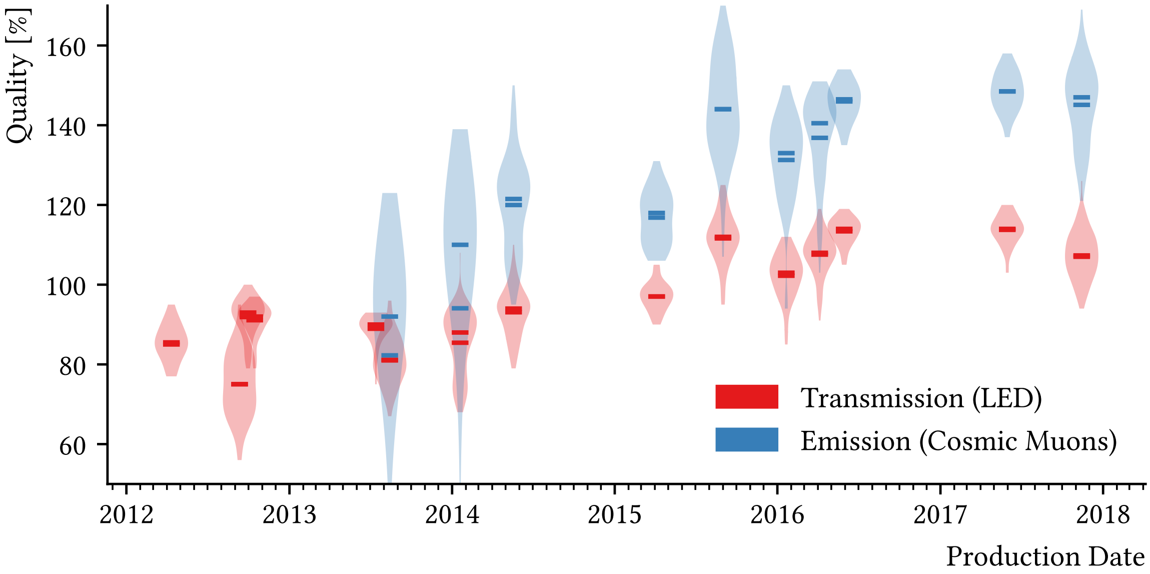

FIGURE 2.2.: Quality of 950 REXON scintillator paddles for different deliveries relative to the GSI standard paddle, with indication of mean and median values. Light emission measurements replaced the transmission test as main site acceptance factor in 2014. Early and continuous feedback to the manufacturer resulted in significantly increased light yields.

included permalloy shielding, and included 50 Ω resistor have been purchased over the years via the German distributor [23].

The devices are delivered without plug, connector, or mount. Modification for integration in NeuLAND is done at GSI, shown in Figure 2.3: First, a plastic ring, a spring, and a tube with bayonet joint are positioned on the end of the PMT. The high voltage and signal wire are pushed through a flexible plastic cap using small amounts of dish-washing detergent. The high voltage coaxial-type wire is un-insulated and split into the (still insulated) core and the mesh. The latter is twisted and re-insulated with heat-shrinking tubing. An additional piece of heat-shrinking tubing is used at the branching point. Crimped wire ferrules protect the wire endings, to which high voltage plugs are mounted. A lemo type plug is connected to the signal wire by an external contractor.

This process is repeated for each PMT. With some logistics (supplying, unpacking, and cutting of materials) and work-flow optimization (planning and distributing each step) two people can achieve a rate of up to 20 PMTs per hour, contributing another 20 man-hours per double plane. The photo multipliers are not tested before installation due to time constraints and the high quality of the delivered goods.

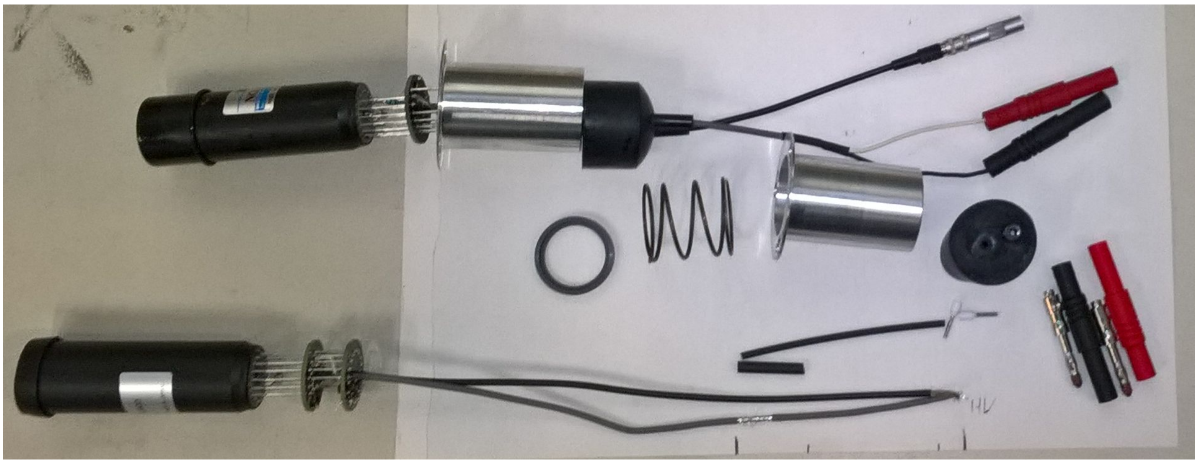

Figure 2.3.: Equipping photomultiplier tubes with mounts and plugs. The finished product (top) is created from several components (bottom). See text for details.

2.3. Frame assembly

The frame is built from aluminum plates on which socket boards are mounted. Signal cables from the boards run up to the top of the detector to the data acquisition electronics while high voltage cables are routed to the bottom to the power supplies. At a later stage, the horizontal and vertical paddles will be mounted at opposite sides of the frame. Thus, the boards are placed at opposite sides as well. This stage is by far the most time consuming one.

Four thick aluminum slabs, each with different dimensions and hole configurations, form the main frame. Once the four parts have been connected in a horizontal position on trestle legs, a crane is required for any moving operation. It is imperative to plan the steps such that the plane must be turned only once.

To start, the two side parts are placed face down. On these, the bottom and top part are placed face up and connected with screws. Plastic spacers, cable ducts, crane hangers, and several aluminum stiffeners are screwed in. In addition, paddle mounting apertures can already be installed on the parts with holes (not slits, see Figure 2.4).

A piece from the main mantle from two short and two long high voltage cables is removed such that the center of the four parts can be reached. The individual wires are sorted by the imprinted number, cut to length, soldered to the boards, and fastened with zip ties (see Figure 2.5). Insulation spray is used to finish the soldering joints, after which the boards are fastened to the spacers with plastic screws. The signal cables are sorted and bundled in the cable ducts. Once all boards have been wired, the ducts are closed. The high voltage ground phase is shared by all boards; thus, they are connected with short wires.

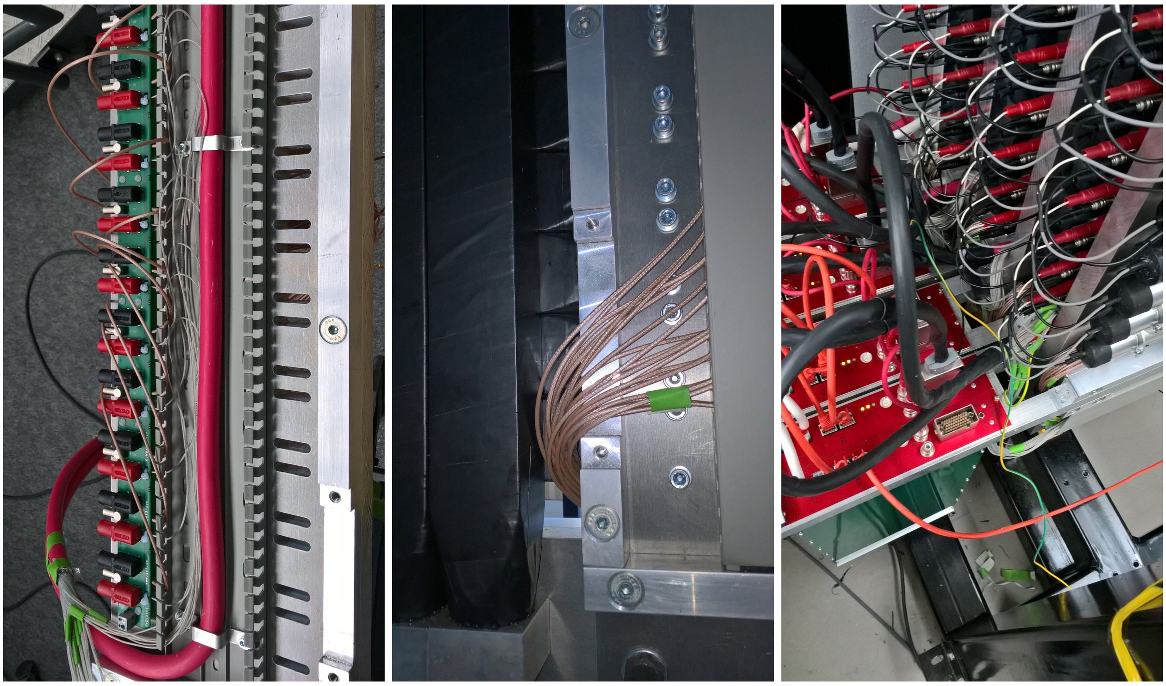

FIGURE 2.4.: Construction of NeuLAND elements: *Left:* Socketboard mounted on plastic spacers on a side next to a cable duct, with the high voltage supply for the upper corner in the center. The high voltage supply for the lower corner is split into the individual strands an soldered to the boards. On this side, slits are drilled into the metal for the mounting of the paddles to compensate for differences in the conical shapes and tape. *Center:* Lower edge of a double plane with the paddles installed. Signal cables from the bottom are fed through open small spaces to reach the top of the structure. *Right:* Several finished double planes with their high voltage supply boxes and PMTs installed and plugged into the boards. Each double plane, including all components, does not exceed 10 cm (twice the paddle thickness) to minimize the space between all paddles.

After the frame has been turned, the long high voltage cables are fastened in the side cable ducts (see Figure 2.4), and the board mounting process is repeated. The short high voltage cables are not fastened to the frame, but liberal amounts of tape can be used to hold them in place during transport. The signal cables from the bottom are guided to the sides, joined and bundled with those signal cables, and lead out on top. Plugs at the end of each signal cable bundle are installed.

Once every piece has been installed, connected and fixated, the frame can be moved to the next stage in the assembly line.

2.4. Double plane assembly

Once all components have been prepared, the double planes can be created.

The frame is moved to an upright position at the assembly station where the paddles have been sorted by quality. Paddles with the highest light output are assigned to the center of the planes, with falling quality to the outsides. A ring of black silicone is applied to the conical ends of the paddles before mounting in the paddle holders to ensure light tightness. For the horizontal paddles, thin plates incorporated between the paddles and connected to metal bands provide additional structural support to avoid sagging.

Two-component optical glue is prepared and applied to the PMTs, which then are mounted to the paddles and fixated by bayonet joints. PMTs plugs are connected to the boards, and the high voltage boxes are mounted at the bottom. As all signal cables have different lengths when exiting the cable ducts, clearing boxes are installed on top of the detector. On top of the clearing boxes, the electronic modules are positioned, with cable management rails guiding the wires. The completed planes are suspended on a rail system, see Figure 2.6.

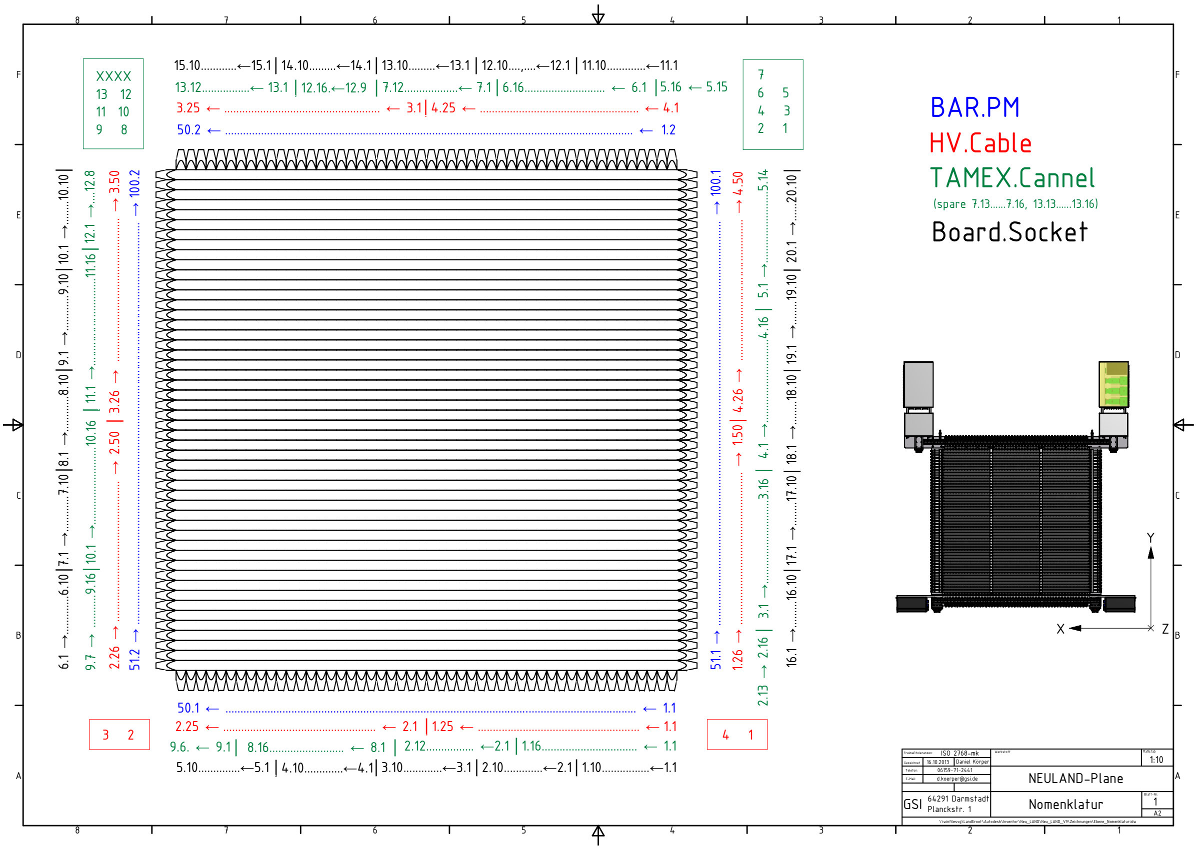

FIGURE 2.5.: NeuLAND nomenclature design sheet. High voltage (red) is supplied for each corner, covering 25 bars per side per bunch. As a result, the two high voltage distributors on each side exactly supply their side of the double plane. Signal cables (green) are bunched in groups of 8 to match the plugs and sockets used in the data acquisition front ends. Here, some bunches exist with channels from two sides combined. (Technical drawing by D. Körper, 2013. Used with permission [21].)

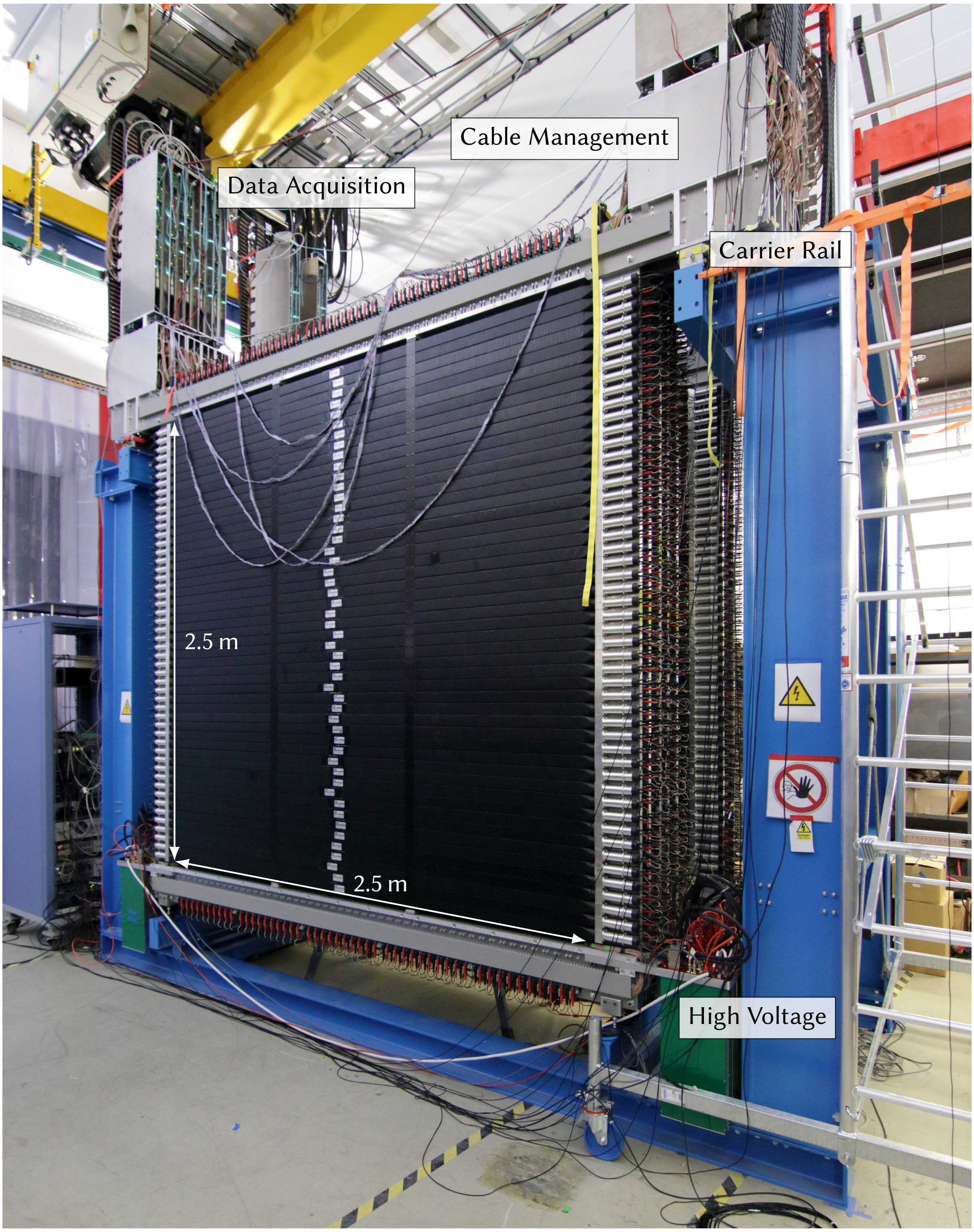

Figure 2.6.: Several finished NeuLAND double planes in the experimental area. (Adapted from K. Boretzky, 2018. Used with permission [23].)

Chapter 3.

Experiments

Parts of NeuLAND have been used at GSI before the facility was shut down for upgrades. Afterwards, four double planes, the so-called NeuLAND demonstrator, were transported to Japan for an experimental campaign at the Radioactive Ion Beam Facility at the RIKEN Nishina Center, Tokyo. In the meantime, the planes were brought back to GSI for the upcoming experiments in FAIR Phase 0.

3.1. Experiments performed at GSI

Four experiments with NeuLAND parts have been performed before the shutdown: S406 and S438a-c, see Table 3.1. In S406, 150 scintillator bars were arranged to a cube, aiming for a reasonable detector depth with a limited number of modules, only. In this beam time, neutrons from quasi-free breakup of deuterons with energies between 200 MeV to 1500 MeV were detected [24, 25]. In S438a, performed in April 2014, one double plane was used to detect neutrons from Coulomb breakup of ^{58}Ni. In October 2014, four double planes and two half-finished “single planes” were used in a commissioning experiment followed by the last physics beam time with the old R^{3}B setup, studying fission of heavy elements after Coulomb excitation [26]. For the last experiment, NeuLAND was not required but neutrons were observed parasitically.

3.2. Experiments performed at RIKEN

After the test experiments performed at GSI, the NeuLAND demonstrator was shipped to Japan. It was integrated in the SAMURAI setup at the Radioactive Ion Beam Factory (RIBF) at the RIKEN Nishina Center in Tokyo [27–29]. The SAMURAI setup is comparable to the R^{3}B setup, as its main component is also a large dipole magnet to separate exotic isotopes. For most experiments, NeuLAND was combined with the existing NEBULA detector for neutron detection at 0°. A total of 12 experiments with 71 days of beamtime were performed, a list of the experiments is given in Table 3.1, see [30] for details. The experiments in 2015 and

2017 were assisted as part of this thesis. In Section 6.4.2, data recorded in 2015 is compared to simulations performed with the software described in the next chapters.

3.3. UPCOMING EXPERIMENTS IN FAIR PHASE 0

For the upcoming FAIR Phase 0, several scientific proposals using the R^{3}B setup have been accepted. Three experiments have been scheduled for late 2018: A commissioning experiment which will not be used directly for NeuLAND and two production experiments. In the first, the standalone detection of one to three neutrons is essential; while in the second, NeuLAND is not required. At least 7 and up to 15 double planes are expected to be fully operational for these experiments.

TABLE 3.1.: Experiments with different configurations of NeuLAND at GSI [24, 25, 31], with the NeuLAND demonstrator at the SAMURAI setup at RIKEN [30], and scheduled experiments at GSI-FAIR in 2018.

	Year	Experiment	NeuLAND	Days
GSI	2012	S406: Calibration with Deuterons	150 bars	
	2014	S438a: R^{3}B Commissioning (^{58}Ni)	1 dp	5
		S438b: R^{3}B Commissioning (^{48}Ca)	2 sp + 4 dp	7
		S438c: SOFIA campaign (Coulex fission of U, Tl, Bi, Fr)	2 sp + 4 dp	8
RIKEN	2015	IMPACT campaign (transmutation studies)	4 dp	
		^{7}Li(p,n): 1n efficiency at 110 MeV & 250 MeV	4 dp	1
		^{28}O & ^{27}O spectroscopy	4 dp	11.5
		Sπrit TPC – EOS experiment	4 dp	12
	2016	^{31}Ne Coulomb breakup & knockout	4 dp	3.5
		Nucleon removal reactions around N=16 shell closure	4 dp	3
		Lifetime of ^{26}O ground state	4 dp	4
	2017	Dipole response of n-rich Ca isotopes	4 dp	7
		SEASTAR-3 (n-rich isotopes in K – V region)	4 dp	8
		Dipole response of light, dripline nuclei (^{6,8}He)	4 dp	6
		Study of tetraneutron system using ^{8}He(p,pα)4n	4 dp	8.5
		Study of tetraneutron system using ^{8}He(p,2p)^{7}H	4 dp	6.5
FAIR	2018	S444: R^{3}B Commissioning	7-15 dp	5
		S473: Measurements of accurate cross sections with R^{3}B	7-15 dp	5
		S454: Studying the astrophysical reaction rate of ^{12}C(α,γ)^{16}O	7-15 dp	3

CHAPTER 4.

SOFTWARE AND DATA FLOW

Raw data collected in an experiment must be processed and analyzed to extract the physics quantities of interest. This process is not trivial and requires dedicated software. In addition, simulations are required to characterize and optimize the experimental setup even before the experiment is performed and to understand the gathered data. This software must be crafted with the same care as the physical detectors to be able to perform its task well and for many years.

For the experiments at FAIR, a holistic approach is taken: Both data analysis and simulation are performed with the same software. The main principle utilized is that after calibration of the experimental and digitization of the simulated data, the properties of both should be the same. Reconstruction algorithms can then be applied to both, and, in case of simulated data, compared with the input. Thus, the full data analysis stack can be constructed and tested beforehand, see Figure 4.1.

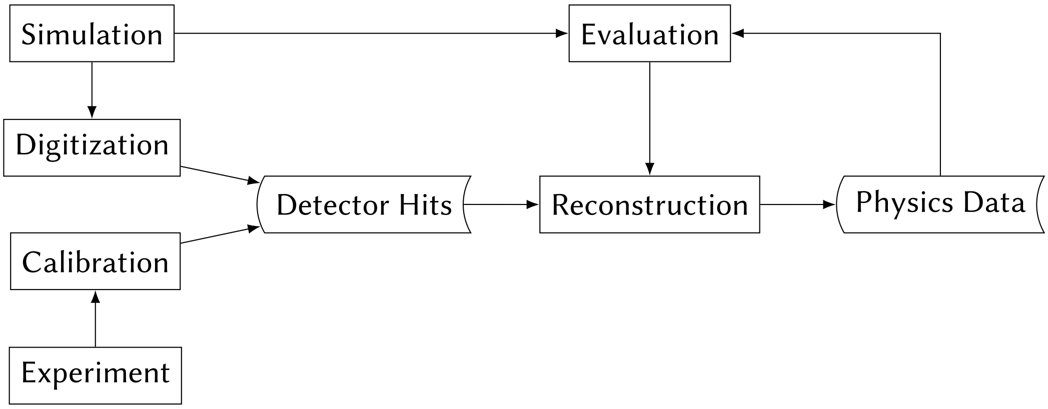

FIGURE 4.1.: Generalized data flow scheme of R3BRoot. Raw experimental and simulated data are processed to detector hits which are then reconstructed to extract the physical data. As the correct result is known in the case of simulation, the effectiveness of the reconstruction stage can be evaluated.

4.1. PRIOR AND RELATED WORK

Since 1990, the LAND detector has been used with the ALADIN magnet in the R^{3}B setup at GSI [18]. For its data processing, the `land02` package was used [32, 33]. It was originally developed by Håkan Johansson and further supported by Ralf Plag and is a predecessor of R3BRoot.

Some simulation and analysis parts for the LAND detector were partially implemented in R3BRoot between 2009 and 2011. For the creation of the NeuLAND technical design report [6], these old LAND classes were re-purposed and modified without properly separating the concerns of both detectors.

In addition to the TDR, some simulations were performed before this work, most notably the evaluation of S406 [25], studies of the background in S438 (K. Miki), and the effect of the photomultiplier saturation [34].

For future experiments over the next decades, a clean code base was desired. Work on software was divided into several parts:

- Reading and calibration of experimental data up to hit level (V. Wager [35])
- Simulation and digitization of hit level data (this work)
- Research and implementation of event reconstruction algorithms (this work)
- Simulation and feasibility studies for a veto detector (C. Douma [36])

Notable other related works are `ggland` [37] and `smsimulator` [38], both standalone GEANT4 packages for simulation of R^{3}B/LAND and the Japanese NEBULA detector, respectively.

4.2. FAIRROOT AND R3BROOT

For the experiments performed at FAIR, the common software framework FairRoot has been developed since 2003 [39]. It provides the base for analysis and simulation of the individual experiments, like CBM and PANDA. R3BRoot is the respective derived software for the R^{3}B experiment, in which individual detectors, including NeuLAND, and their respective analysis methods are implemented.

FairRoot, as the name suggests, heavily relies on ROOT and associated programs. Its dependencies are bundled under the FairSoft project, which includes GEANT3, GEANT4, ROOT, Virtual Monte Carlo, Pythia, and many others. This common installer for all dependencies ensures that every installation is identical, and, hence reproducibility of the results.

FairRoot provides the core services for detector simulation and analysis by providing C++ interface classes, from which the actual implementations derive. These derived classes can then be supplied to the core management classes. Thus, the code for the experiments does not need to worry about mundane tasks like handling input/output files and parameter storage. Neither FairRoot nor the individual experiment codes deliver an actual executable program. Instead, the code is compiled to shared libraries which are then loaded and steered in ROOT macros for maximum flexibility without recompilation.

Additional benefits are the interchangeability of code and, more importantly, developers between the experiments. All depended experiments also profit from common future developments, e.g., advanced multiprocessing over multiple servers and message-based data flow [40]. FairSoft[1], FairRoot[2], and R3BRoot[3] have been released as open source. FairSoft version `oct17p1` (with Geant4 `10.02.p1`), FairRoot `v-17.10b`, and custom versions of R3BRoot were used for the results presented here.

4.3. NeuLAND in R3BRoot

NeuLAND, as all other detectors used in the R^3B experiment, must be available in R3BRoot. In the scope of this thesis, the required classes were implemented, tested, and analyzed.

The work can be grouped into overarching modules which will be discussed in the next chapters: Chapter 5 deals with the implementation of the simulation itself and the properties of primary neutron reaction products in NeuLAND. The energy depositions of these reaction products are then digitized and compared to experimental hits in Chapter 6. These hits are then grouped together to form clusters whose properties are discussed in-depth in Chapter 7. Finally, Chapter 8 deals with various approaches to reconstruct the primary neutron interaction points and neutron multiplicity.

In Figure 4.2, an overview over the components and the internal data flow is given.

The actual Monte Carlo simulation is coordinated by `FairRunSim` which requires the geometry, the primary particles, and the Monte Carlo engine with its physics implementation. During the simulation, a huge amount of data is produced while every single created particle is tracked on its path through the matter. These tracks could be saved in their entirety, but this is rarely used due to the enormous data size, easily producing tens of gigabytes. Instead, the classes responsible for providing the detector geometry to the coordinating class grab and save only the information of interest from the data stream. For NeuLAND, the individual energy depositions in the active volumes are extracted as so-called `R3BNeulandPoints`. In addition, information about the reactions taking place inside NeuLAND can be extracted to

---

[1] `https://github.com/FairRootGroup/FairSoft`

[2] `https://github.com/FairRootGroup/FairRoot`

[3] `https://github.com/R3BRootGroup/R3BRoot`

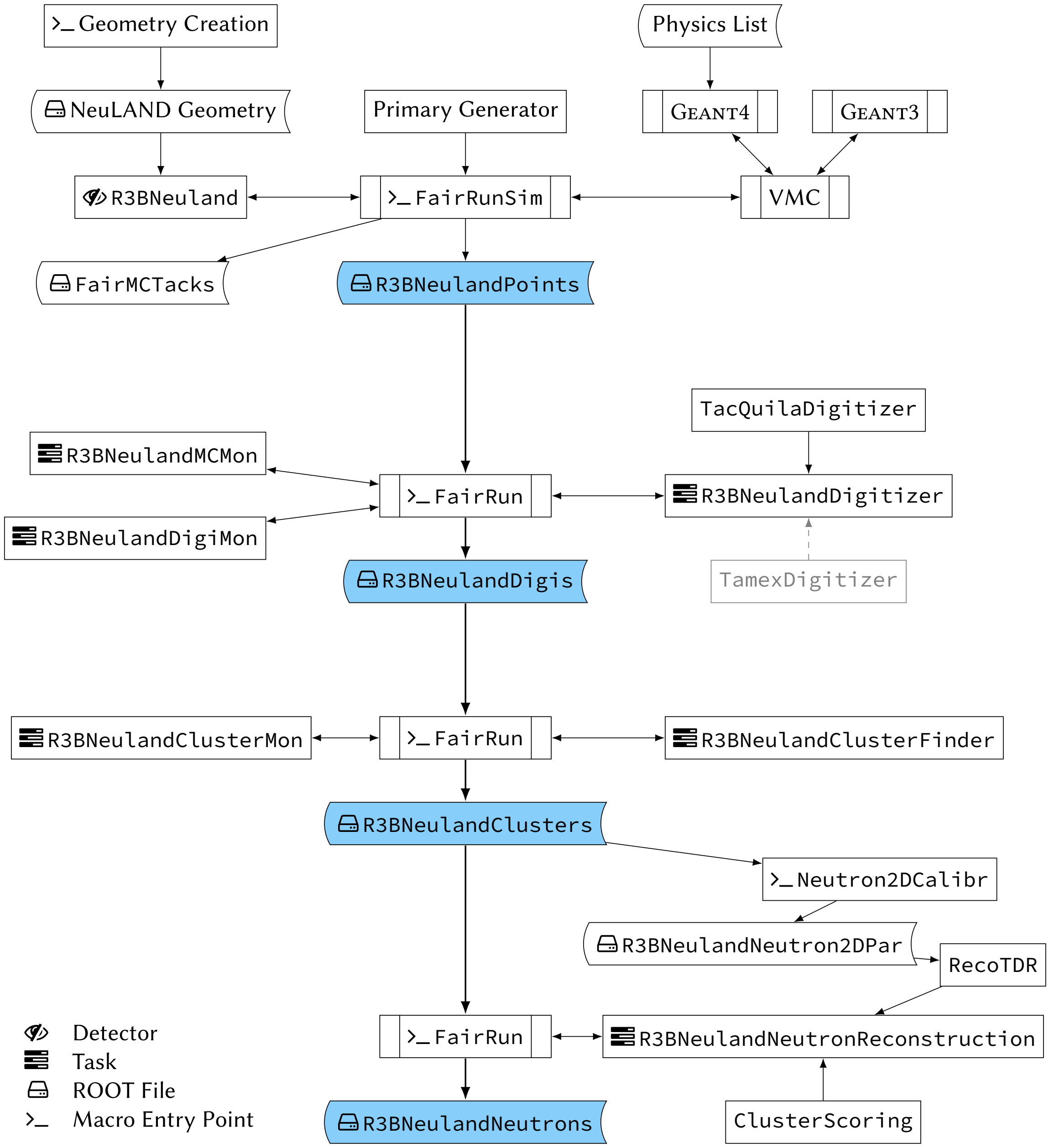

FIGURE 4.2.: Overview over the simulation and reconstruction process in R3BRoot. The main simulation session is managed by the `FairRunSim` class, which is supplied with the primary particle generator, the detectors and their geometry, and the Monte Carlo engine to use, including the physics list. The simulation produces, amongst other data, the `R3BNeulandPoints`, which are digitized in a separate session using a digitizer task. The individual components are discussed in the next chapters.

gain a first impression of the challenges and possible starting points for event reconstruction ideas.

These `R3BNeulandPoints`, whose numbers can be in the thousands, are then collected per detector element. The response of this element and its data acquisition is applied in a process called *digitization* which produces detector hits (`R3BNeulandDigis`). For each generation of data acquisition electronics, a respective `Digitizer` is required. The energy, time, multiplicity, etc., of these simulated detector hits can then be compared to experimental hits. If both the simulation and digitization are performed appropriately, the properties should match. From this point onwards, one can use simulations to run every desirable experiment virtually and observe the reaction of the detector.

NeuLAND should deliver two related but distinct types of information: The number of neutrons that have reacted in the detector, called the *neutron multiplicity*, and the interaction points and times of these interactions. This is the main challenge for NeuLAND and the most important part of this thesis. One approach to reconstructing is to group hits, which are in neighboring detector elements, to so-called `R3BNeulandClusters`. Many different algorithms can then try to use the properties of these clusters to determine the neutron multiplicity and find the primary neutron interaction points.

The result of this process are `R3BNeulandNeutrons` which contain the four-momenta of the reconstructed neutrons. All R^{3}B users can use the software developed in the scope of this thesis for data from R^{3}B/NeuLAND experiments.

CHAPTER 5.

SIMULATION

In this chapter, the Monte Carlo simulations are discussed: Primary projectiles interact with the geometry via specific physics processes, creating secondary particles and energy depositions in the material.

The interactions of primary neutrons are the focal point of NeuLAND and the simulations: Since they are uncharged, neutrons do not loose energy via electromagnetic stopping processes. Detection can only take place trough nuclear reactions and consecutive energy depositions of the secondary particles. A firm understanding of these reaction products is thus vital to understand the measured data and attempt reconstruction of the interaction points.

5.1. PRIMARY PROJECTILES

Primary projectiles are typically not generated by GEANT4 itself, but by other, user-controlled methods and then handed over to the Monte Carlo track processing. In this work, four generators have been used:

Box Generator This generator produces primary particles without any regards for actual physical processes. A random number generator picks origin, direction, and energy from user-defined ranges. This is especially useful to examine the detector response to mono-energetic neutrons over a wide energy range, see Section 5.4.

Ascii Generator External reaction kinematics codes can pre-compute sets of particles and store their momenta in text files for later use. These text files are typically quite large, as they must contain a substantial amount of different sets to provide enough statistics. The ^{130}Sn-multi-neutron test case discussed in Section 1.2 were simulated with such input files.

Phase-Space Generator Lorentz-invariant phase space has been used to generate multi-particle weighted events since the first Monte Carlo codes. The `TGenPhaseSpace` class available in ROOT is based on the old GENBOD code (W515 from CERNLIB, 1975) using the Raubold and Lynch method [41]. It is still an important basic component of many simulations (see, e.g., [42]). In the scope of this thesis, the ROOT class was

Table 5.1.: NeuLAND paddle material properties and thicknesses. Materials are simplified to their main constituents. Thicknesses are given from the center of a paddle, the total width is thus 4.94 cm.

Part	Material	Density [g cm^{-3}]	Composition	Thickness [cm]
Scintillator	RP-408 (polyvinyltoluene)	1.032	8.4% H, 91.6% C	2.4
Reflector	Aluminum alloy foil	2.7	Al	0.02
Wrapping	Adhesive black polyethylene	0.94	14.3% H, 85.7% C	0.05

wrapped in the new `R3BPhaseSpaceGenerator`[1] to be compatible with the FairRoot framework. The main advantages over Ascii files are the flexibility of input parameters and no limitation on the number of events.

Cosmic Muon Generator NeuLAND uses cosmic muons for time and energy calibration. This generator produces muons according to the energy distribution of the cosmic ray flux at sea level [43].

5.2. Geometry

Physical volumes are, in principle, the least ambiguous component in simulations. Properties of shapes and materials can be measured to high precision. Implementation in the virtual environment is straightforward for basic shapes like spheres and boxes and common materials. Complex structures, however, quickly reach unreasonable requirements of computational power and manual labor.

NeuLAND double planes do have a quite simple shape, see Section 2.4. Both implementation of the detector geometry and its usage in simulations were redone from scratch. ROOT geometry macros create the individual scintillator bars including the conic tapers at each end and the wrapping of aluminum and tape. Table 5.1 holds dimensions and materials used for these paddles. Individual paddles are arranged to form double planes which in the next step are arranged to form the NeuLAND detector volume. The resulting single assembly volume is stored in a ROOT file for later use. This process can be repeated for different numbers of double planes.

The geometry of the frame and mounting structures is not trivial. As the implementation of these parts is not required for the simulations in this thesis, they were omitted. Simulation of background from the sides, e.g., created in the heavy fragment tracking detectors, might require a more detailed description in the future. Methods to implement these parts with lower effort and high accuracy are described in Section 12.3.

---

[1] `https://github.com/R3BRootGroup/R3BRoot/pull/163`

The `R3BNeuland` class interacts with the Virtual Monte Carlo code. It is derived from the `R3BDetector` class which in turn is derived from `FairDetector`. Its responsibilities are providing the geometry and extracting desired information from the individual tracking steps.

When performing simulations, `R3BNeuland` reads the pre-compiled geometry from the file and places it at the desired spot in the simulated world. The active scintillation volume is observed, and energy depositions of the tracked particles are collected. Not the full information of each individual energy deposition step is retained. Thus, the emitted light must be already calculated here, even though the digitization class would be expected to handle this process, see Equation (6.3). Deposited energy and generated light are stored along with time, position, and paddle number in `R3BNeulandPoints`.

In addition, the NeuLAND primary neutron interaction points (NPNIPS) are recorded and stored with their exact position and time for later validation of the reconstruction. These positions are also converted to indices in a 50 by 50 by 60 grid and stored as `R3BNeulandPixels` for use in Neural Networks, see Chapter 9.

Basic tracking steps for the whole virtual environment are saved automatically by the main `FairRunSim` application.

The `R3BNeulandMCMon` class reads the stored Monte Carlo tracks, points, and NPNIPS to produce various histograms for analysis of the neutron interactions, as discussed in Section 5.4.

5.3. Monte Carlo physics

For anything to happen during the simulation, interactions between particles and material are required. Implementation of interactions are a main part of Geant4. "The physics processes offered cover a comprehensive range, including electromagnetic, hadronic and optical processes, a large set of long-lived particles, materials and elements, over a wide energy range starting, in some cases, from 250 eV and extending in others to the TeV energy range." [4]

While it is possible to pick and choose each possible interaction manually for each particle, the so-called physics lists are the standardized way of selecting the models to use: "Geant4 provides a comprehensive set of physics processes to model the behavior of particles. The user is able to choose from different approaches and implementations, and to modify or add to the set provided." [4]

Geant4 version 10.4 includes a total of 20 predefined physics lists[2]. These are mostly combinations of different models for the hadronic interactions with the same or similar models for

---

[2] `FTF_BIC`, `FTFP_BERT`, `FTFP_BERT_HP`, `FTFP_BERT_TRV`, `FTFP_BERT_ATL`, `QBBC`, `QGS_BIC`, `QGSP_BERT`, `QGSP_BERT_HP`, `QGSP_BIC`, `QGSP_BIC_HP`, `QGSP_BIC_AllHP`, `QGSP_FTFP_BERT`, `QGSP_INCLXX`, `QGSP_INCLXX_HP`, `FTFP_INCLXX`, `FTFP_INCLXX_HP`, `LBE`, `NuBeam`, `Shielding`

all other interactions. The hadronic part is delegated to different models depending on the particle energy. Variants with the `_HP` suffix use a high-precision model for neutrons below 20 MeV.

In the `QGSP_BERT` physics list, for example, the *Quark-Gluon String Precompound* (QGSP) model handles neutrons over 12 GeV, the *FRITIOF Precompound* (FTFP) model is applied from 9.5 GeV to 25 GeV, and the *Bertini Cascade* (BERT) model is used up to 9.9 GeV[3] - overlaps intended. In the comparable `FTFP_BERT` physics list, the FTFP model is used for the full high energy part.

For NeuLAND, only the "low" energy parts of the hadronic interactions ($E < 10\,\text{GeV}$) must be compared, which reduces the decision down to few models: Bertini Cascade (BERT), Binary Cascade (BIC), and Liège Intranuclear Cascade (INCL). The influence of the different models has been investigated in Section 6.4.2. An overview over the most common reactions predicted by INCLXX and BERT is given in Table A.1. For the TDR, GEANT4 9.4 was used with the `QGSP_BIC_HP` physics list [6, p. 35], while R3BRoot is now using `QGSP_INCLXX_HP` by default with recent versions of GEANT4 (10.2 and later). The comparable Japanese simulation software for Nebula/SAMURAI uses its own variant of the `QGSP_INCLXX_HP` physics list [38].

5.4. PRIMARY NEUTRON INTERACTIONS

Neutrons, in contrast to charged particles, can only interact with matter via nuclear and collision reactions. These randomly occurring processes can be described using probability theory.

For N_{in} incoming neutrons, the probability P for N_{reac} interactions is expected to be a binomial distribution

$$P\big(N_{\text{in}}, N_{\text{reac}}, p(n_{\text{DP}})\big) = \binom{N_{\text{in}}}{N_{\text{reac}}} \cdot p(n_{\text{DP}})^{N_{\text{reac}}} \cdot (1 - p(n_{\text{DP}}))^{N_{\text{in}} - N_{\text{reac}}}, \tag{5.1}$$

where the interaction probability $p(n_{\text{DP}})$ for a detector depth of n_{DP} double planes is given by

$$p(n_{\text{DP}}) = 1 - (1 - p_{\text{DP}})^{n_{\text{DP}}}. \tag{5.2}$$

The *double plane efficiency factor*, i.e., the probability p_{DP} for a primary neutron interaction in one NeuLAND double plane, only depends on the neutron energy and can be determined by simulations: Up to five primary neutrons are shot at up to 50 double planes, and the number of primary neutron interactions is extracted from the raw Monte Carlo data. Thus,

---

[3] https://github.com/Geant4/geant4/blob/geant4-10.4-release/source/physics_lists/constructors/hadron_inelastic/src/G4HadronPhysicsQGSP_BERT.cc

TABLE 5.2.: Theoretical maximum achievable efficiency ϵ_{max} for n neutrons with a kinetic energy of 600 MeV for the NeuLAND demonstrator, the range of double planes available in FAIR Phase 0, and full NeuLAND. Note that the actual achievable performance in an experiment can be significantly lower, see Chapter 8.

n	$\epsilon_{\text{max}}(n_{\text{DP}} = 4)$ [%]	$\epsilon_{\text{max}}(n_{\text{DP}} = 7)$ [%]	$\epsilon_{\text{max}}(n_{\text{DP}} = 15)$ [%]	$\epsilon_{\text{max}}(n_{\text{DP}} = 30)$ [%]
1	38	56	82	97
2	14	32	68	94
3	5.7	18	58	90
4	1.7	9.5	47	88
5	0.7	5.7	40	85

this number only reflects how many neutrons have interacted in NeuLAND, which does not necessarily mean it can be detected or even reconstructed. A fit of Equation (5.1) with p_{DP} as the only free parameter matches the simulated distributions very well. In Figure 5.1, the probability distributions at a primary neutron energy of 600 MeV are shown together. The double plane efficiency factor is proportional to the neutron reaction cross section and thus energy dependent, ranging from 10 % to 12.2 %. At 600 MeV, p_{DP} is 11.03(1) %.

While the binomial behavior is no surprise, it is important to be explicitly aware of the implications for multi-neutron events: The interaction probability for $N_{\text{in}} = N_{\text{reac}}$ is the maximum achievable detection efficiency ϵ_{max}, given in Table 5.2. As expected by the Lambert–Beer law for the attenuation of uncharged particles in media, increasing the detector depth quickly leads to diminishing returns for the detection of a single neutron.

However, for multi-neutron detection this marginal change enters in a power law. If only seven double planes are available in FAIR Phase 0, four out of four neutrons will react only in 9 % of all cases. This can be quintupled to 46 % by getting 15 double planes in operation. In addition, events where not all neutrons have reacted will occur significantly more often, which complicates event reconstruction. Any additional double plane greatly improves the situation for the detection of many-neutron events just by improving the ratio of fully detectable events. For 600 MeV neutrons, doubling the detector depth from 7 to 15 double planes increases the ratio of fully reacted to partially reacted events $P(4,4)/\sum_{0<i<4} P(4,i)$ from 0.11 to 0.88, which increases the prevalence for four-neutron detection by a factor of eight. Doubling the depth again raises this value to an excellent 7.3. This effect is even larger for the actual achievable efficiency, as described in Chapter 8.

These basic considerations of the reaction probability show that experiments targeting the prestigious detection of four-neutron events will be quite challenging with less than half the detector — without even looking at reconstruction. From this standpoint it seems well justified to target 30 double planes for the final detector depth, as proposed in the TDR.

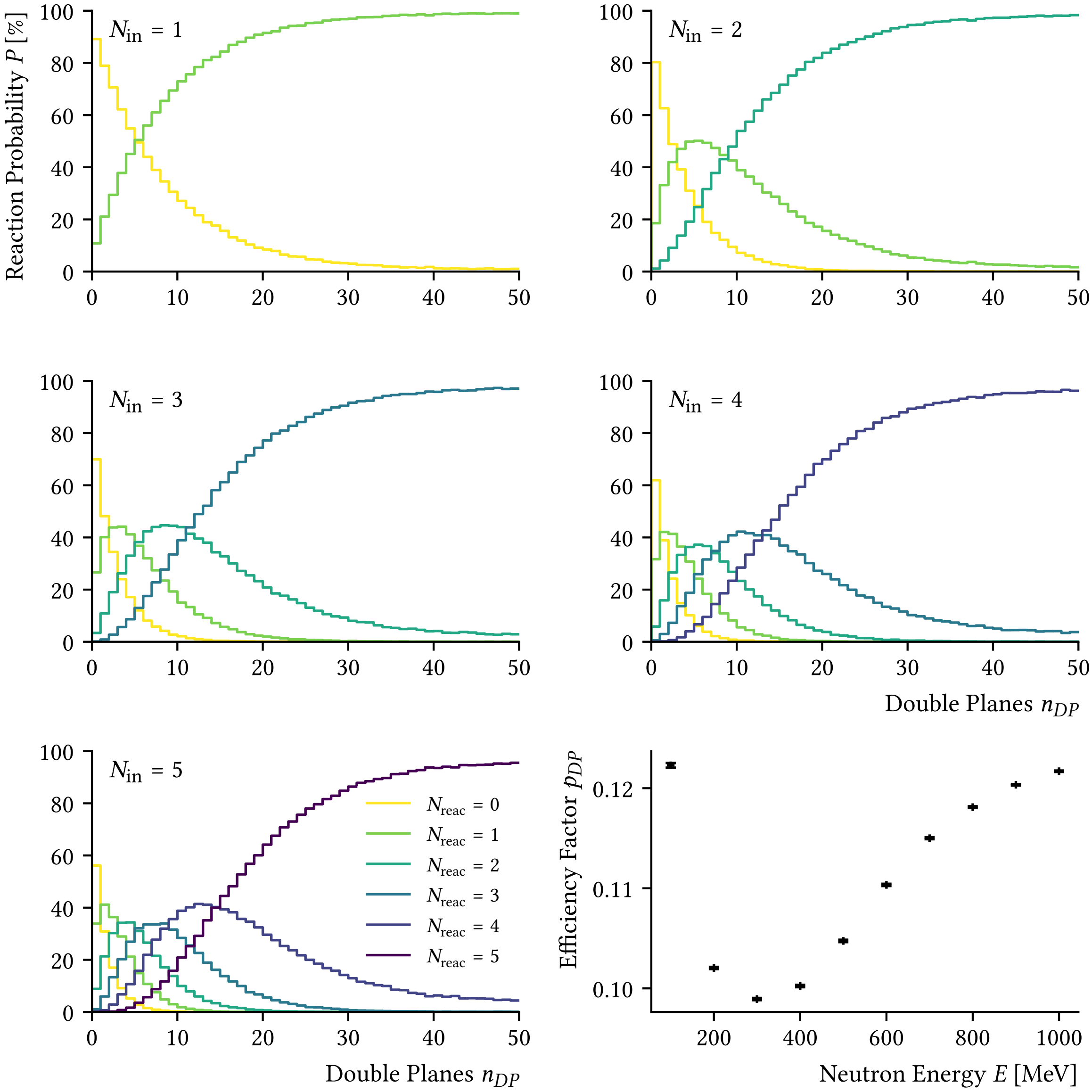

FIGURE 5.1.: Neutron reaction probability distributions as function of the number of double planes for 600 MeV and the double plane efficiency factor p_{DP} as a function of the neutron energy. For N_{in} incoming neutrons, the number of reacted neutrons N_{reac} is extracted from Monte Carlo data for each number of double planes n_{DP}. These simulated probabilities follow the expected binomial distribution (Equation (5.1)), which can be fitted with the free parameter p_{DP}. The intrinsic maximal achievable performance of NeuLAND, i.e., where all incoming neutrons undergo a reaction in the detector volume ($N_{reac} = N_{in}$), strongly rises when increasing the detector depth from 10 to 20 double planes, while at the same time suppressing unwanted channels ($N_{reac} < N_{in}$).

5.5. PRIMARY NEUTRON REACTION PRODUCTS

Neutrons at these energies can react with the paddle materials via elastic scattering, knockout, and fission reactions. Ejectile types, quantity, and energy vary widely for the relevant neutron energies from 100 MeV to 1000 MeV. Once light generation of these secondary particles is understood, approaches for reconstruction of the primary interaction points can be made. In the following, the different particles and their impact will be discussed in detail.

Primary neutrons with a kinetic energy of 600 MeV in a simulation with 500 000 events using the `QGSP_INCLXX_HP` physics list create over 8500 unique sets of reaction products (ignoring gamma rays and electrons). Most sets stem from the destruction of carbon to all possible combinations of protons, deuterons, ^{4}He, etc. The top 10 most common reactions make up 30 % to 40 % of all reactions, see Table A.1. Even more reaction types may occur in an experiment, as the simplified materials used in the simulation do not contain all elements present in, e.g., the aluminum wrapping. For different hadronic models, here for example for the Bertini cascade, the reaction sets and the respective energy depositions can be significantly different. This is further investigated with experimental data in Section 6.4.2 by applying energy thresholds on the measured hit energy.

Nevertheless, most of the reaction products can be ordered by importance:

Neutrons are the reaction products with the most impact. Reactions of primary neutrons are extremely likely to emit at least one or more neutrons – only in roughly 10 % of all cases, no neutron is emitted. On average, 1.4 neutrons are emitted per incoming neutron for 200 MeV, up to almost 2 neutrons at 1 GeV, see Figure 5.2. While most emitted neutrons have an energy of less than 50 MeV, there is a significant number of neutrons at high energies, with a peak slightly below the incident neutron energy, see Figure 5.3. These neutrons then travel further through the detector, producing more signals in secondary and tertiary reactions.

Protons are the second most common reaction product with around 1.4 protons per incoming neutron. They can also carry significant kinetic energy up to the kinetic energy of the incoming neutron, see Figure 5.3. Due to their characteristic energy loss, these high-energy protons are the most valuable particles for tracking purposes, see Section 7.4.

Alpha particles are produced around 0.8 times per incoming neutron. Their kinetic energy, however, is insignificant even for 1 GeV neutrons; the intensity drops exponentially with rising kinetic energy. This is due the possible reaction channels: Reactions producing ^{4}He often produce other heavy fragments as well, splitting the available energy.

Uncharged Particles: Primary neutron interactions produce only around 0.4 γ-rays on average, but excited secondary particles can contribute more. At higher neutron energies, $\boldsymbol{\pi^0}$ are created, which can carry high energies and decay to additional γ-rays.

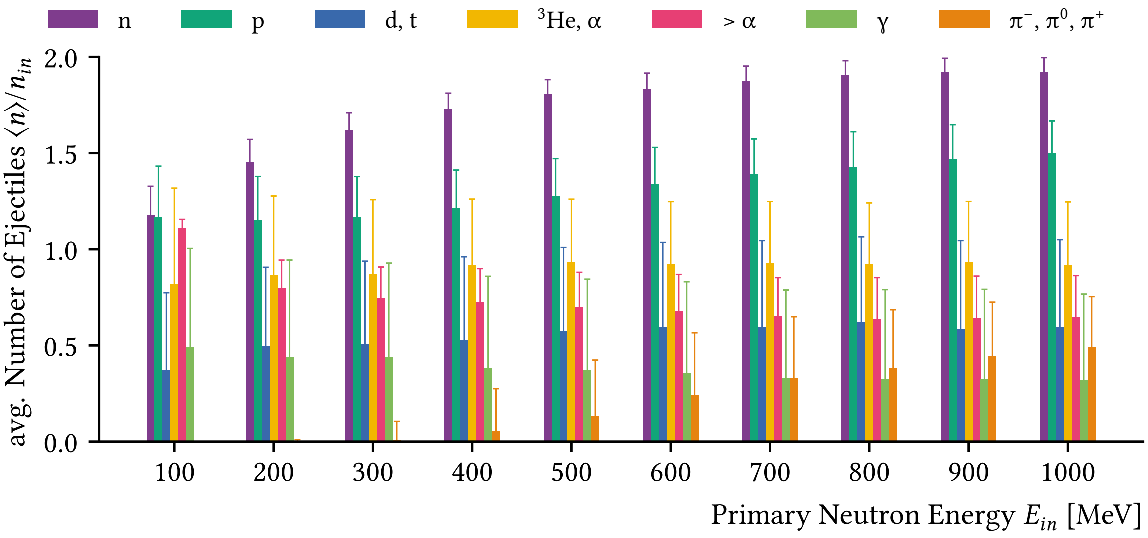

FIGURE 5.2.: Average number of reaction products from primary neutron interactions as function of kinetic energy for 30 double planes, simulated with `QGSP_INCLXX_HP`. Note that for each incoming neutron, more than one neutron is emitted, which then can react again to create even more neutrons (not shown here). The heavy reaction products (> α) mainly consist of ^{12}C.

Deuterons with high kinetic energy are orders of magnitude less common than protons, especially at high neutron energies. There is, however, a peak in intensity close to the incident neutron energy.

Pions ($\pi^{\pm}$) carry high kinetic energy with significant intensity for high neutron energies.

Heavy ions and their fragments, most notably ^{12}C from the Scintillator and ^{27}Al from the wrapping, carry low kinetic energy, and, due to their high energy loss over short distances, produce little light.

The charged particles from this list will deposit energy starting at their point of creation. As there are many particles with low energy or high mass, i.e., low range, there is a varying amount of energy deposited in clumps around the neutron interaction point. The noticeable number of protons with high kinetic energy deposit most of their energy further away in a Bragg peak.

In the next chapter, the conversion of this deposited energy to the actual measured energy in the scintillator paddles is discussed. In Chapter 8, these patterns of energy depositions are used to reconstruct the neutron interaction points.

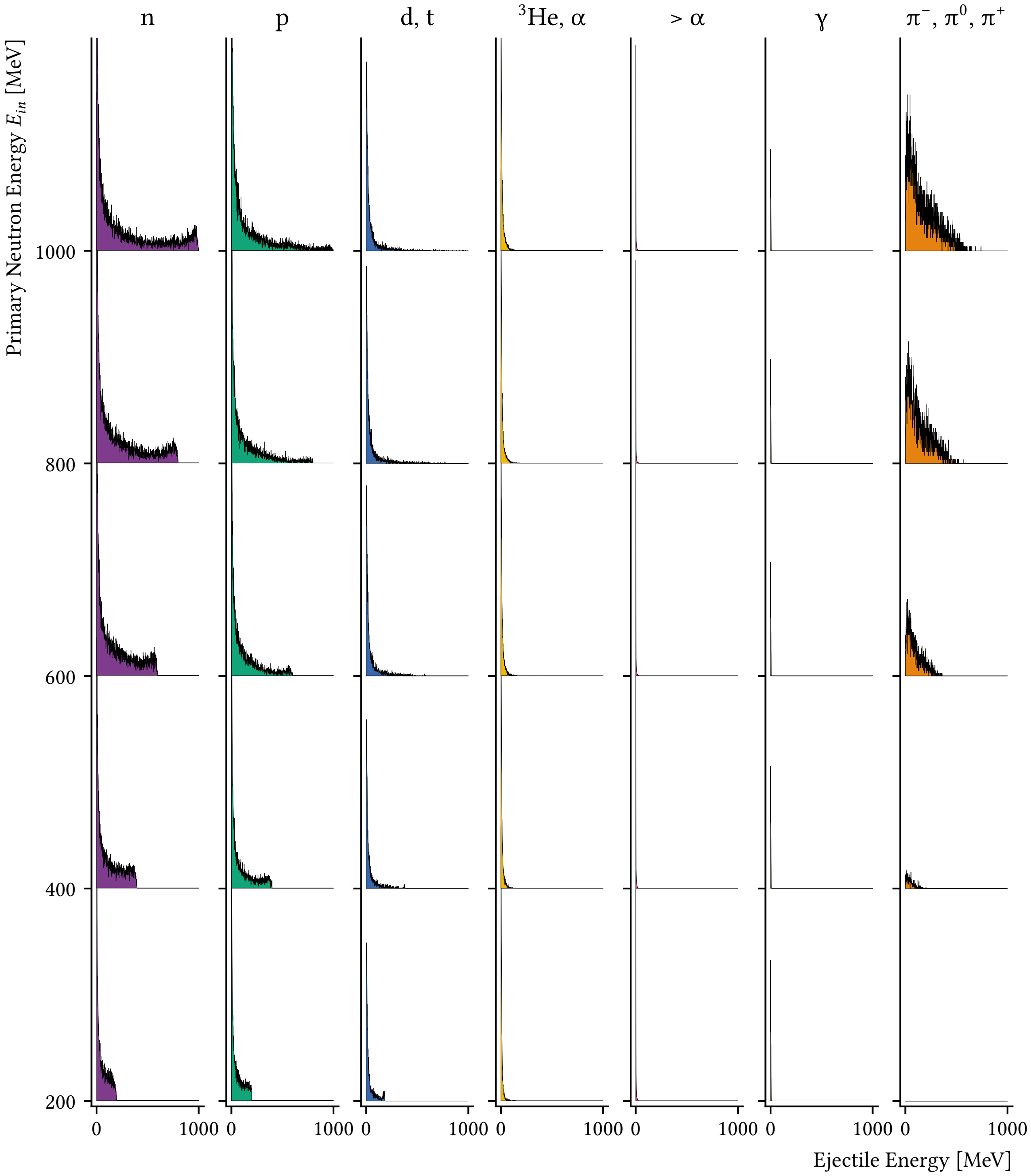

FIGURE 5.3.: Energy spectra of products from primary neutron interactions. Primary neutrons reacting in NeuLAND produce various particles with a large spread in kinetic energy. Note that low energetic neutrons and protons (<10 MeV) are emitted orders of magnitude more often (here clipping through multiple other spectra).

Chapter 6.

Digitization

Simulations must be consistent with experimental data. For NeuLAND, the comparison is based on *hit level data*, see Section 4.3. If an acceptable agreement is reached, simulations can predict outcomes for various experimental scenarios and provide insight into processes within the detector.

The Monte Carlo simulation reports individual energy depositions of particles tracked through the material. It is the digitizer's task to convert this basic information to experimental look-alike data.

To understand the steps included and omitted in the digitizer, it is required to understand the data acquisition and the experimental time and energy calibration of NeuLAND. Many components and processes transform the energy depositions on their course through the real-world detector system. These processes can be split into two groups: Physical effects in the scintillator and the photomultiplier on the one hand, and technical effects caused by data acquisition hardware and calibration software on the other — all of which must be represented adequately in the digitizer. The result is then verified with experimental data.

In the past, some confusion was caused by a misrepresentation of the calibration procedure, which resulted in an inadequate digitizer and subsequently in a degraded multiplicity resolution, see [34], and digitizer parameters far away from reasonable physical values. This could be resolved with the re-implementation within the scope of this thesis.

6.1. Processing of experimental data

During an experiment, the electronic hardware acquires an uncalibrated integer value for time and energy of the signal. If a hardware threshold is exceeded and trigger conditions are met, these values are kept, read out, and written to disk.

These raw values are then processed in several steps: First, the data is unpacked, read into R3BRoot, and assigned to the respective detector module, creating *mapped*-level data. Mapped data from a calibration run is analyzed to create parameter sets used to calculate the intermediate *cal*-level. Here, time and energy are calibrated for individual PMTs, i.e., converted from the integer value in channels to physical quantities. These calibrated detector signals are then synchronized with each other. The final hits then include global time in ns, energy in MeV, and position in cm. This procedure is part of R3BRoot, see [35] for an in-depth discussion.

Digitizers for NeuLAND could target the mapped, cal, and hit level. Throughout this thesis, hit level data is created. While lower level data could be useful to test calibration routines for experimental data, possible gains were deemed too small to warrant the required effort and increased code complexity. For example, simulated data is perfectly time synced and gain matched. Time offsets can differ from experiment to experiment, and gains can shift even within a few hours — all of which is caught and taken care of in the calibration [35]. Adding these imperfections would effectively require randomly shifting data and immediately correcting these alterations back to the original values. Standalone test without Monte Carlo aspects could cover this more efficiently. Instead, the trigger time for each PMT is determined and folded with the measured time resolution.

To handle the energy, more effort is required: The measured energy value q for each photomultiplier can be expressed as

$$q_i = g_i \cdot e^{-\lambda d_i} \cdot L \tag{6.1}$$

Where L is the generated light, d_i the deposition position in the scintillator, λ the attenuation coefficient, and g_i the gain of the photomultiplier. Minimal ionizing particles, e.g., muons from cosmic radiation [44], are ideal for energy calibrations, as they deposit a small, but constant amount of energy per unit distance while passing through the material. For the plastic scintillator used here, the energy loss $\epsilon_\mu = \frac{\Delta E}{\Delta x}$ is around $1.8\,\mathrm{MeV\,cm^{-1}}$ to $2.0\,\mathrm{MeV\,cm^{-1}}$ [45].

Using the two photo multipliers at each end of the paddle with length $l = d_1 + d_2$, a position independent energy calibration k for the paddle can be obtained:

$$E_{\mathrm{meas}} = k\sqrt{q_1 q_2} = \sqrt{g_1 g_2} e^{-\lambda l} L \tag{6.2}$$

The calibration for each photomultiplier can then be obtained by using the ratio of the charges and the position information derived from time difference, see [35]. Note how the attenuation is absorbed in the calibration parameter and is no longer relevant — an easy oversight when implementing the digitization of simulated energy depositions.

Currently, the calibration of experimental data does not take the known PMT saturation (see below) into account, which can lead to misconceptions when comparing simulated and experimental data. It would be highly beneficial to implement the saturation correction for experimental data [34].

6.2. PHYSICAL EFFECTS IN THE SCINTILLATOR AND THE PMT

While GEANT4 could handle scintillation, optical absorption, reflection, etc. [4, Ch. 5.10.2-4], Birks' Law and Lambert-Beer's Law are used to save computation time. Light transport simulations with tracking of individual photons have been performed for some parts in the TDR [6, Ch. 4.4].

The scintillation material emits the initial signal at t_0. Photons in the visible light range are created after the organic molecules have been excited. The amount of emitted light L is approximated with a variant of Birks' Law

$$L(E, x, q) = \frac{E}{1 + C_1(q) \cdot \frac{E}{l} + C_2(q) \cdot \left(\frac{E}{l}\right)^2} \tag{6.3}$$

where E is the deposited energy, x is the distance of the energy deposition, and C_x are charge q dependent parameters. The effect of Birks' Law is visualized in Figure 6.1. High energy depositions over a short distance, e.g., heavy ions and proton Bragg peaks, produce a reduced amount of light. The emitted light is calculated for each tracking step and transported to both PMTs. Due to the distance d to the photomultiplier, the arrival time is $t_{\mathrm{PMT}} = t_0 + c_{\mathrm{Medium}} d$ with the effective speed of light in the medium $c_{\mathrm{Medium}} = 14\,\mathrm{cm\,ns^{-1}}$. Also, the light is attenuated exponentially $L_{\mathrm{PMT}} = Le^{-f_{\mathrm{at}} d}$ with the light attenuation length $f_{\mathrm{at}} = 0.008\,\mathrm{cm}^{-1}$. The light pulse is implemented with a sharp rising edge and the material-specific decay constant for the main component of 2.1 ns [46].

The photomultiplier tube (PMT) receives the light pulses and coverts them into a current, which is fed into a channel of the data acquisition (DAQ) electronics, which digitizes the (summed) analog signal and records time and energy. In an ideal case, this conversion would be linear. For the PMTs used in NeuLAND, a saturation effect has been measured:

$$L' = \frac{L_{\mathrm{PMT}}}{1 + f_{\mathrm{sat}} L_{\mathrm{PMT}}} \tag{6.4}$$

where the saturation coefficient has been determined in an experiment to $f_{\mathrm{sat}} \approx 0.012\,\mathrm{MeV}^{-1}$ [25, 46], but it is likely that this factor is gain dependent.

Note that for simplicity, all linear scaling or conversion factors are ignored: Light and current are given in MeV, and the full amount of light is transported to both PMTs (instead of half-half), and no gain factor is introduced for a conversion to current or charge. In addition, the saturation is probably a function of time, i.e., two pulses at different times would probably induce less saturation than a single pulse with twice the amplitude.

6.3. Technical effects of data acquisition and calibration

Data acquisitions are complex systems and their description can fill whole publications on their own. For NeuLAND, two systems are relevant: The *TacQuila* system with several sub-configurations (frontends) has been used for the predecessor LAND, the NeuLAND prototype and the NeuLAND demonstrator. The *Tamex* system will replace the outdated components for the experiments at FAIR.

In this thesis, only the TacQuila system could be considered, as the Tamex electronics is in production and will be available only from the first FAIR experiments onward. This implies that all findings based on hit level data, which includes the full reconstruction part in Chapter 8, is based on the “wrong” data acquisition. While there are significant differences in the inner workings of both systems, there should be no regression of the high-level features of the obtained data, i.e., time and energy resolution.

One major discrepancy could be the procedure integration, i.e., the check if a channel has seen a signal at all (“has fired”), and after how much time after the start of the integration stray incoming pulses are still integrated up into the same output value. While this cannot be disregarded entirely, signals of significant intensity will create significant hits anyway. Hits that only barely exceed the trigger threshold will most likely be filtered out in later stages.

The triggering process has been implemented in a simplified way: The pulse height is calculated as function of time, where incoming pulses are added on the falling tail of the previous pulses. If this pulse height exceeds the hardware threshold, which is typically around 1 MeV, the channel has triggered, and an integration window opens. This trigger time is used as the time information with an uncertainty of $\sigma = 0.15\,\mathrm{ns}$. Within the integration window of 400 ns all incoming light pulses, including the triggering pulse, are summed up.

This sum, typically called *QDC-value* (from charge-to-digital converter) is calibrated to an energy by (1) reversing the attenuation for half the paddle length $Qe^{+\frac{1}{2}l_{\mathrm{Paddle}}f_{\mathrm{at}}}$, (2) reversing the saturation $\frac{Q}{1-f_{\mathrm{sat}}Q}$, and (3) applying the uncertainty of the acquisition setup, here a Gaussian distribution with $\sigma = 5\,\%$.

If both channels of a paddle have fired, a hit is created with the hit energy, time, and position information:

$$E = \sqrt{E_{\mathrm{leftPMT}} \cdot E_{\mathrm{rightPMT}}} \tag{6.5}$$

$$t = \frac{1}{2}(t_{\mathrm{leftPMT}} + t_{\mathrm{rightPMT}}) - \frac{\frac{1}{2}l_{\mathrm{Paddle}}}{c_{\mathrm{Medium}}} \tag{6.6}$$

$$x = \frac{1}{2}(t_{\mathrm{leftPMT}} - t_{\mathrm{rightPMT}})c_{\mathrm{Medium}} \tag{6.7}$$

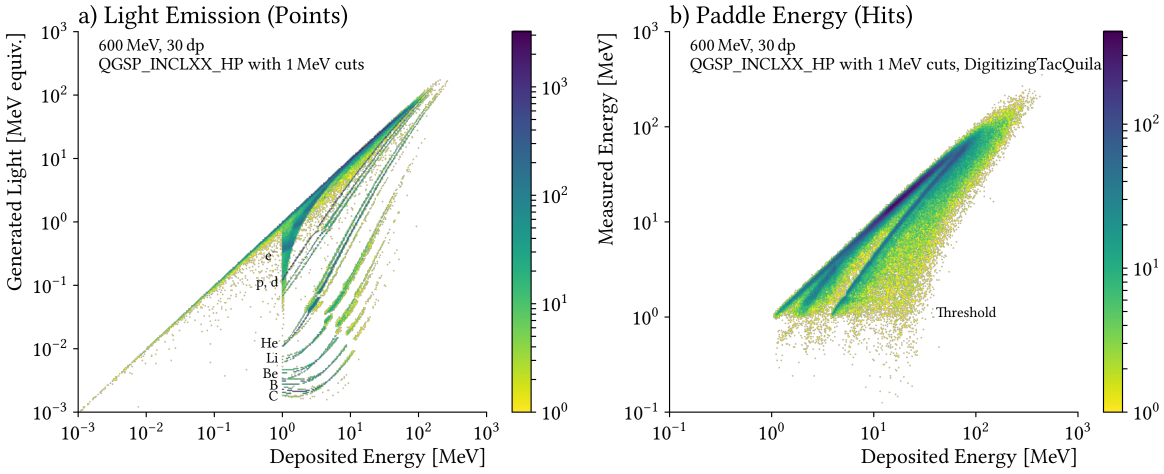

Figure 6.1.: a) Generated light for each individual energy deposition by Monte Carlo tracks (Points). The step length and the deposited energy can depend on settings of the physics list and energy cuts used. Note that charged particles with higher Z produce less light for the same deposited energy. b) Measured energy for the sum of all energy depositions in paddles (Hits) for the adaptation of the implementation of the TacQuila electronics.

To complete the position information, x (or y) and z are inferred from the paddle position. These values are not further modified, the conceivable *box* distribution for the paddle (Uniform distribution) is not applied here[1].

6.4. Comparison to experimental data

Basic properties of hits and the one-neutron detection efficiency were compared to experimental data from the NeuLAND @ SAMURAI campaign described in Section 3.2.

To ensure comparability, the full geometry of the SAMURAI setup was ported to R3BRoot. In the Japanese *smsimulator* program, a Geant4 application for simulating experiments with SAMURAI [38], all required geometries are already implemented. The program was made usable on the local system and modified to write the full geometry into a GMDL file (see Section 12.3). NeuLAND was removed from the GDML file, such that the space could later be filled with the R3BRoot implementation of NeuLAND, and the structure of the internal overarching main volume and hierarchy of volumes was changed to an assembly volume. In addition, an additional class for loading passive geometry from GDML files was created in

---

[1] For a NeuLAND paddle, the standard deviation of the uniform distribution is $\sigma = \frac{5\,\text{cm}}{\sqrt{12}} \approx 1.44\,\text{cm}$, which motivates the NeuLAND design parameter $\sigma_{x,y,z} < 1.5\,\text{cm}$ [6, p. 11].

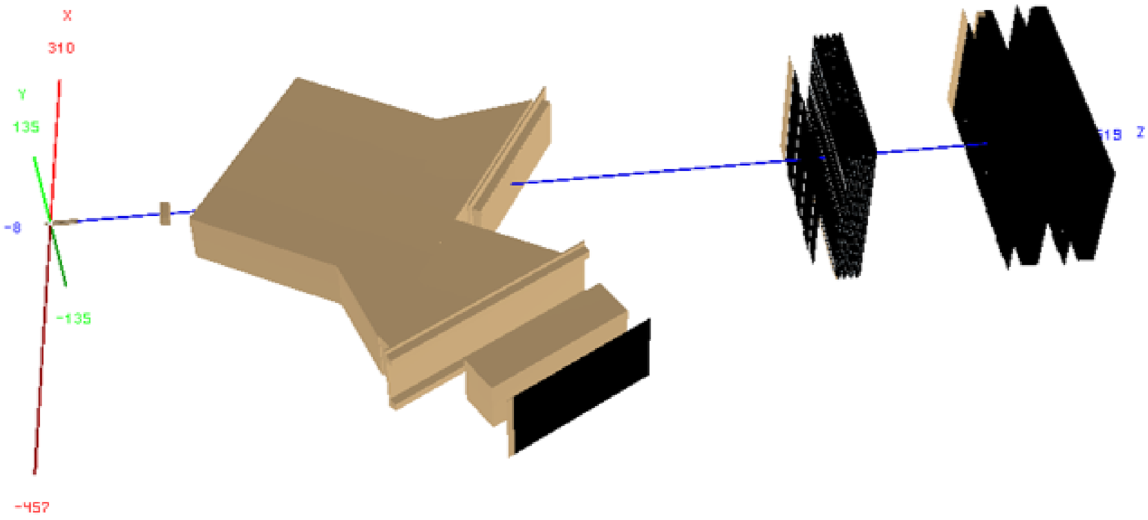

Figure 6.2.: The NEULAND @ SAMURAI setup in R3BRoot. The SAMURAI magnet and all detectors except NeuLAND were imported from a GDML file and used together with the R3BRoot version of NeuLAND. Note that all other detectors are passive, i.e., simulated data was only obtained for NeuLAND.

R3BRoot. Both NeuLAND and the whole SAMURAI setup were then positioned accordingly, the resulting setup is shown in Figure 6.2.

6.4.1. Hit properties

To validate the digitizer, distributions of basic hit properties were compared to experimental data from the ^{29}Ne(p,2p)^{28}F $\longrightarrow$ ^{27}F + n side channel of the ^{27,28}O spectroscopy experiment performed in 2015. This channel was selected because of low background, good statistics, and progress in analysis by Y. Kondo [47].

Primary neutrons were generated with a phase space approach, including the elongation of the liquid hydrogen target [48]. The resulting distributions are shown in Figure 6.3 and match the experiment very well. Note that the intensity is scaled to the experimental values, the efficiency is discussed in the next chapter.

The digitizer can reproduce all basic properties of the hits without any further arbitrary adjustments.

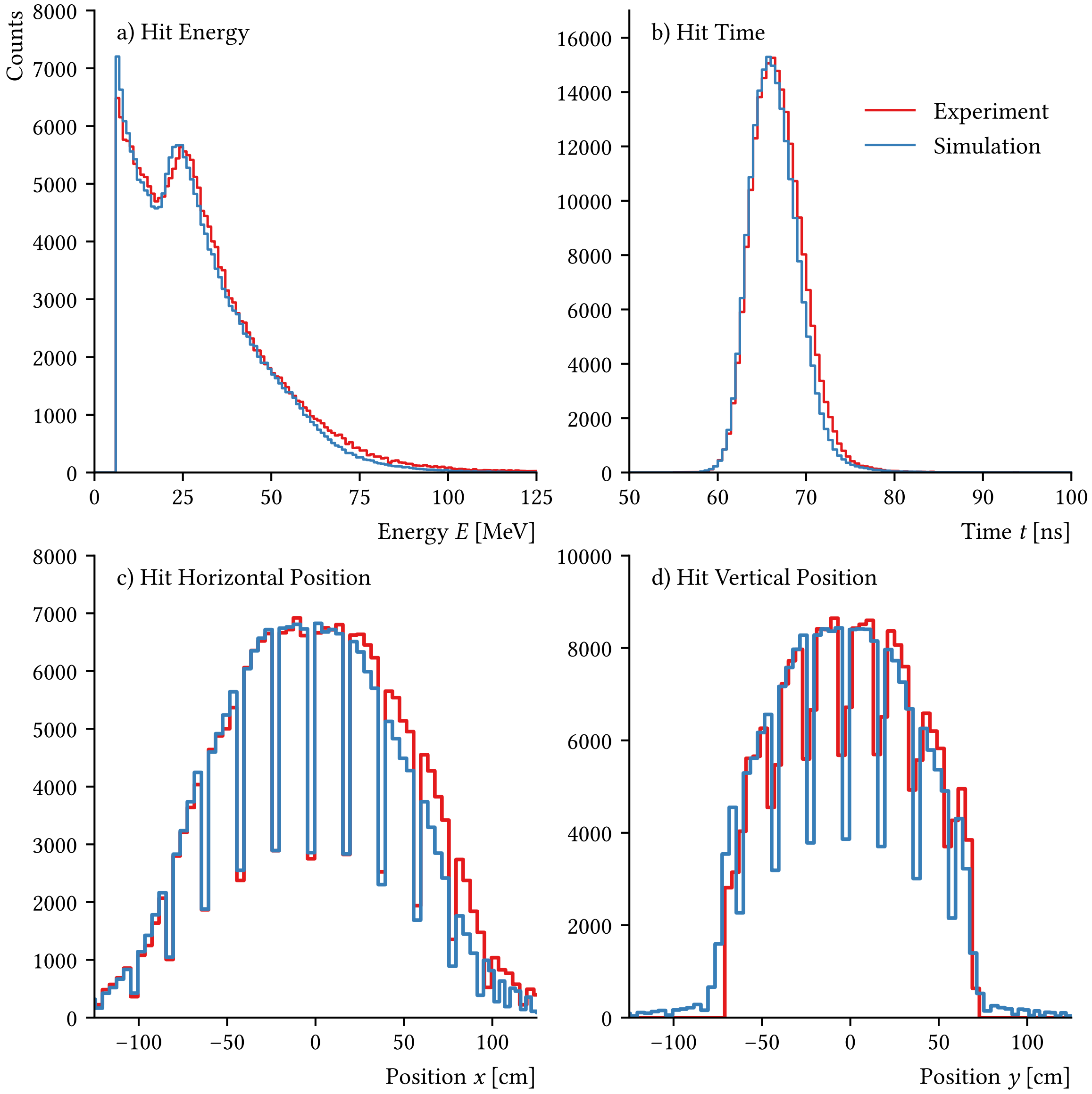

Figure 6.3.: Comparison of experimental and simulated hit energy (a), time (b), and spatial distributions (c, d). The simulated data was scaled to match the experimental. Note that the vertical positions are cut of at the top and bottom due to the SAMURAI magnet. Experimental data by Y. Kondo [47].

6.4.2. Single neutron detection efficiency

During the experimental campaign in Japan, the one neutron efficiency of the NeuLAND double planes was measured in a dedicated experiment, see Table 3.1. Proton beams at 110 MeV and 250 MeV impinged on a ^{7}Li target to produce mono-energetic neutrons with a known cross section [49]. The data was analyzed by J. Kahlbow. Background was a significant problem, as the remaining proton beam was dumped inside the magnet [48, 50, 51].

The neutron detection efficiency depends on the energy threshold applied to the hits in the detector, which can be compared for different implementations of neutron interactions.

In this work, mono-energetic primary neutrons were created with the box generator and the efficiency was determined as a function of the hit energy threshold for all compatible physics list. Photomultiplier saturation was not corrected in the experimental data, which is accounted for in the simulation. Similar cuts as in the experiment were applied, however these were not actually necessary, as they had no or only minor influence on the simulated data.

The simulated values solely depend on the model for the low energy hadronic interactions, i.e., `QGSP_BERT` behaves like `FTFP_BERT`, see also Section 5.3. Physics list variants using high precision neutron interactions for neutrons below 20 MeV (with `_HP` suffix) [52] show no difference to the normal versions. This reduces the comparison to the three models for neutrons between 0.1 GeV to 1 GeV: BERT, BIC, and INCLXX. Figure 6.4 shows a combination of these models with the QGSP model for high energies and high precision low energy neutron. For historical reference, GEANT3 in GCALOR mode is also shown. Note that `QGSP_BIC_HP` and `GCALOR` were used in the TDR, while `QGSP_INCLXX_HP` is the current default in R3BRoot.

Differences between these models are surprisingly large. BERT based physics lists show a significantly lower efficiency and in addition a different behavior at higher thresholds. For both energies, the experimental values are not well matched and fall mostly in the gap between BERT and the other models. At 250 MeV, the shape is recreated well, which could indicate a possible scaling problem in either the models or the experimental data.

Unfortunately, this issue cannot be fully resolved here. `QGSP_BIC_HP` and `QGSP_INCLXX_HP` produce similar results should both be viable options.

The commissioning experiments scheduled for FAIR Phase 0 with more double planes should deliver data at higher energies and with more comparable properties, e.g., distributions as function of detector depth.

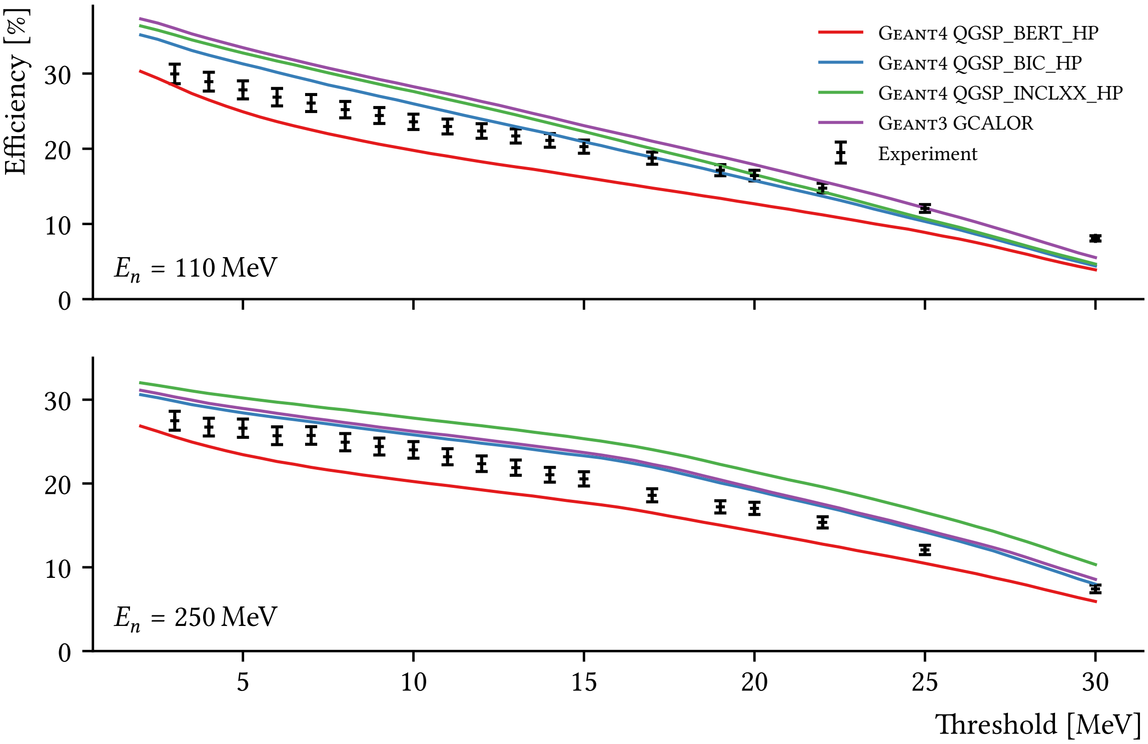

FIGURE 6.4.: Single neutron detection efficiency at 110 MeV and 250 MeV for different hit energy thresholds. The experimental data was gained in an experiment performed with four double planes in RIKEN, evaluated by J. Kahlbow [48, 50]. Photomultiplier saturation was not corrected in the experimental data; this is accounted for in the simulation. The simulations were performed with R3BRoot using GEANT4 with different physics lists and GEANT3 with GCALOR for hadronic interactions.

CHAPTER 7.

CLUSTERS

Clustering is the process of grouping objects together by a specified condition. Here, hits in the individual scintillator paddles are combined to clusters based on their distance.

Several drawbacks were found with the old clustering code. The previous implementation was based on accumulating data, i.e., the total energy and the dimensions were calculated while iterating over all hits, marking hits as clustered in a separate data structure. This process required merging of this accumulated data to join overlapping clusters in a second stage, which lead to several issues: Sometimes, hits were missed that should have belonged to a certain cluster, and often clusters that should have been merged were not. Cluster dimensions were sometimes calculated wrong, and it was basically impossible to add more properties to accumulate.

A new algorithm, dubbed *handshake-chain clustering*, had to be developed in the scope of this thesis[1,2]. It is implemented as a C++ template; thus, any type of object can be clustered together as long as a *handshake*, i.e., a binary classification of togetherness between two objects, can be defined. Thus, it can be used in other projects as well — finding correlated clusters in an unsorted pile of data is an important task in many fields. The individual objects that form a cluster are moved into a separate container, thus all properties of interest can be calculated from this list when needed. This is a vital feature for the analysis of cluster properties and its usage for reconstructing. A cluster is completed if all the included objects have no foreign neighbor close enough to *shake hands with.*

In NeuLAND, a handshake between hits is performed if the distance is sufficiently small, commonly within neighboring scintillator paddles:

$$\Delta x \leq 7.5\,\mathrm{cm} \quad \text{and} \quad \Delta y \leq 7.5\,\mathrm{cm} \quad \text{and} \quad \Delta z \leq 7.5\,\mathrm{cm} \quad \text{and} \quad \Delta t \leq 1\,\mathrm{ns} \tag{7.1}$$

These handshake conditions are a trade-off between ensuring inclusion of correlated hits and avoiding inclusion of uncorrelated hits. The parameters can be changed if needed: For example, Δz can be doubled to mitigate missing hits, which can occur either if no hit is recorded due to an electronics issue, or if multiple energy depositions in different parts of

---

[1] `https://github.com/R3BRootGroup/R3BRoot/pull/96`

[2] `https://github.com/R3BRootGroup/R3BRoot/pull/101`

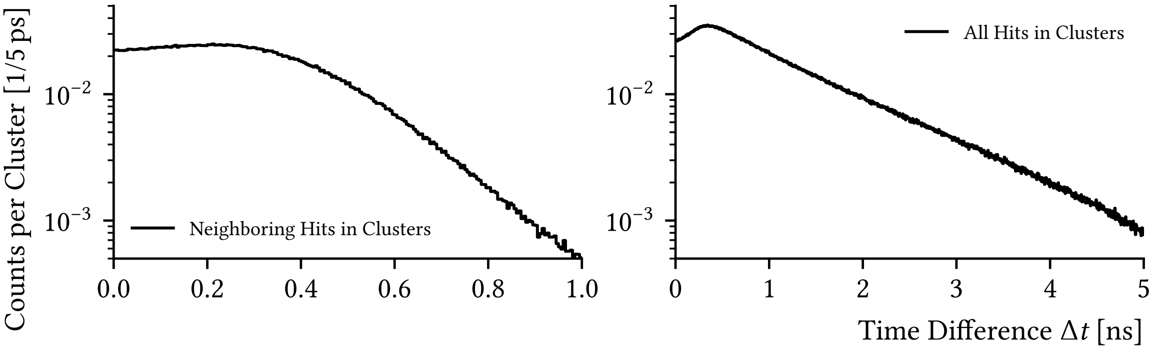

FIGURE 7.1.: Time difference of hits in clusters for one incoming neutron with $E_N = 600\,\text{MeV}$. For clustering of hits in NeuLAND, a time difference of $\Delta t \leq 1\,\text{ns}$ is commonly used. This can be reduced to $\approx$0.75 ns without losing too many hits. Clusters can cover time ranges of up to several ns.

the paddle move the observed position too far out. If many neutrons are impacting too close together, their hits can end up in a single cluster. The time difference Δt can be reduced to mitigate this problem to some degree, see Figure 7.1. Examples for events and clusters are show in Figure 7.2.

7.1. CLUSTER FEATURES

From the total number of clusters in an event, those corresponding to a primary neutron interaction must be chosen. An ideal reconstruction method would pick exactly these primary clusters and disregard the others. This event-by-event selection process can only be based on features of individual clusters, like size and energy, and on properties at large, i.e., the number of clusters and the total energy deposited. Even if information on the multiplicity is reliably provided by other detectors, this selection is still required.

The simulation provides the first interaction points, which can be used to unambiguously determine the primary clusters. A comparison to all clusters can then show which features are able to distinguish primary and secondary clusters.

At the same time, this perfect *cheating* reconstruction method yields the maximum achievable performance, that is, the best outcome any algorithm can achieve. This performance deviates from the theoretical maximum (Section 5.4) by a few percent, see Table 8.2, due to too low energy deposition or reactions in inactive material without break through into the active material.

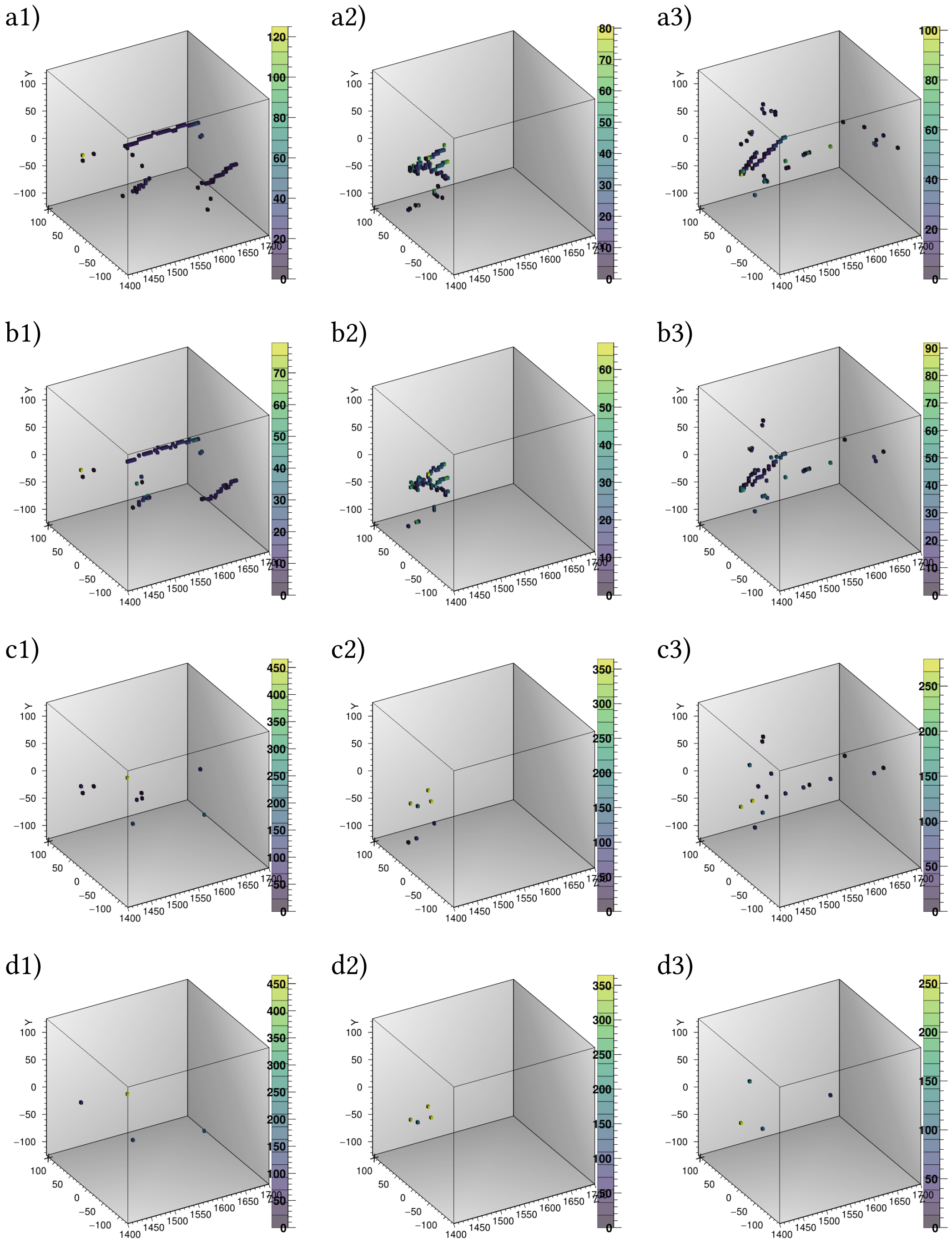

FIGURE 7.2.: Energy depositions (a), hits (b), clusters (c), and neutron interaction points (d) for three events (1-3) in NeuLAND. Four incoming Neutrons with $E_N = 600$ MeV react in 30 double planes and create diverse hit patterns. The interaction points in event 1) are well separated and can be easily located. In event 2), hits are close together but still separated. It is not obvious from the hit distribution where the interactions took place in event 3).

In the following, features of individual clusters and properties of all clusters in an event (*ensemble*) are presented.

7.2. Ensemble properties

Two main properties can be calculated for each event: The number of clusters and the total deposited energy; both scale with the number of neutrons. The distributions broaden for higher neutron multiplicities, as they are convolutions of the one neutron distribution, see Figure 7.3. Note that even for 30 double planes, the distributions are too broad to cleanly separate the multiplicities by one quantity alone. Neutron multiplicity determination in the TDR uses both number of clusters and the total deposited energy which are plotted in one two-dimensional histogram, see Section 8.1.

7.3. Individual properties

Some properties of clusters might be good indicators for a classification between primary and secondary clusters.

Individual properties of primary clusters are compared to secondary clusters directly, and also shown as the fraction of all clusters (PC/(PC + SC). In an ideal case, the fraction would be 100 % for some value range of the feature, and then immediately drop to zero. A gate applied on this interval would perfectly separate primary and secondary clusters.

It was found that for the physics cases simulated here, a gate on the energy from time-of-flight (E_{ToF}, see below) and the cluster energy E is highly effective. All features are also tested with a pre-filtered set of clusters that fulfill the conditions

$$E > 10\,\mathrm{MeV} \quad \text{and} \quad 0.95 \cdot E_{\mathrm{Beam}} < E_{ToF} < 1.05 \cdot E_{\mathrm{Beam}}. \tag{7.2}$$

The dependency on the beam energy might not be appropriate for neutrons from a delayed decay from, e.g., fission experiments. For the Lorentz-Boosted Phase-Space decays discussed in Section 3.3 and Section 5.1, this cut is applicable.

In Figure 7.4 and Figure 7.5 the Counts per incoming primary neutron (CPN) are shown as a function of individual cluster features. The details are discussed in the following:

Size The cluster size N denotes the number of hits clustered together. While there is an over-proportional number of one-hit clusters, the occurrence of larger clusters drops exponentially from two neutrons onward. The fraction of the cluster size rises logarithmically from effectively zero for $N = 1$ to about 70 % for size 15 and above. However, if

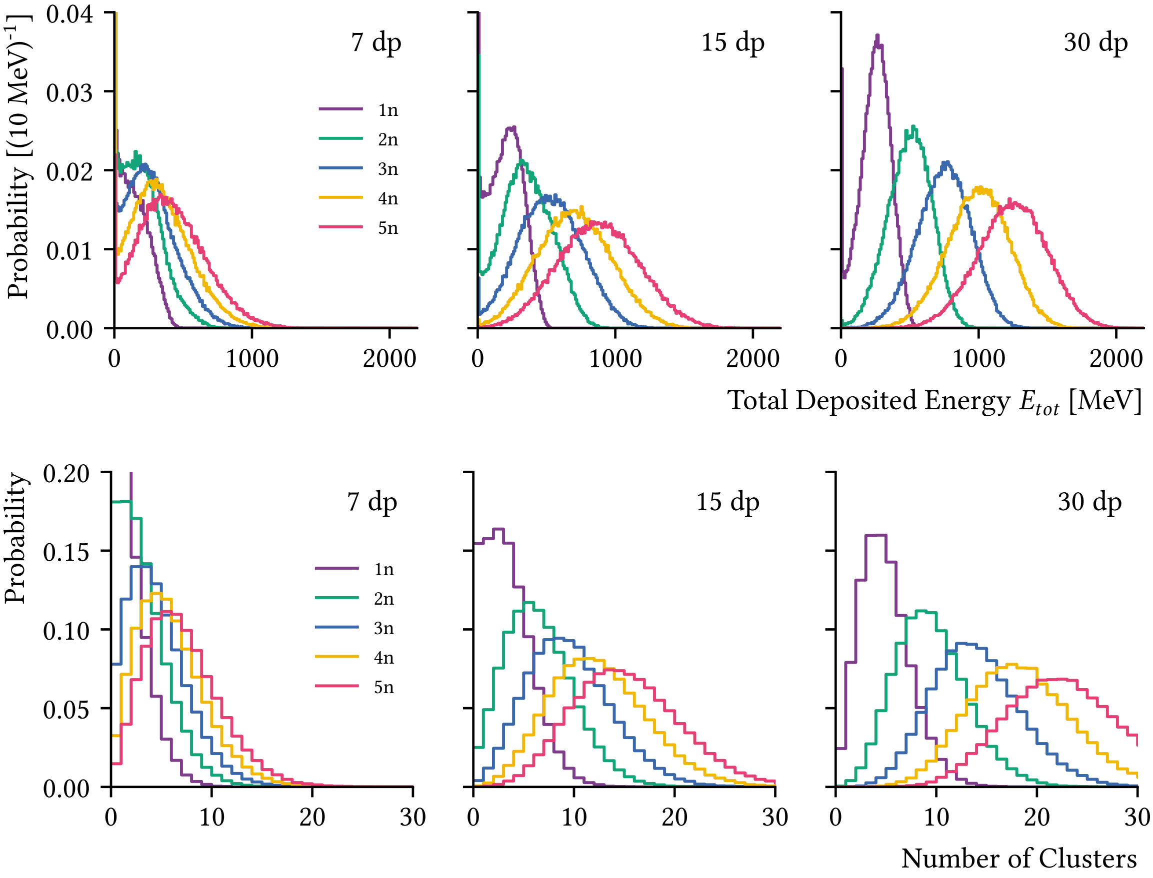

FIGURE 7.3.: Total measured energy and number of clusters for different number of neutrons and double planes for a neutron energy of $E_N = 600$ MeV. Note that while the average deposited energy and the number of clusters is correlated to the number of incoming neutrons, the resolution is not high enough to separate the individual channels event-by-event.

the pre-filter is applied, many clusters with small sizes are removed and the fraction is more-or-less constant at 70 %.

Energy The cluster energy E is the sum over the energy of the individual hits. Like the cluster size, there is an overabundance of hits with energies below 10 MeV. Energies up to 300 MeV are quite common, with a steep drop off when approaching the energy of the primary neutron. The fraction for the cluster energy, similar as for the cluster size, rises linearly until reaching 80 % at 300 MeV. If the clusters are pre-filtered, the fraction already starts at 50 %.

Time-of-Flight The time-of-flight t is the time from the start signal (emission of the neutron) to the detected time of the first hit in the cluster. The expected perfect exponential

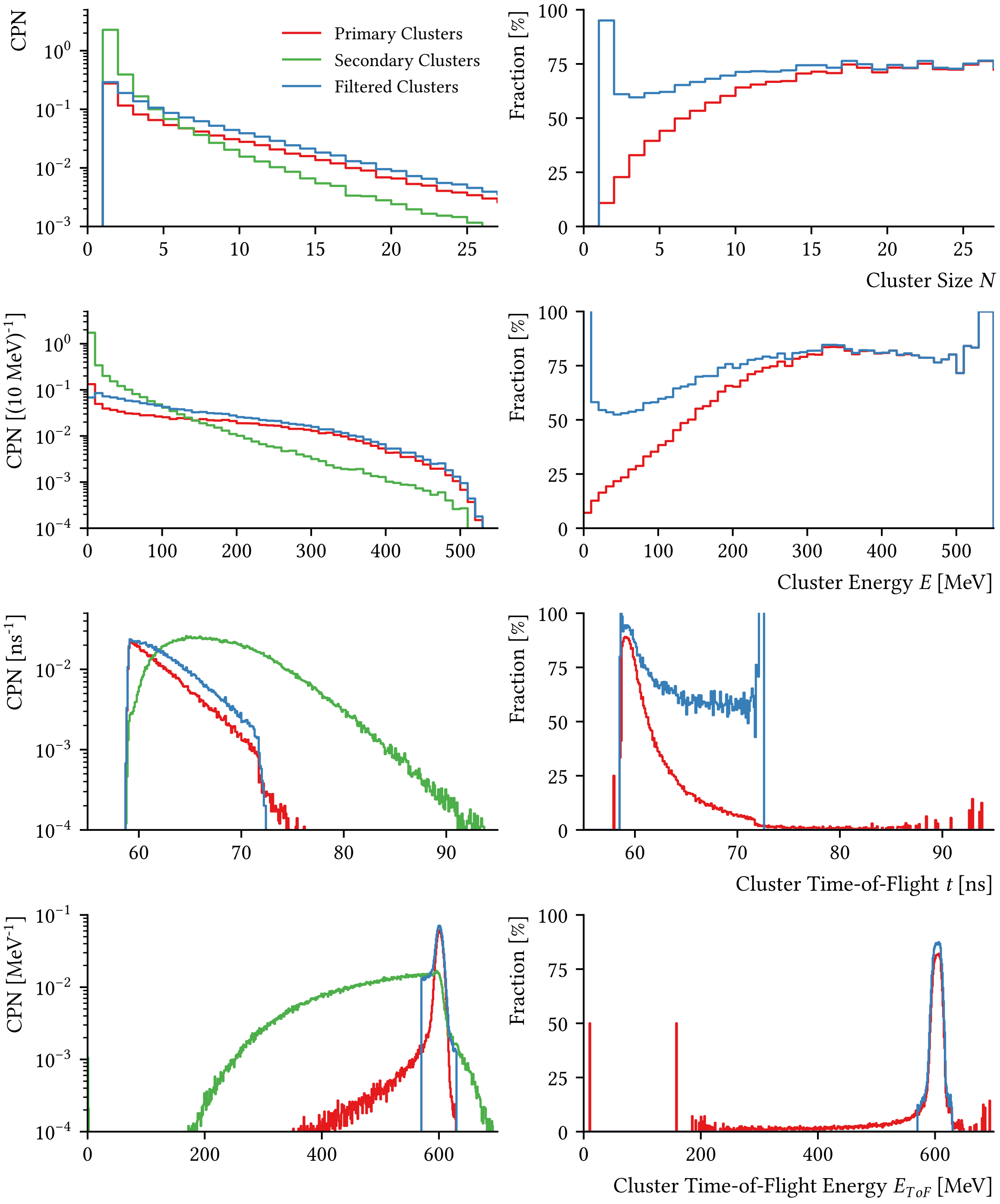

Figure 7.4.: Counts per neutron (CPN) and fraction of all clusters for cluster size, energy, time-of-flight, and neutron energy from time-of-flight. See text for details.

decline can be seen for the primary clusters for a time interval corresponding to the depth of the detector, during which the neutron intensity drops according to Lambert-Beer's law. On top of this, an enormous number of hits is detected both during this interval and after, with a peak located around the middle of the primary hit interval. The first hits must stem from a primary neutron, the fraction of the earliest hits is thus of course 100 %. In the same notion, clusters with times outside of the interval can be immediately disregarded. Within this window, the situation is less clear, as secondary particles deposit energy at the same time with neutrons in the back of the detector. This results in fractions as low as 10 % just before the end of the interval. Even with the pre-filter applied, only 60 % can be reached here.

Neutron Energy from Time-of-Flight Assuming the cluster is created by a neutron stemming from the target, the time-of-flight and the position of the first hit in the cluster can be used to calculate the neutron energy E_{ToF}, see Equation (1.2). In the physics cases simulated here, neutrons are emitted within a narrow energy window (FWZM < 10 %), thus primary clusters must have a corresponding E_{ToF}. Secondary clusters that fall within the time-of-flight acceptance interval are rarely located at positions that match the required E_{ToF}. The fraction function is close to ideal: A sharp Gaussian peak reaching 90 %, which can be easily gated on. Hence, a hard cut on E_{ToF} is the single best method of eliminating unwanted clusters and was therefore used in the pre-filter condition.

R-Value The R-Value, defined as $R = \frac{|\beta_{Beam} - \beta_{Cluster}|}{E}$, is a critical component of the reconstruction method proposed in the TDR, see Section 8.1. For the calculation of R, external knowledge of the beam velocity β_{Beam} is required; it cannot be calculated and then, in a second step, be cut upon. In terms of fraction, the logarithm of R-Value does surprisingly well. A plateau at 85 % is followed by a rapid drop of to 20 % and a slow descent to zero.

Timespan The cluster timespan, that is the time difference between the last and the first hit in the cluster, behaves like the cluster size. This is expected, as larger clusters are mostly created by protons passing through the planes.

Distance The distance from the center $\sqrt{x^2 + y^2}$ is a measure for the angular spread of the incoming neutrons, which is directly related to E_{rel}. For a specific angular spread, clusters outside of the cone size are less likely to stem from a primary neutron interaction.

Depth The depth z shows the expected logarithmic decline also seen for the cluster time t, however here no sharp edge in the fraction can be exploited for cuts.

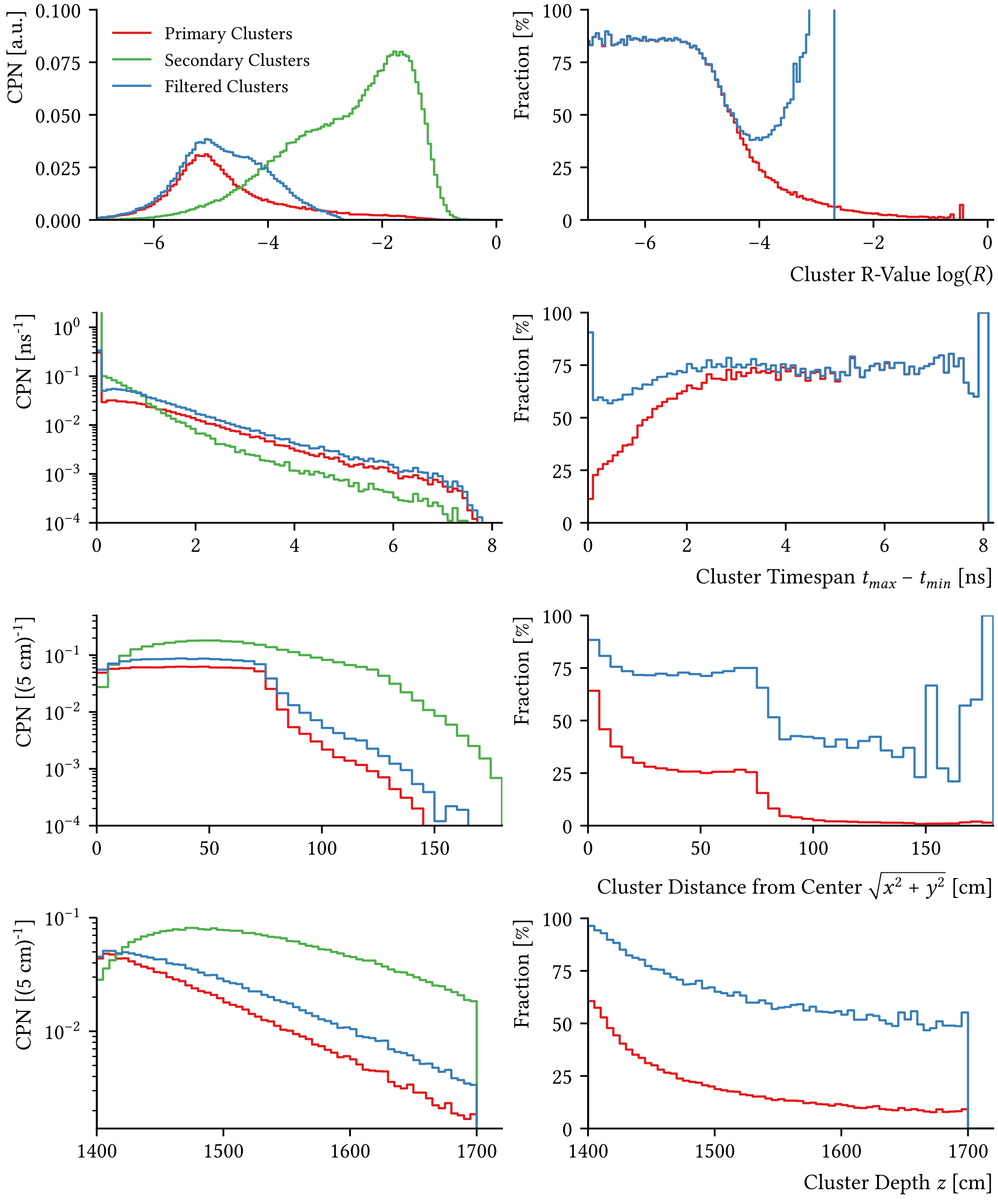

Figure 7.5.: Counts per neutron (CPN) and fraction of all clusters for cluster R-value, timespan, distance from center, and depth. See text for details.

7.4. PROTON TRACKING

High energetic protons produced by primary neutrons (see Section 5.4) deposit their energy over a long distance, spanning several paddles. Examples of proton tracks can be seen in Figure 7.2 (b1-3). These so-called Bragg tracks with the characteristic Bragg peak at the end carry information about the energy of the proton via length and deposited energy, as well as about the direction.

Track finding is a common task in high energy physics. Other large segmented detectors like PANDA use sophisticated algorithms like Triplet Finder and Circle Hough [53, 54], which require computer graphics cards (GPUs) to handle the intense computational load. These algorithms could be used for NeuLAND; however, all information is already encapsulated in clusters.

Here, a method is presented to use proton Bragg tracks to determine the energy of the primary neutron without a track finder or a fitting algorithm. While only few percent of all clusters consist of clean tracks, the following steps can be performed for each cluster with negligible computational power.

First, the cluster energy centroid vector $\mathbf{x}_{EC}$ is defined as

$$\mathbf{x}_{EC} = \frac{\sum_{h \in H} \mathbf{x}_h E_h}{\sum_{h \in H} E_h}, \tag{7.3}$$

which is equivalent to the geometric center, except that the sum over the hits H should not include the first two hits to avoid energy depositions from other particles. Using as much information as possible provides additional robustness to stray or missing hits, contrary to only using the vector between the first and last hit. This centroid vector can be used to calculate the angle $\theta_{NP'}$ between the direction of the incoming primary neutron N and the scattered proton P':

$$\cos\theta_{NP'} = \frac{(\mathbf{x}_{EC} - \mathbf{x}_{\text{First}}) \cdot \mathbf{x}_{\text{First}}}{|(\mathbf{x}_{EC} - \mathbf{x}_{\text{First}})| \, |\mathbf{x}_{\text{First}}|} \tag{7.4}$$

In addition, the cluster moment M can be defined as

$$M = \frac{\sum_{h \in H} |\mathbf{x}_h - \mathbf{x}_{EC}| \, E_h}{\sum_{h \in H} E_h} \tag{7.5}$$

which is a measure for the initial energy of the proton, and using calibration simulations with protons of different energies the relation

$$E_{P'}(M) = 55.629 \cdot M^{0.6521} \tag{7.6}$$

could be determined. This energy $E_{P'}(M)$ can be compared to the actual deposited energy in the cluster E.

The most important quantity is the energy of the primary neutron E_N. Using four-momentum calculations, a formula for this energy as a function of the scattered proton energy and the scattering angle could be derived, see Appendix A.2 for the step-by-step derivation.

$$E_N(E'_P, \theta_{NP'}) = \frac{2m_0c^2 E'_P}{2m_0c^2 \cos^2\theta_{NP'} - E'_P \sin^2\theta_{NP'}} \tag{7.7}$$

CHAPTER 8.

RECONSTRUCTION

Neutron multiplicity and primary neutron interaction points are reconstructed for each event. These two quantities are correlated, but independent to some degree — the multiplicity can be determined without reconstructing or even without being *able* to reconstruct the correct interaction points. Thus, there must always be a function to rank clusters, and a way to limit the neutron multiplicity, i.e., the number of clusters to select.

NeuLAND should be able to determine the neutron multiplicity on its own. While other detectors can supply information about the number of incoming neutrons in some experiments, full information on all involved particles is highly desirable: It allows for kinematically complete measurements with the benefit of removing background effectively.

It is important to remember that not all incoming neutrons will react in the detector, especially not for a system with fewer double planes, as discussed in Section 5.4. From the measured data in NeuLAND, one can only reconstruct the number of reactions N_{reac} for each event — a challenge of its own, which is discussed in detail in this chapter. If enough events have been recorded, conclusions on the number of incoming neutrons N_{in} can be drawn from the individual distributions.

Algorithms should select the clusters that correspond to the interaction of a primary neutron from the large number of clusters detected in each event. For simulated data, the correct answer is known, and the performance of each model can be investigated in different situations. As discussed in Chapter 6, this should mirror equivalent experimental data sufficiently well.

Three different models try to solve both challenges: In the TDR, an algorithm was proposed with a strict separation of multiplicity determination and cluster ranking. While it was found to be sufficient for the full detector, doubts were raised if it can handle the task if only few double planes are available. In the scope of this thesis, this method was refined, and two additional methods were designed to alleviate this problem. Both new algorithms are based on using as much information of all clusters as possible, based on the features discussed in Chapter 7.

8.1. The reconstruction method proposed in the TDR

The TDR acknowledges the cluster selection challenge and provides a simple algorithm designed for the full-depth detector [6, p. 55]. The multi neutron reconstruction process is split into determining the neutron multiplicity using calorimetry and sorting instructions based on the cluster velocity and deposited energy; both parts are fully independent.

Neutron reactions in the detector produce a statistically distributed number of clusters and deposited energy. For multiple incoming neutrons, the deposited energy is the convolution of multiple one-neutron distributions. The detector can be considered as a calorimeter if the deposited energy distribution for a single neutron is sufficiently narrow. In this case, the deposited energy indicates the number of incoming primary neutrons that have reacted in the detector.

It has been indicated that the information on the deposited energy alone does not allow for a clean separation of the different neutron multiplicity channels [6, 34] — the overlap between the energy distributions for different numbers of incoming neutrons is too large, as can be seen in Figure 7.3. In combination with the number of clusters, which is a related but not fully proportional statistical distribution, an acceptable separation can be achieved for the full detector [6].

In this so-called *2DCalibr* method, the number of clusters is plotted together with the total energy in a two-dimensional histogram for each multiplicity number. Different regions in this plot represent different multiplicities. In the TDR and the previous implementations, these regions were created by diagonal cuts in the 2D histogram. Using only one-neutrons events, different values of a gradient are tested by increasing the intercept until the area outside the cut, which represents the incorrectly assigned efficiency, is below a given value. For all higher multiplicities, the same gradient is used, and the intercepts determined as above. The gradient and the intercepts are then stored in a text file for use in the next step. Note that in this process, the histograms were created based on the number of incoming neutrons.

This calibration data then determines the number of neutrons to reconstruct for each event. From all clusters, the timewise first cluster is always taken. Then, clusters with the lowest R-value (see Section 7.3) are taken until the neutron multiplicity is reached.

8.1.1. The TDR+ reconstruction method

In the scope of this thesis, the 2DCalibr method has been overhauled, and now forms the *TDR+* reconstruction algorithm. Two-dimensional histograms are now created based on the number of reacted neutrons to accommodate the reduced interaction probability. For these, cuts are now calculated by minimizing the overall mis-assigned events using the `Minuit2` minimizer and stored as `TCutGs` in a ROOT file using `R3BNeulandNeutron2DPar`, which

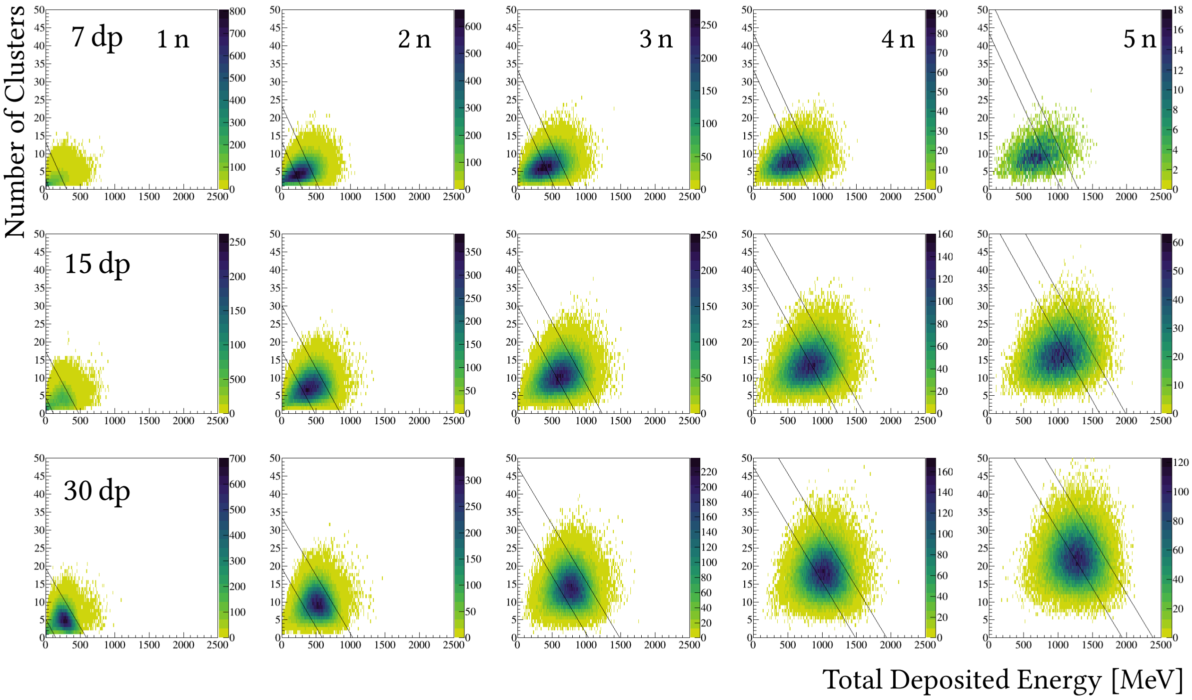

Figure 8.1.: Two-dimensional histograms of the number of clusters and the total deposited energy for 1 to 5 reacted neutrons at 600 MeV for 7, 15, and 30 double planes. Cuts are placed such that the integrals outside of the cuts are minimized. Note that for larger numbers of double planes the peaks get significantly sharper and separated from other peaks. For 30 double planes, the cuts can be placed almost centered around the peak location.

ties into the FairRoot parameter storage concept. This also enables greater control for the user, because arbitrary cuts, changes, and shifts can be accommodated. The cluster selection process was not changed, but fully re-implemented to match coding standards and to fit into the dependency injection design.

Distributions and cuts for 7, 15, and 30 double planes are visualized in Figure 8.1.

8.2. Event reconstruction using cluster scoring

Some of the features of clusters discussed in Section 7.1 show a significant difference between primary and secondary clusters — differences that can be exploited.

To classify each cluster, a scoring system was developed. First, a score of zero is assigned to each cluster, forming a `ScoredCluster`. A container with all scored clusters is created, and passed to individual functions, called *scorers*, that judge features and modify the score. The scorers are independent functions and can be added to the reconstruction task depending on the experiment. Internally, the scorers are implemented as `std::functions`, which can be stored in a container and iterated over. This also enables the user to add new scorers on-the-fly if needed, an example is given in Listing 1.

```
auto reco = new Neuland::ClusterScoring();

// Custom EToF Cut in shape of a scorer for E_N ~ 600 MeV
auto scoreEToF = [](std::vector<ScoredCluster>& scs) {
    for (auto& sc : scs)
    {
        if (sc.cluster->GetEToF() > 620 || sc.cluster->GetEToF() < 580)
        {
            sc.score -= 100.;
        }
    }
};
reco->AddScorer(scoreEToF);

// Prepared Scores
reco->AddScorer(Neuland::ClusterScoring::scoreEnergy);
reco->AddScorer(Neuland::ClusterScoring::scoreClusterSize);
reco->AddScorer(Neuland::ClusterScoring::scoreHitSequenceWithDescendingZPosition);
reco->AddScorer(Neuland::ClusterScoring::scoreElasticSecondaryInterations);
reco->AddScorer(Neuland::ClusterScoring::scoreProtonTracksMatchingToF);

// Inject the prepared dependency into the task and add it to the run
run.AddTask(new R3BNeulandNeutronReconstruction(reco));
```

LISTING 1.: Example usage of the cluster scoring reconstruction in a macro.

Both individual features as well as interdependencies between clusters can be scored. For example, a high energy increases the score, while a low energy decreases it. Scorers are available for simple features like cluster size and energy, for more complex features like the neutron energy derived from proton tracks (see Section 7.4), and for sequences which take, e.g., the time series into account.

In total, seven predefined scorers are available:

`scoreEnergy` and `scoreClusterSize` reward clusters with high energy and many hits. Score is awarded in four categories: Negative for low size and energy, none for intermediate, positive for high, and very positive for exceptionally large and very energetic clusters.

`scoreFirstCluster` and `scoreHitSequenceWithDescecdingZPosition` use causality of arrival: The first cluster must stem from a neutron (excluding early γ-rays). If it has reacted in the back of the detector, a subsequent hit in the front is likely to be another neutron.

`scoreProtonTracksMatchingToF` and `scoreElasticSecondaryInterations` try to use momentum arguments. The first tracks the proton and compares the neutron energy from time-of-flight, as discussed in Section 7.4, while the later tries to eliminate secondary hits.

`handleMultiHitClusters` is a highly experimental scorer to mitigate the problem at low E_{rel}: If too many neutrons hit the detector too close together, e.g., the two innermost bars, their hits end up in the same cluster. If the first neutron is reacting further back in the detector, the cluster will have an unusual time structure. In this case, the cluster can be split into two.

The scorers are built for 600 MeV neutrons, but some are energy independent, e.g., the hit sequence, or usable over a wide energy range, e.g., the comparison of proton tracks to time-of-flight. They should always be combined with the additional user-build filtering function like in Listing 1. Note that this filter makes `scoreElasticSecondaryInterations` basically superfluous.

A minimal score is set, usually only slightly over 0 such that not too many false negatives occur, and all clusters fulfilling this requirement are taken as neutron interaction points. The neutron multiplicity is then simply the number of these points — a contrary approach to the TDR.

8.3. EVENT RECONSTRUCTION USING BAYESIAN STATISTICS

In the previous method, the cluster features presented in Section 7.1 were processed into scorers manually. Scoring intervals and weight are selected by hand, which might introduce inconsistent parameters.

Bayesian statistics provides a way of calculating probabilities for hypotheses H under the effect of data $\mathbf{E} = E_1, ..., E_k$

$$P(H|\mathbf{E}) = P(H)\frac{P(\mathbf{E}|H)}{\sum_h P(\mathbf{E}|H_h)P(H_h)} \quad \text{with} \quad P(\mathbf{E}|H) = \prod_{E\in\mathbf{E}} P(E|H), \tag{8.1}$$

where $P(H)$ is the probability before the consideration of data, called *prior*; $P(H|\mathbf{E})$ the probability of H after $\mathbf{E}$, called *posterior*; and $P(E|H)$ the probability of observing E given H, also known as the *likelihood*. In a nutshell: Likelihoods can be multiplied with each other which, after normalization, results in a probability for each possible outcome.

This can be applied to determine both the neutron multiplicity and select the primary clusters. For the neutron multiplicity, the hypotheses range from one neutron to five neutrons $\mathbf{H} = \{1n, 2n, 3n, 4n, 5n\}$. Currently, $H = 0n$ is only assigned to events without any clusters. This set of hypotheses, assuming the multiplicity cannot be higher than five, fulfills the requirements

Table 8.1.: Multiplicity determination using Bayesian statistics for an event with $E_{tot} = 1000\,\text{MeV}$ and 15 clusters for a neutron energy of 600 MeV in 30 double planes. No prior information is assumed, thus all hypotheses start with an initial probability $P(H) = 1/5$. The likelihoods $P(E_{tot}|H)$ for an energy deposition of $E_{tot} = 1000\,\text{MeV}$ and $P(N_{clus}|H)$ for 15 detected clusters are looked up from simulated distributions for each number of reacted neutrons H, see Figure 7.3. These values are then multiplied and normalized to from the resulting probabilities $P(H|\mathbf{E})$. This particular event would be classified with multiplicity four with a probability of 67 %.

H	$P(H)$	$P(E_{tot} = 1000\,\text{MeV}\vert H)$	$P(N_{clus} = 15\vert H)$	$P(H\vert\mathbf{E})$
1n	1/5	0	0	
2n	1/5	0	0.026	
3n	1/5	0.009	0.080	0.13
4n	1/5	0.017	0.072	0.67
5n	1/5	0.010	0.036	0.20

of mutual exclusiveness and collective exhaustiveness. The number of clusters and the total deposited energy can be used as data, the probabilities shown in Figure 7.3 are the likelihoods entering the calculations. In principle, the individual probabilities must be independent. This requirement is not completely fulfilled here but ignored. An example is given in Table 8.1.

Another application is the determination of primary clusters. Here, the choice is only between primary cluster (PC) and secondary cluster ($\overline{\text{PC}}$), however more evidence can be applied: The counts C for one neutron for the features energy E, size N, energy from time-of-flight E_{ToF}, time t, and R-Value R were used as likelihoods for each cluster

$$P(\text{PC}|\mathbf{E}) = \frac{1}{2} \cdot C(E|\text{PC}) \cdot C(N|\text{PC}) \cdot C(E_{ToF}|\text{PC}) \cdot C(t|\text{PC}) \cdot C(\log(R)|\text{PC}) \tag{8.2}$$

$$P(\overline{\text{PC}}|\mathbf{E}) = \frac{1}{2} \cdot C(E|\overline{\text{PC}}) \cdot C(N|\overline{\text{PC}}) \cdot C(E_{ToF}|\overline{\text{PC}}) \cdot C(t|\overline{\text{PC}}) \cdot C(\log(R)|\overline{\text{PC}}) \tag{8.3}$$

and normalized with $P(\text{PC}|\mathbf{E}) + P(\overline{\text{PC}}|\mathbf{E})$. In Figure 7.4 and Figure 7.5, the counts per neutron (CPN) are shown for primary clusters (PC) and all clusters ($\text{PC} + \overline{\text{PC}}$). The resulting probability distributions are shown in Figure 8.2.

In a variation of this algorithm, called BayesWCP, the cluster probabilities can be included in the multiplicity determination: Clusters are sorted by $P(\text{PC})$ descending, and the n-th probability is multiplied with the hypothesis for n reacted neutrons.

$$P(H \in \{1n, 2n, 3n, 4n, 5n\}|\mathbf{E}) = \frac{1}{5} \cdot P(E_{tot}|H) \cdot P(N_{clus}|H) \cdot P_H(\text{PC}|\mathbf{E}) \tag{8.4}$$

The multiplicity with the highest probability is then chosen alongside with the respective number of clusters. Note that the probability of the n-th best cluster can be volatile and

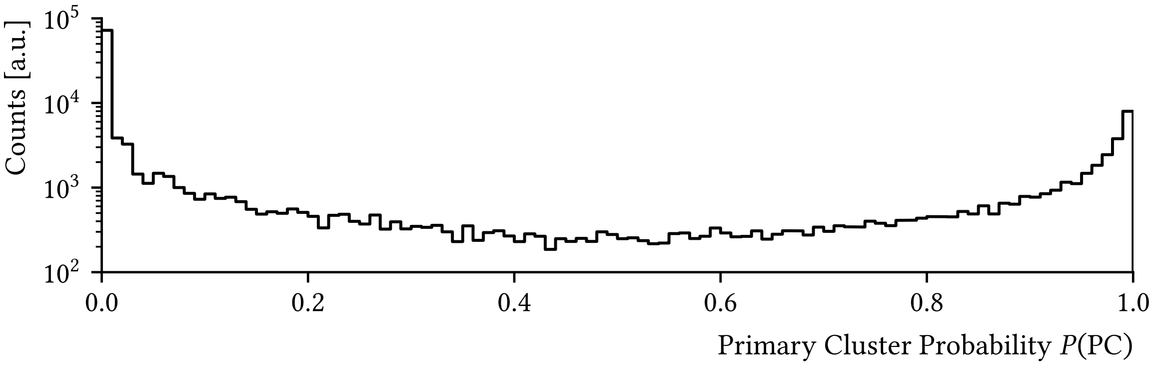

FIGURE 8.2.: Primary cluster probability distribution for one neutron with 600 MeV on 7 double planes. Many clusters can be identified reliably as primary ($P(\mathrm{PC}) = 1$) or secondary cluster ($P(\mathrm{PC}) = 0$).

lead to more off-by-one multiplicity assignments. This can be mitigated with averages while retaining enough impact:

$$P(H \in \{1n, 2n, 3n, 4n, 5n\}|\mathbf{E}) = \frac{1}{5} \cdot P(E_{tot}|H) \cdot P(N_{clus}|H) \cdot \frac{1}{H} \sum_{h=1}^{H} P_h(\mathrm{PC}|\mathbf{E}) \tag{8.5}$$

If other detectors can provide the information on the number of incoming neutrons, the prior can be changed to the known Equation (5.1), which should allow for more reliable values of N_{reac}.

Note that in principle, the probability for each combination of PC and $\overline{\mathrm{PC}}$ over all clusters could be determined. Then, also relationships between clusters could be included, which is not possible here.

8.4. ANALYSIS

8.4.1. MULTIPLICITY

In the TDR, tables were used that show the multiplicity as a percentage for each number of incoming neutrons. The optimal results are given in Table 8.2, and the results for the TDR 2DCalibr, the Scoring, and the Bayesian method are given in Table 8.3, Table 8.4, and Table 8.5, respectively. Note that the tables disregard the difference between incoming neutrons N_{in} and reacted neutrons N_{reac}, which is significant for lower detector depth. In addition, the values do not show if the multiplicity assignment was correct on an event-by-event basis. Lastly, they give no indication if the clusters reconstructed are useful for further physical analysis.

TABLE 8.2.: Neutron separation matrices for an optimal multiplicity determination. Values in [%], see text for details.

7 dp		Incoming Neutrons				
600 MeV		1n	2n	3n	4n	5n
Detected Multiplicity	0n	47	22	10	5	2
	1n	53	47	31	18	10
	2n		31	41	36	26
	3n			18	31	34
	4n				10	22
	5n					6

15 dp		Incoming Neutrons				
600 MeV		1n	2n	3n	4n	5n
Detected Multiplicity	0n	21	4	1		
	1n	79	29	8	2	
	2n		66	35	12	3
	3n			56	38	17
	4n				47	40
	5n					39

30 dp		Incoming Neutrons				
600 MeV		1n	2n	3n	4n	5n
Detected Multiplicity	0n	7				
	1n	93	10	1		
	2n		90	12	1	
	3n			88	13	1
	4n				86	15
	5n					83

TABLE 8.3.: Neutron separation matrices obtained with the TDR+ (2DCalibr) method.

7 dp		Incoming Neutrons				
600 MeV		1n	2n	3n	4n	5n
Detected Multiplicity	0 n	51	26	13	6	3
	1 n	39	45	37	28	19
	2 n	9	24	33	35	32
	3 n		5	14	22	27
	4 n			3	8	13
	5 n				2	4

15 dp		Incoming Neutrons				
600 MeV		1n	2n	3n	4n	5n
Detected Multiplicity	0 n	27	6	1		
	1 n	66	39	17	6	2
	2 n	8	46	42	25	12
	3 n		9	33	39	30
	4 n			7	24	35
	5 n				5	17

30 dp		Incoming Neutrons				
600 MeV		1n	2n	3n	4n	5n
Detected Multiplicity	0 n	7				
	1 n	88	18	2		
	2 n	5	74	28	5	1
	3 n		7	62	37	9
	4 n			8	51	42
	5 n				7	42

TABLE 8.4.: Neutron separation matrices obtained with the Scoring method.

7 dp		Incoming Neutrons				
600 MeV		1n	2n	3n	4n	5n
Detected Multiplicity	0 n	68	34	17	9	5
	1 n	27	42	37	28	21
	2 n	4	18	28	31	29
	3 n	1	5	12	19	23
	4 n		1	4	8	13
	5 n			2	4	9

15 dp		Incoming Neutrons				
600 MeV		1n	2n	3n	4n	5n
Detected Multiplicity	0 n	49	13	4	1	
	1 n	39	36	18	8	4
	2 n	10	31	30	19	12
	3 n	2	13	26	26	20
	4 n		4	14	22	23
	5 n		2	9	24	41

30 dp		Incoming Neutrons				
600 MeV		1n	2n	3n	4n	5n
Detected Multiplicity	0 n	39	6	1		
	1 n	45	28	8	2	1
	2 n	13	37	23	9	4
	3 n	3	20	30	20	10
	4 n	1	7	21	25	18
	5 n		3	17	43	67

TABLE 8.5.: Neutron separation matrices obtained with the BayesWCP method.

7 dp		Incoming Neutrons				
600 MeV		1n	2n	3n	4n	5n
Detected Multiplicity	0 n	71	41	23	13	10
	1 n	21	27	23	17	12
	2 n	7	23	32	32	28
	3 n	1	7	15	22	25
	4 n		2	6	11	16
	5 n			2	5	10

7 dp		Incoming Neutrons				
600 MeV		1n	2n	3n	4n	5n
Detected Multiplicity	0 n	43	11	4	4	8
	1 n	40	26	11	4	1
	2 n	16	45	36	20	10
	3 n	1	17	34	33	23
	4 n		1	12	25	28
	5 n			2	13	29

7 dp		Incoming Neutrons				
600 MeV		1n	2n	3n	4n	5n
Detected Multiplicity	0 n	25	3	2	4	8
	1 n	53	17	3	1	
	2 n	22	63	31	10	4
	3 n	1	17	54	33	14
	4 n			10	40	32
	5 n				11	42

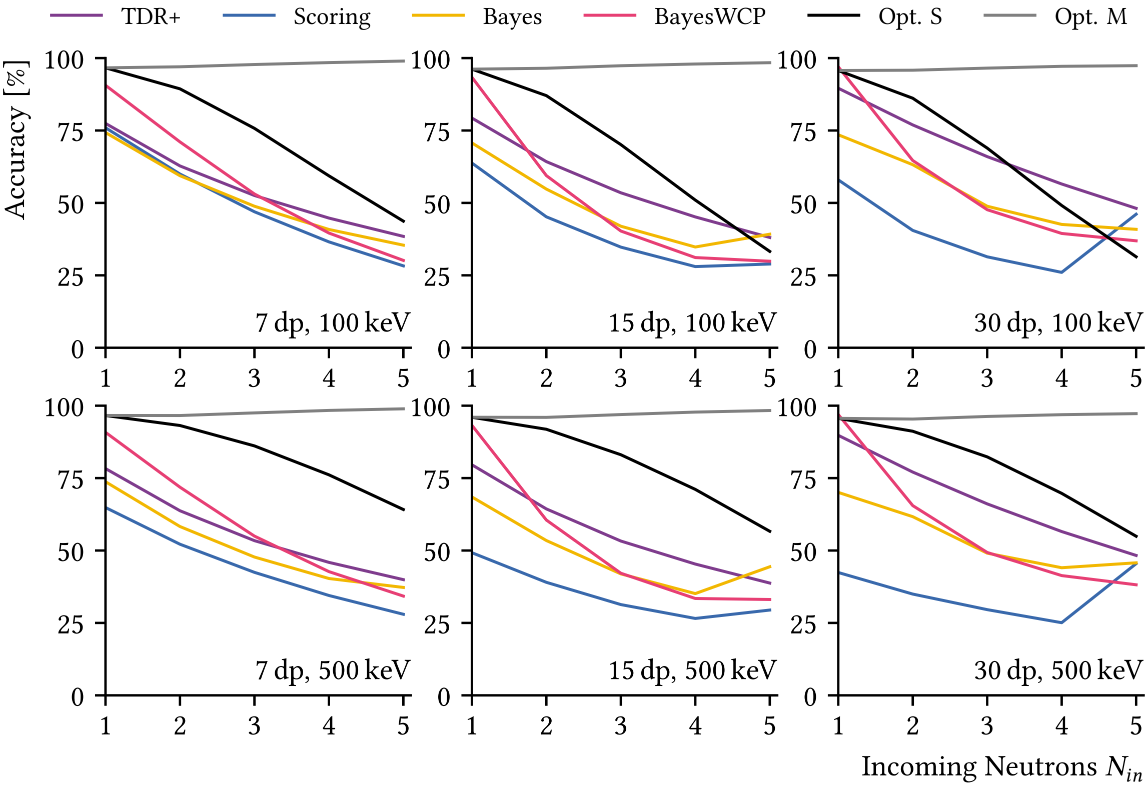

FIGURE 8.3.: Accuracy of the determination of reacted neutrons N_{reac} as a function of the number of incoming neutrons N_{in} for 7, 15, and 30 double planes. For low relative energies, the hits occur close together and get absorbed into one cluster. Even an optimal reconstruction algorithm will fail if each cluster can only be selected once (Opt. S). If clusters can be selected multiple times (Opt. M), this issue is resolved. This is not a problem for the TDR and Bayesian multiplicity determination, as they do not depend on single clusters. The scoring method performs worse for higher number of double planes and larger neutron spread, because too many clusters reach the minimum score.

If an event-by-event reconstruction of the multiplicity is not required, the experimental histogram of the total deposited energy could be decomposed as fraction of the distributions shown in Figure 7.3. That is, a weighted sum of histograms for individual numbers of incoming neutrons should be able to reproduce any experimental histogram.

A comparison of the detected multiplicity to the number of reacted primary neutrons is more valuable. In Figure 8.3, the probability for the correct assignment ($\Delta N = N_{reac} - N_{reco} = 0$) is given as a function of the number of incoming neutrons N_{in}.

On first glance, there seems to be an unexpected behavior: The “cheating” reconstruction method does not seem to be able to pick the correct number of clusters, dropping even below 50 % for 5 neutrons for the low spread at a relative energy of 100 keV.

This can be explained by a simple fact: Neutrons impact too close together and are gathered into a single cluster. For four incoming neutrons and 15 double planes, just 82 % of clusters include only a single neutron. If an optimal reconstruction algorithm can select clusters multiple times, the correct number of neutrons is obtained in almost all cases.

The 2DCalibr method does not care about one or two fewer clusters and provides the multiplicity independent of distance or neutron spread. While its accuracy drops for lower number of double planes, it is overall quite solid — significantly better than expected given the E_{tot} and N_{clus} distributions in Figure 7.3. Reduced calorimetric properties of NeuLAND are, while noticeable, not the main problem. The main problem is simply the underlying reaction probability, as neutrons that do not have reacted cannot be detected. Thus, the number of incoming neutrons cannot be reliably determined on an even-by-event basis if the detector depth is too small. While the solution to this is building more double planes, any number of double planes should be used optimally by the reconstruction software.

The Bayes method follows the 2DCalibr methods closely, with some differences at five neutrons. Here, the 2DCalibr method is limited, i.e., everything above the last cut is thrown away. This could be replicated by including the hypothesis for 6n.

The BayesWCP and the Scoring method seem to be worse, especially for larger number of double planes. As both use the probabilities of each clusters only once, they count either too few clusters if the minimal score is high, or too many for a lowered score. While this simple $\Delta N = 0$ metric seems worse in these cases, it already reflects how good the reconstructed interactions points are, which is not the case for the 2DCalibr method.

8.4.2. CLUSTER SELECTION

The question "Is this cluster a primary cluster?" is a binary classification. For NeuLAND, the *total population* consists out of primary clusters (*condition positive*) and secondary clusters (*condition negative*).

To judge solely the cluster selection part, the algorithms were supplied with the correct number of clusters, which then calculate the *predicted condition* for each cluster.

In the terminology of predictive analysis, these classifications can be divided into the four groups of a confusion matrix: *True positive TP*, *False positive FP*, *False negative FN*, and *True negative TN*. From there, several derived values can be defined:

The *precision* or *positive predictive value*

$$PPV = \frac{\text{True Positive}}{\text{Predicted Condition Positive}} = \frac{TP}{TP + FP} \tag{8.6}$$

The *sensitivity* or *true positive rate*

$$TPR = \frac{\text{True Positive}}{\text{Condition Positive}} = \frac{TP}{TP + FN} \tag{8.7}$$

and the *accuracy*

$$ACC = \frac{\text{True Positive + True Negative}}{\text{Total Population}} = \frac{TP + TN}{TP + TN + FP + FN} \tag{8.8}$$

are measures for the quality of the algorithm. The so-called *F_1 score*, which is the harmonic mean of precision and sensitivity, tries to combine all measures into a single value.

In the best case, all these indicators should be 100 %. Achieving both high precision and high sensitivity at the same time might not always be possible, and trade-offs might be necessary. For the resulting spectra, false positives reduce the resolution and false negatives reduce the efficiency.

Results for 15 double planes are shown in Table 8.6. Note that the values are for the classifications of individual clusters, not for the reconstruction of the whole set. As these values enter exponentially for higher number of neutrons, small changes can have a huge impact on the results, see below.

The TDR cluster selection performs well at few neutron events, the strategy of always taking the first clusters works well in this scenario. The advantage is quickly lost however, both precision and sensitivity drop significantly for four and five incoming neutrons.

The scoring algorithm has a high threshold applied, which leads to a high precision, but deficits in sensitivity. While both values are effectively constant for all numbers of incoming neutrons, they seem to fall behind the TDR method.

For few neutrons, the Bayes method is worse than the TDR method. This changes at three incoming neutrons, where it pulls slightly ahead.

8.4.3. RELATIVE ENERGY SPECTRA

The most relevant challenges are relative energy spectra created with the reconstructed neutrons. Information on the beam-like heavy fragment is needed to calculate the invariant mass, which was pulled directly from the Monte Carlo data here.

Figure 8.4 shows the resulting spectra for 7, 15, and 30 double planes at a distance of 14 m for one and two incoming and reconstructed neutrons and Figure 8.5 for three and four neutrons.

As the combination of multiplicity and cluster selection, these spectra reflect the properties discussed above.

Table 8.6.: Cluster selection performance for the TDR, Scoring, and Bayesian method. The correct number of primary clusters was supplied from the outside. For each number of incoming neutrons, the confusion matrix (CM) and the resulting values for the accuracy, precision, sensitivity and the F1 score are given in [%]. See text for details.

15 dp@14 m, 600 MeV, 500 keV TDR w/ perfect number of clusters					
N_{in}	CM [1e3]	Acc.	Prec.	Sens.	F1
1n	62 18 17 201	88	78	79	78
2n	110 46 48 401	85	71	70	70
3n	153 75 80 598	83	67	66	66
4n	192 106 109 790	82	64	64	64
5n	227 138 137 971	81	62	62	62

15 dp@14 m, 600 MeV, 500 keV Scoring w/ perfect number of clusters					
N_{in}	CM [1e3]	Acc.	Prec.	Sens.	F1
1n	37 18 42 202	80	67	47	55
2n	88 42 70 405	82	68	56	61
3n	132 64 100 609	82	67	57	62
4n	170 83 131 812	82	67	56	61
5n	199 98 166 1011	82	67	55	60

15 dp@14 m, 600 MeV, 500 keV Bayes w/ perfect number of clusters					
N_{in}	CM [1e3]	Acc.	Prec.	Sens.	F1
1n	51 21 28 199	84	71	64	68
2n	100 46 58 400	83	68	63	66
3n	149 75 84 598	82	67	64	65
4n	192 101 109 795	82	66	64	65
5n	224 119 140 990	82	65	62	63

For one neutron all methods deliver good results — a complicated reconstruction algorithm is not required here. The TDR method even manages to reach the optimum for 30 double planes, while the other methods fall behind, especially the scoring method due to the minimal score requirement.

For two neutrons, the distance to the ideal reconstruction is already substantial. At 100 keV excitation energy, the TDR method starts to lose its advantage for 7 and 15 double planes. Note that the peak height for all methods is around the same fraction of the ideal peak in most cases.

For three neutrons and seven double planes, the TDR method falls massively behind at low E_{rel}, and at four neutrons, its is unusable for 7 and 15 double planes.

Overall, the TDR+ method works well for few neutrons or high numbers of double planes, while the Bayesian method works in all cases and provides better multi-neutron reconstruction. Also, Scoring and Bayesian method require specific input for each combination of energy, detector size, and distance to the target. These parts make them more flexible, but also more prone to failure. Input parameters for the Bayesian method can be produced with little effort, which makes it the prime candidate for multi-neutron event reconstruction with NeuLAND.

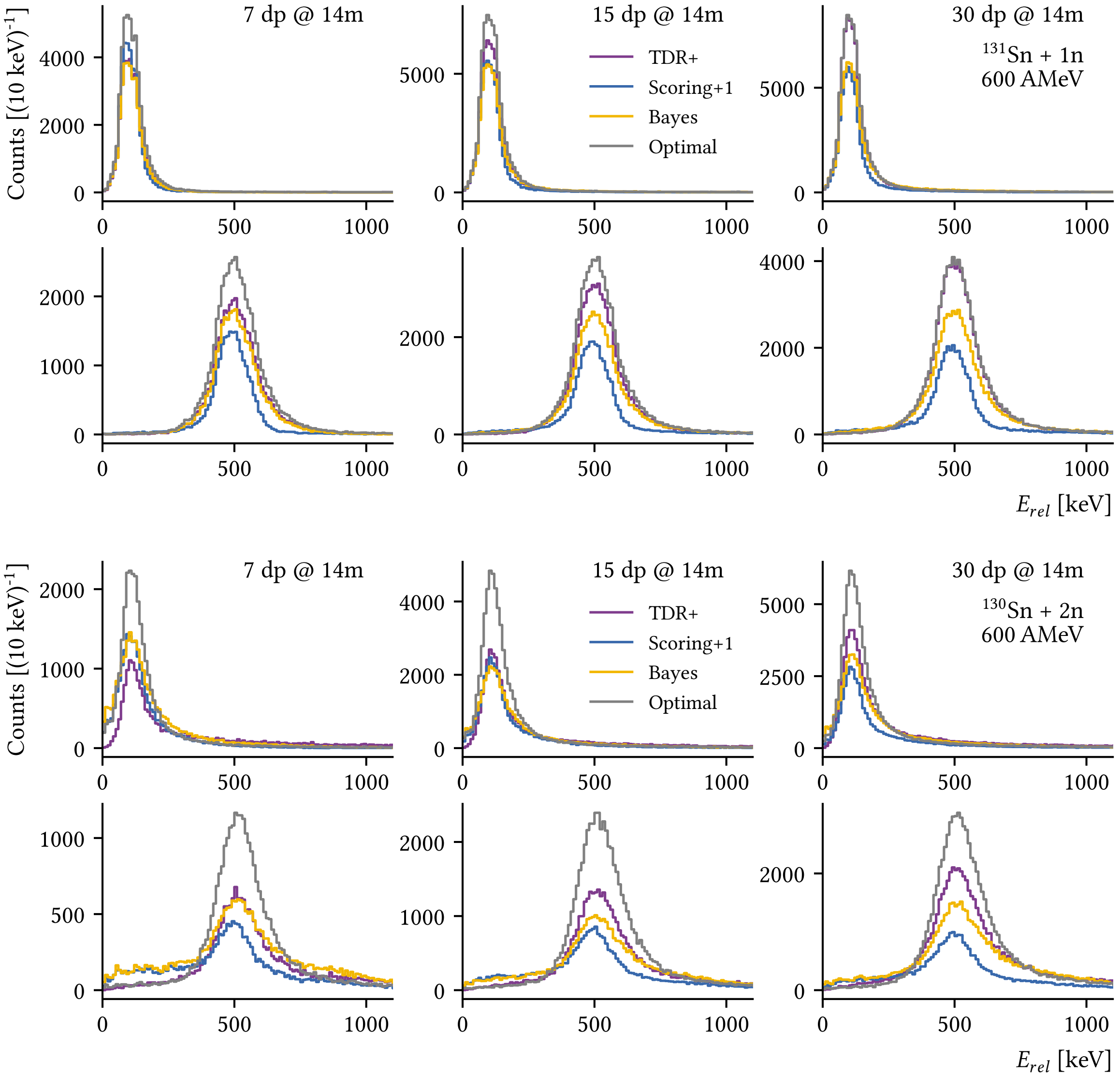

Figure 8.4.: Relative energy spectra for the decay of ^{132}Sn emitting one and two neutrons at 100 keV and 500 keV detected by 7, 15, and 30 double planes at a distance of 14 m from the target.

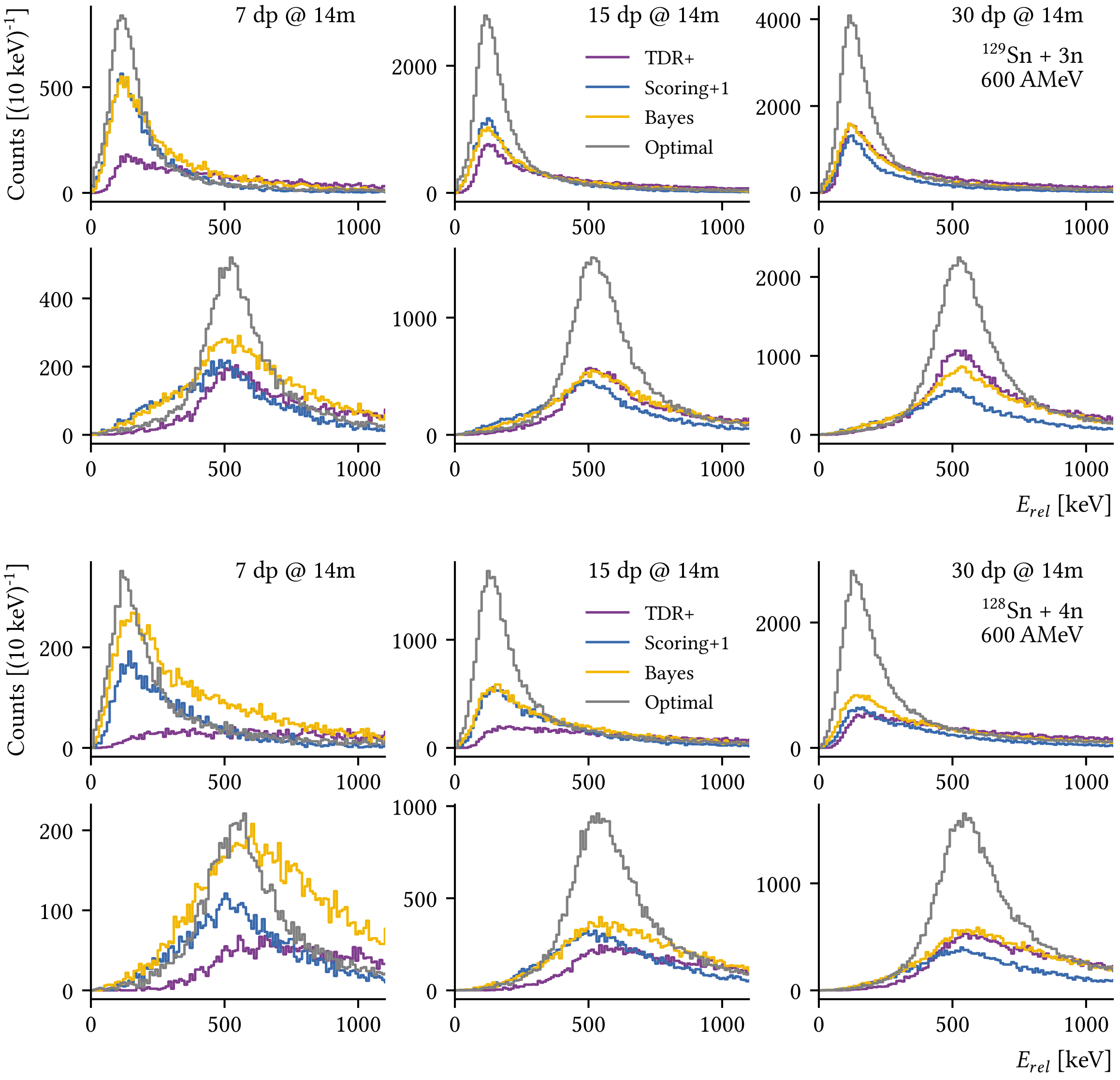

FIGURE 8.5.: Same as Figure 8.4, but for three and four emitted neutrons. Note how the performance of the different algorithms changes with the different parameters.

CHAPTER 9.

NEURAL NETWORKS

In the previous chapter, the original reconstruction algorithms with hard cuts and a strict sorting procedure was advanced to determine probabilities based on likelihoods of cluster features. These features, however, were still manually selected. The next evolution step would be to let the computer find the relevant connections between the individual hits on its own via *Machine Learning*.

Machine learning with *Neural Networks* has been in vogue for a few years. Large companies like Google and Microsoft spend massive amounts of effort on developing neural networks for their services — fortunately, they have released their frameworks to the public. Together with affordable, high-performance hardware, machine learning can now be used in many applications. In this chapter, ways to integrate neural networks into the R3BRoot infrastructure for event reconstruction of NeuLAND are shown.

9.1. FROM THE BRAIN TO TENSORS

The original idea for neural networks was once based on the human brain: Lots and lots of simple, independent neurons receive signals from many other cells and, depending on the input, send signals out [55, 56].

In the world of machine learning, this is abstracted: Here, a neuron calculates the weighted sum of all its inputs, adds a constant bias, and feeds it into a non-linear activation function. If the weights and biases are chosen correctly, the output layer (the last nodes in a connected network) hopefully shows a meaningful result. In the case of a classification, one neuron should emit a strong signal, indicating the predicted class for the input. For full in-depth discussions of neural networks see for example [57–59].

Google TensorFlow[1] has earned a lot of renown, e.g., recently for its contribution to beating the world's best human players at the game Go [60]. As the name suggest, the operations mentioned above are implemented as operations on tensors.

---

[1] `https://www.tensorflow.org/`

The most basic network uses few components. The input tensor X, also called *feature*, is filled with the data to process. These could be, for example, the pixels of a picture. Each node connected to this input layer, calculates the sum with weights W and biases b for additional degrees of freedom:

$$L = X \cdot W + b \tag{9.1}$$

These sums are then passed to an activation function and normalized, for example the nonlinear *softmax*:

$$\text{softmax}(L_n) = \frac{e^{L_n}}{||e^L||} \tag{9.2}$$

Without further layers, the result of this process is the prediction vector:

$$Y_{pred} = \text{softmax}(X \cdot W + b) \tag{9.3}$$

With good weights and biases, these predictions should be reasonable.

To get to this point, the network must be trained. Input data with known *labels* for the features is filled in the input tensor. The prediction made by the network is then compared to the correct result by calculating the *distance*, which is often done with the cross entropy:

$$\text{CrossEntropy} = -\sum Y_{real} \cdot \log(Y_{pred}) \tag{9.4}$$

Other functions, like the Euclidean distance, can work as well. Now, this distance needs to be minimized. TensorFlow provides several optimizers, e.g., a gradient descend optimizer. This gradient, with all its partial derivatives, can be followed a small step. It modifies the weights and biases in such a way that for the next inputs, the prediction is (hopefully) better.

There are many more terms and ideas: Often, many inputs are processed in one batch. Each input in the batch runs through the same neurons with the same weights and biases. *Deep* neural networks have additional hidden layers, commonly with other activation functions like *relu* or *sigmoid. Convolutional* neural networks use known geometric structures in the input, e.g., the pixel grid in a picture. This can have great benefits were shape and position are important.

9.2. Concepts for event reconstruction with Neural Networks

The purpose of NeuLAND, as stated before, is to find all primary neutron interaction points. In principle, a well-constructed neural network should be able to do exactly this — finding objects like people, cars, and digits in pictures is a common application.

NeuLAND can be seen as a 3D picture: Due to the dimensions of the scintillator bars, the introduction of “pixels” with border lengths of 5 cm by 5 cm by 5 cm is natural. With 30 double planes, this would result in a 50x50x60 grid. At two dimensions per pixel for energy and time, saved as 32-bit floating points, the neural network input placeholder is 1.2 MB in size. This seems to be acceptable, as an uncompressed HD picture is about $1920 \cdot 1080 \cdot 3 \cdot 32\,\text{bit} \approx 25\,\text{MB}$ large.

In a perfect scenario, the neural network would immediately show the four-momenta for each primary neutron interaction point. The output layer could also either be the same grid to indicate the position of the predicted interaction points, or just the multiplicity. With the necessary hidden layers and 3D convolutions and their weights and biases, the memory requirements quickly escalate. Modern consumer graphics cards often have 4 GB to 8 GB of RAM, which limits the batch size. With the rise of neural networks, computer manufacturers have responded and offer specialized GPUs and systems. A study conducted at the Chalmers University of Technology [61] used a network with a total size of 2 GB. The achieved accuracy of $\approx 75\,\%$ is unfortunately not representative, as input data was not simulated with R3BRoot and is missing vital physics interactions and the digitization process. In addition, it was found that the necessary 3D convolutions are quite slow.

While the fully-fledged 3D representation should offer the best results, other approaches might also be viable. A big physical problem of the pixel grid method is the high number of “dead” pixels. With the current hardware, each bar only produces one hit per event, i.e., at most one out of 50 pixels will have data. In addition, not every bar will see an energy deposition. Thus, the input for the neural network is zero in most case, which then requires an enormous amount of training data such that each pixel is properly trained with.

This problem could be mitigated by reducing the data beforehand, for example by eliminating one dimension. As the interaction patterns in NeuLAND should be rotation symmetric around a centered z-axis, the x and y values could be merged into one, e.g., $r = \sqrt{x^2 + y^2}$. Alternatively, the position information could be eliminated entirely, and input organized by paddle id. With energy, time, and position in the bar, this would reduce the input size to 9000.

A completely different approach could be cluster classification. Here, the neural network would be shown single clusters on a tiny 3D or 2D grid and asked to predict the number of primary interaction points it contains (none, one, many). This would keep the position information at least somewhat intact, while reducing the input size.

Normalization of time and energy values might also be a critical point for all these approaches. Mapping both to a $[0:1]$ interval, with cutoff and offset correction if necessary, could help stabilize the network.

9.3. DATA TRANSFER FROM ROOT

The Monte Carlo simulations with R3BRoot can produce infinite amounts of training data. However, the system running the training or later the reconstruction might not be able to run R3BRoot or even ROOT itself. Therefore, the data format must be changed.

In this thesis, Google Protobuf[2] was successfully used: “Protocol Buffers (a.k.a., protobuf) are Google’s language-neutral, platform-neutral, extensible mechanism for serializing structured data.” [62] Protobuf is included in FairSoft, i.e., it is immediately available on any system using R3BRoot. The data structure described with Protobuf files can be parsed by many languages, including C++ for R3BRoot and Python for TensorFlow. In Listing 3, the Protobuf data structure for NeuLAND is shown.

Two methods of data exchange have been tested: Conversion to file and direct transfer over network. Reading and saving protobuf events from and to file is achieved by using a streaming library in python, appropriately named `pystream-protobuf`[3]. Files including streams of protobufs are quite handy for training purposes, as they can be sent to the training machine and reused with ease.

While protobufs can be written to disk, the serialized objects can also be sent over the network via a messaging protocol. Messages can be sent with `ZeroMQ`, which is also part of FairSoft, over TCP to a server, which processes the request and send a reply. For the application of event reconstruction, R3BRoot could be client which connects to a machine running a neural network as a service. This was implemented as part of this thesis. A R3BRoot client running at the Institute for Nuclear Physics, University of Cologne successfully send events over the Internet to the authors PC at home and received the predicted multiplicity back.

During these tests, a problem appeared: R3BRoot is currently built to fully process one event at a time. After sending one event on its way, the process is blocked while waiting for a response. The round-trip time over the Internet is small, but as it occurs for every single event, it completely obliterates the large advantage the PC’s GPU has over the CPU based server. In addition, the neural network is built to handle inputs in batch, up to hundreds of events at a time, which is not compatible with the one-event-after-the-other approach. Even if the systems are located next to each other, it is more efficient and robust to convert the ROOT file to a protobuf file, run it through the neural network, convert the result back to a ROOT file, and read it into R3BRoot. This assessment might change in the future, as messaging solutions within FairRoot are under development [40].

---

[2] `https://github.com/google/protobuf`

[3] `https://pypi.org/project/pystream-protobuf/`

9.4. Results

A very small neural network was created as a baseline and to test the input-output capabilities, the core is shown in Listing 2. It takes the time and energy of each paddle side-by-side, both normalized linearly to $[0:1]$, and feeds them directly into a softmax output layer with size six to classify zero to five reacted neutrons.

It was trained and evaluated with different sets of simulated data with one to five 600 MeV neutrons on 30 double planes in 14 m distance. For training, 5×10^5 events were randomly shuffled and fed through the networks over 50 epochs. After training, the whole network was saved to disk and loaded in a separate script for evaluation, where the same data from Chapter 8 for the decays of ^{138}Sn was used. TensorFlow 1.9 ran on a system with Windows 10, Python 3.6, CUDA-Toolkit 9.0, and cuDNN v7.0 using a GeForce GTX 1050 Ti 4GB.

With its small number of only 36 006 variables, the network reaches an average accuracy of 42(2) % for training data, which is surprisingly high for such a tiny network. Training accuracy, loss, and accuracy of the multiplicity prediction for the evaluation data is shown in Figure 9.1. The reconstruction accuracy stays significantly below any method presented in Chapter 8.

```
# Input: 30 double planes * 100 paddles per double plane * 2 channels
# Output: Multiplicity classification: 0-5 neutrons -> 6 Classes
x_size = 30 * 100 * 2
y_size = 6
# Placeholders for train data
X = tf.placeholder(tf.float32, shape=[None, x_size])
Y_real = tf.placeholder(tf.float32, shape=[None, y_size])
# Variables & Biases
W = tf.Variable(tf.truncated_normal([x_size, y_size]))
b = tf.Variable(tf.zeros([y_size]))
# Model
Y_pred = tf.nn.softmax(tf.matmul(X, W) + b)
# Cross Entropy
cross_entropy = -tf.reduce_mean(Y_real * tf.log(Y_pred))
# Training
train_step = tf.train.GradientDescentOptimizer(0.4).minimize(cross_entropy)
```

Listing 2.: Core of the smallest neutral network for multiplicity prediction. Energy and time information are normalized and placed side-by-side for all paddles.

A single hidden layer with 500 `relu` nodes already delivers a performance close to the TDR/2DCalibr method. Larger hidden layers of 750 nodes and more do increase the accuracy for the training data, however with only marginal effects for the evaluation data set. This indicates overfitting, i.e., the neural network is starting to memorize specific events instead of

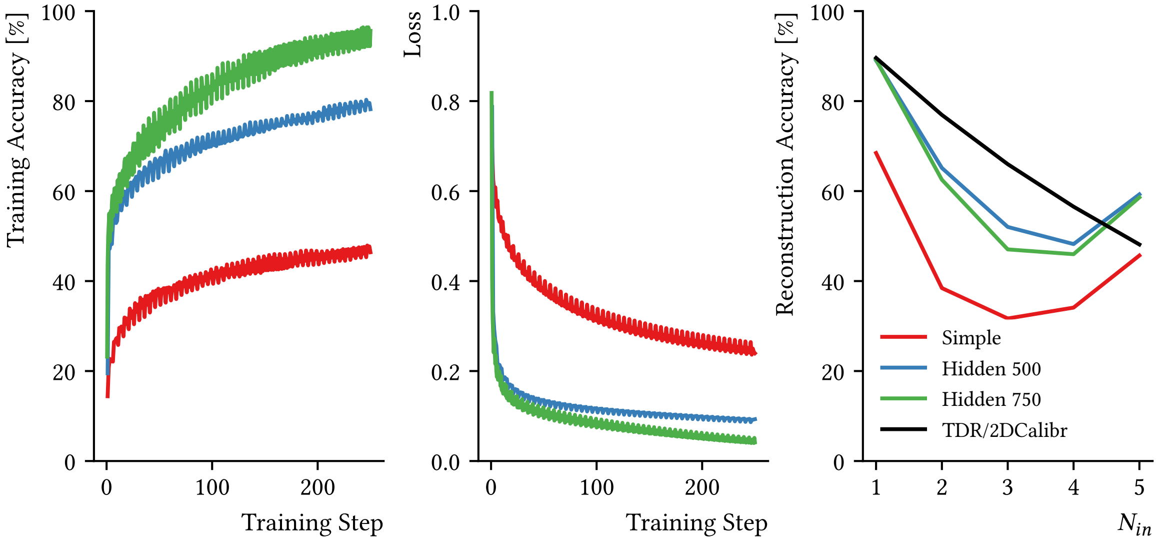

FIGURE 9.1.: Accuracy and loss during training and multiplicity reconstruction efficiency for the simple neural network and added hidden layers with 500 and 750 nodes, respectively. The hidden layer drastically improves the performance of the network with its large number of variables. While more nodes in the hidden layer increase the accuracy for the training data, this does not translate to better multiplicity prediction.

creating an abstract model valid for any type of event. If the hidden layer is increased to 1000 nodes, the network no longer converges, and training fails for currently unknown reasons.

These immediate results motivate further investigations of neural networks for NeuLAND. From here on out, many options can be considered: From the input, like more or different training data and other normalizations, over the network structure, with more and larger layers or more and different hidden layers, to the cost function and optimizers. A systematic study of these parameters could very well lead to an enormous jump in accuracy and efficiency for all NeuLAND related data analysis.

While accurate multiplicity is already quite valuable, the cluster selection or interaction point determination could also be performed by neural networks. The required changes to the output layer are massive, as an entirely different approach must be taken. However, with the progress made in other applications, this project seems feasible.

If the messaging infrastructure can be developed further to minimize the overheads discussed above, a single GPU based server with the proper network could provide a reconstruction service to the whole R^3B collaboration.

CHAPTER 10.

SUMMARY AND OUTLOOK

The New Large Area Neutron Detector NeuLAND will be the world's best neutron detector for high energy neutrons between 100 MeV to 1000 MeV. It will provide the multiplicity and the energy of neutrons from Reactions with Relativistic Radioactive Beams (R^3B) at the Facility for Antiproton and Ion Research (FAIR).

Over the last six years, elements of the detector have been built by groups from the universities of Frankfurt, Darmstadt, and Cologne as well as from the GSI. The assembly process is almost exclusively performed in-house at GSI; it is reported on here. The so-called double planes are composed of 100 organic scintillator bars with a length of 2.5 m. Each bar is tested for its light generation and light transport capabilities. After many bars were rejected in the beginning, a clear increase in quality has been reached. Photomultiplier tubes are equipped with mounts and plugs and attached to both ends of the bars. The frames of the double planes hold the scintillator elements and high voltage as well as signal cables. Data acquisition modules are located on top of each frame, supporting 200 channels per plane. The final detector will consist of 30 double planes, 11 of which have been assembled.

During the shutdown at GSI, four double planes were shipped to Japan, where a successful three-year experimental campaign took place. Here, NeuLAND gathered data over 71 days of beamtime in 12 experiments.

The R^3B experiment uses the software R3BRoot, in which NeuLAND simulation and reconstruction classes have been integrated as part of this thesis. The primary particles, including the primary neutrons that must be reconstructed later, are handed off to the Monte Carlo transport codes. It was shown that for few double planes, the probability to detect high neutron multiplicities is severely affected. Only for more than 15 double planes do all out of four or five incoming neutrons react at least every other event. When the primary neutrons interact in NeuLAND, they produce even more neutrons, which in turn produce even more particles.

Charged secondary particles deposit energy in the scintillator. A digitizer collects these energy depositions and transforms them to hits which should look like experimental data. It could be shown that the re-implemented digitizer for the electronics used in Japan is fully able to reproduce the characteristics of the measured data, which had been a problem before.

This could be achieved by modeling each influence on the final value separately, including light emission, transport, and collection as well as photomultiplier and electronic response and calibration.

The experiments in Japan also included an efficiency measurement, which was recreated in the R3BRoot software with the correct geometry. Simulations with the three relevant physics models included in Geant4 were compared to the experimental values. No clear recommendation can be given, as the experimental data falls in the surprisingly large gap between the models.

Detector hits are grouped together to clusters. In the scope of this thesis, an efficient templated clustering algorithm was created, which might also find application elsewhere. Properties of primary and secondary clusters were analyzed, and several different behaviors were discovered — differences that can be exploited to select the correct clusters during event reconstruction. In particular, a method to determine the primary neutron energy from proton Bragg-tracks was developed.

Neutron multiplicities and interaction points must be reconstructed for each event, for which three distinct algorithms were developed and tested. The method originally proposed for the full detector has known problems with reduced detector depth, but these have a different origin as expected. While the calorimetric properties are reduced, the accuracy of the multiplicity determination is only marginally affected. Instead, the simple cluster selection algorithm cannot deal with the combination of hurdles: Reduced detector depth, short distance to the target, and clumped primary interaction points. It is important to differentiate the number of reacted neutrons from the number of incoming neutrons and judge the performance accordingly.

To alleviate this problem for experiments in FAIR Phase 0, where 7 to 15 double planes will be operational with new electronics, two new methods were developed. Both use the differences between primary and secondary clusters. The scoring method increases or decreases cluster scores according to manually implemented rules, also including relations between clusters and proton tracking. The feature distributions of primary and secondary clusters also act as likelihoods in the scope of Bayesian statistics. Provided with simulated distributions for the specific experiment, probabilities for clusters and multiplicities can be calculated.

The impact on the resulting relative energy histograms is huge, as shown in Figure 10.1. For the upcoming experiments in FAIR Phase 0 and beyond, this could make all the difference. Still, there is a lot of room for improvement. With the perfect algorithm, efficiency could be doubled without additional cost.

The next natural step leads to machine learning. Simple neural networks were tested for event reconstruction and the necessary software infrastructure was developed. By converting the events from ROOT to Google Protobuf, data transfer to the network is significantly simplified. A neural network with one hidden layer can predict the multiplicity almost as well as the classical methods listed above. This motivates a separate project for further developments

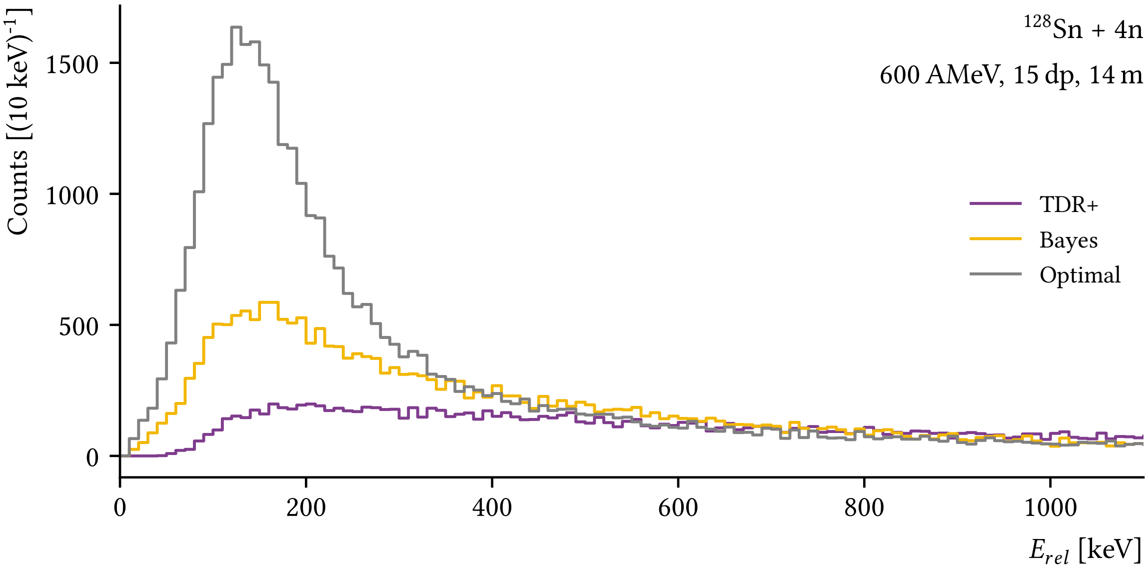

Figure 10.1.: Relative energy spectrum for four neutrons with 600 MeV impinging on 15 double planes, reconstructed with the TDR+, the Bayesian, and an optimal method. While there is no clear peak visible for the TDR+ method, the Bayesian method delivers a clear peak with an acceptably right tail.

in this direction in the future. If successful, the network could even take over the cluster selection process.

LAND, the predecessor of NeuLAND, was built in 1990 and used for an experiment in Russia this year. Both detector hardware and the software created as part of this thesis are the foundation for 25 and more years with NeuLAND, first in FAIR Phase 0, then in Phase 1, and beyond.

PART II.

THE VIRTUAL γ-RAY SPECTROMETER G4HORUS

> “I have yet to see any problem, however complicated, which, when you looked at it in the right way, did not become still more complicated.”
>
> *Poul Anderson*[a]

---

[a] Also known as *Anderson's Law* [63, p. 246]

CHAPTER 11.

INTRODUCTION

The absolute full-energy-peak (FEP) efficiency is a very important attribute of many setups measuring γ-rays. It can be determined experimentally using standardized calibration sources:

$$\epsilon(E_\gamma) = \frac{N_\gamma}{I_\gamma \cdot \tau \cdot A \cdot t} \tag{11.1}$$

Where a source with an activity A emits γ-rays at an energy E_γ with an intensity I_γ, which results in a peak with volume N_γ in the spectrum measured over a time t with a detection system dead time correction τ.

Alternatively, the efficiency can be determined with Monte Carlo simulations, where M γ-rays are emitted, and a spectrum of the deposited energy is produced.

$$\epsilon(E_\gamma) = \frac{N_\gamma}{M} \tag{11.2}$$

G4Horus provides a ready-to-use GEANT4 based application for simulating the efficiency of detectors used at the Institute for Nuclear Physics, University of Cologne. In addition, it can produce listmode-style data in the form of ROOT ntuples and SOCO-v2 event files, which allows for investigations of complex coincidence measurements.

11.1. γ-RAY SPECTROSCOPY WITH HORUS

Located at the 10 MV FN-Tandem accelerator at the Institute for Nuclear Physics, University of Cologne, the γ-ray spectrometer HORUS (High-efficiency Observatory foR Unique Spectroscopy) is used to investigate the structure of nuclei and measure cross sections to answer questions in nuclear astrophysics. It consists of up to 14 HPGe detectors, six of which are equipped with active anti-Compton BGO shields [64]. Signals from the detectors are processed by XIA's Digital Gamma Finder 4C Rev. F, which allows for acquisition of so-called *listmode* data, where coincident hits in different detectors can be correlated to events. Matrices with correlated data from γ-ray cascades can be obtained by *sorting* these events.

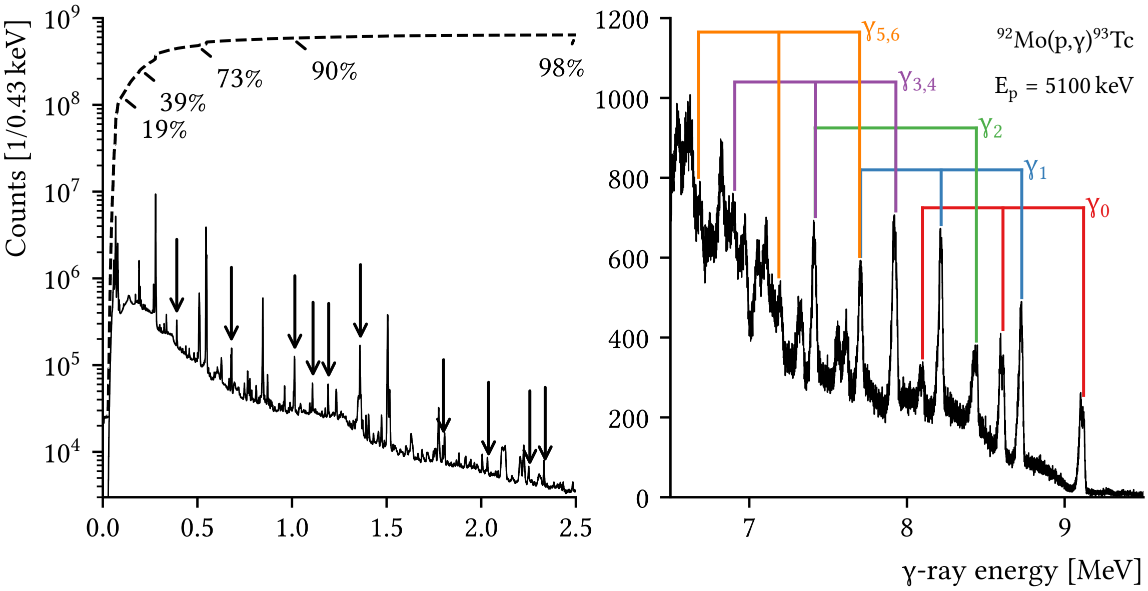

FIGURE 11.1.: Low and high energy part of a γ-ray spectrum obtained with a HPGe detector from a proton capture experiment for nuclear astrophysics [68]. In the low energy part, the running sum of counts (dashed) shows that about 40 % of all counts are contributed by the broad background in the range of 0 keV to 200 keV — all before even a single line of interest from the reaction product (marked with arrows) is included. In the high energy part, the primary transitions to the ground (γ_0) and excited states (γ_i) and their single and double escape peaks are marked, some of which overlap.

For example, γγ coincidences can be used to investigate quadrupole and octupole states [65], or low-spin structures [66]. In addition, high energetic γ-rays, which are emitted after capture of protons or α-particles, can be used to determine total and partial cross sections for nuclear astrophysics [67, 68]. An example for spectra obtained in such an experiment is shown in Figure 11.1. Recently, particle detectors were added with the SONIC detector array [69]. The resulting particle-γ coincidences are used for lifetime measurements with the DSAM technique [70] or to investigate the Pygmy Dipole Resonance [71].

11.2. SIMULATION OF EFFICIENCIES

Monte Carlo simulations of γ-ray detectors are well established [72–75]. γ-ray interactions between 20 keV and 20 MeV are known well enough for most simulation purposes, especially when compared to the description of hadronic interactions, see Figure 6.4.

The main difficulty for HPGe detector simulations is summarized well in [76, p. 117]: "The accuracy of Geant4 simulations is heavily dependent on the modeled detector geometry. Characterizing a detector is difficult, especially if its technical characteristics are not well known."

There are exceedingly many specialized publications addressing simulations of HPGe detectors, which study, e.g., high-precision efficiency determination [72, 77], summing corrections [76], or background sources [78].

However, plain simulations of the FEP efficiency of single γ-ray detectors might not always be necessary. In other kinds of publications, the whole simulation process is sometimes reduced to, e.g., "Monte Carlo simulations with Geant4 were performed [...] and were compared to the experimental efficiencies [...]. The simulation describes the experimental efficiencies very well." [79, p. 5]. Statements of this type, without any information about the implemented geometry, physics, procedure, evaluation, *adjustments* and *corrections*, or even just the Geant4 version used, are not particularly meaningful. This can induce the sentiment that these simulations were seen as unnecessary and performed peripherally just to "tick some boxes".

Under certain conditions, this can be a fair assessment: Many γ-ray transitions are found at energies between, e.g., 200 keV to 2000 keV, where also many calibration lines are located and the detection efficiency is both large and less affected by materials of the target chambers, see Figure 11.2 and Section 13.3. Efficiency simulations in this energy range are rarely critical for the success of experiments, and rather act as an additional check of the measured calibration points during data evaluation.

The efficiency peak at lower energies is quite challenging to reproduce as even minuscule amounts of inactive material, e.g., the germanium dead layer [76], have an enormous impact. Thus, either a lot of work is put into the geometry descriptions [75], or this part of the energy range is simply ignored [79]. In principle, effects of noise and data acquisition settings on the tiny signals must be accounted for as well. Material in front of the detector can also be used deliberately to filter low-energy γ-ray, see Section 13.3.

Efficiency curves of different HPGe detectors can look quite similar in the energy range from 500 keV to 3000 keV, see Figure 11.3. If the absolute efficiency of the setup is not reproduced immediately, e.g., due to imprecise geometry implementation or uncertainties of the distance to the target, scaling is sometimes used to match the experimental calibration data. In this case, the scaled simulation will thus match the experimental data in this range *anyhow*, rendering it (and the work involved) superfluous. A simple fit of an appropriate function could give the same outcome, as long as no interpolation to other energy regions is required.

To summarize: Reproducing the efficiency of a single detector is exceedingly difficult at low energies and easy but superfluous at medium energies. This raises the question: When are simulations beneficial or even necessary? In general, simulations are performed to support the data evaluation, predict the performance of planned experiments, and foster the

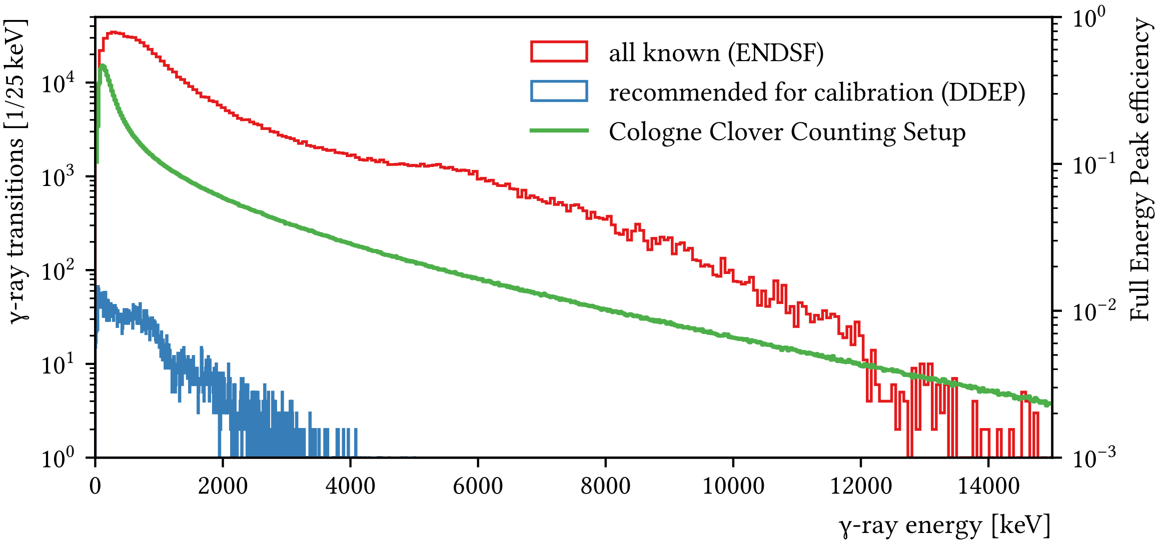

FIGURE 11.2.: Histograms of all known γ-ray transitions extracted from ENSDF data [80] and recommended transitions for detector calibration from DDEP data [81] compared to the simulated efficiency of HPGe detectors using the example of the Cologne Clover Counting Setup [82]. Most known γ-ray transitions occur below 2 MeV with a sharp drop-off in frequency after 6 MeV. Note that the calibration data includes nuclides with all half-lives as well as lines with less than 0.001 % intensity. Even though, only few calibration points are available above 3.5 MeV.

overall understanding of the detection and analysis systems and procedures. Here, the focus lies on efficiency determination at energies were calibration points are scarce. In addition, interactions of many detectors in complex systems can be simulated and recommendations for future developments and improvements are made.

11.3. γ-RAY DETECTION EFFICIENCY AT HIGH ENERGIES

Standard sources of not-too-short lived ($T_{1/2}$ > months) radioactive isotopes provide easily accessible calibration points up to 3.5 MeV and thus are commonly used for both energy and efficiency calibration.

In cases where efficiencies at only slightly higher energies are needed, e.g., up to 5 MeV, short-lived (seconds to minutes) sources can be produced on-site and then quickly measured by the detection setup — an involved process which can detract from the main experiment. Table B.1 lists recommended radioactive sources for efficiency calibration with energies over 3 MeV, most of which can be disregarded due to their short half-live, meager emission intensity for

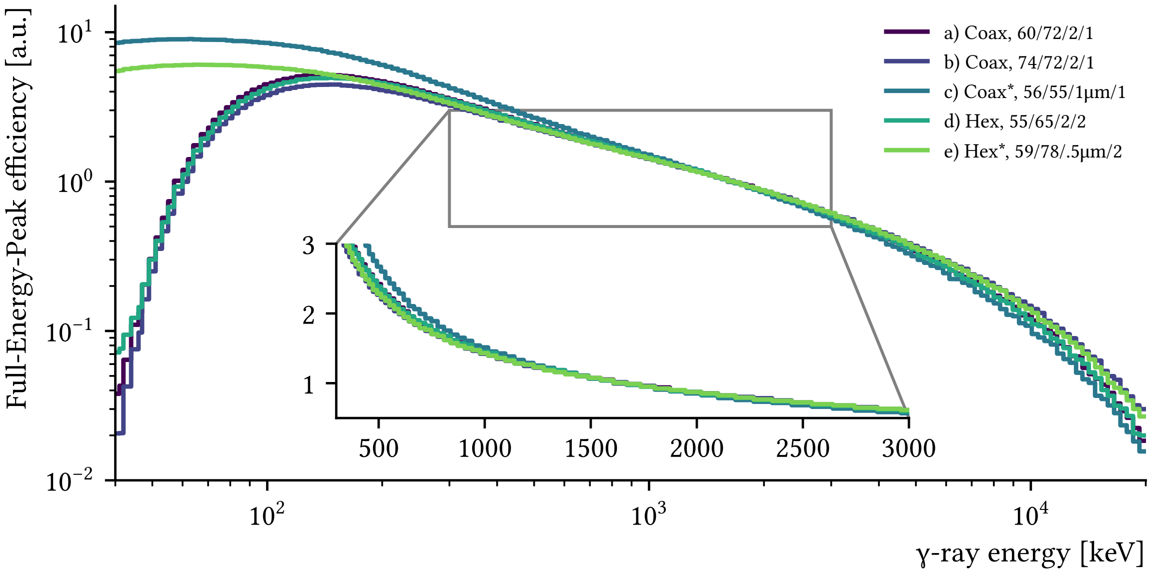

FIGURE 11.3.: Full-Energy-Peak efficiencies, normalized to the mean between 1 MeV to 3 MeV, for different types and implementations of HORUS HPGe detectors. Coaxial and hexagonal shapes (with their diameter/length/dead layer/endcap in mm) were adjusted to match measured efficiency data. Detector parameters marked with * are solely based on manufactured data. Note that for the highlighted energy region, most curves are effectively indistinguishable.

the highest energies, or difficult procurement. Alternatively, given enough calibration points, extrapolation using fitted functions can be used — a process that can produce diverging results for large distances from the highest calibration point and choice of fit function [83], but is reasonably accurate otherwise and low-effort.

Two areas of research have come into focus which require frequent γ-ray detection at energies around 10 MeV and higher: The Pygmy Dipole Resonance and radiative capture reactions for nuclear astrophysics. Both areas of research require precise FEP efficiencies at energies not available with standard sources.

Calibration points in this area are significantly harder to obtain. Decay measurements of pulsed activation in target position, e.g., ^{24}Mg(p,n)^{24}Al [69, 84], emissions from neutron capture reactions, e.g., ^{14}N(n,γ)^{15}N [85], or of prompt γ-ray emission from proton capture, e.g., ^{27}Al(p,γ)^{28}Si [67] can provide calibration data at these high energies. All methods have a very high cost in terms of time taken for preparation and execution, some also subject the detectors to a high current of damaging neutrons. Note that the decay of ^{24}Al is not in the list of recommended nuclides of the Decay Data Evaluation Project (DDEP) [81], i.e. there can be doubts on the accuracy of the existing decay intensity data. The ^{27}Al(p,γ)^{28}Si reaction has many resonances, however only few have been measured extensively, e.g., at $E_p = 992\,\text{keV}$

[86]. This energy is not available at the tandem accelerator in Cologne and thus higher, less well studied energies must be used [67]. In addition, the γ-rays are not emitted isotropically, but are subject to angular correlations, further complicating the efficiency determination.

Simulations can not only interpolate well between the few calibration points these methods deliver, but also reduce the amount of calibration measurements required or even eliminate some of them.

11.4. Simulating coincidences and particle detection

Analysis of events containing data from multiple detectors has become an essential tool in nuclear physics.

For example, γγ-matrices contain information about simultaneous emitted γ-rays and are used investigate the level and decay structure of nuclei. As the direction of the second γ-ray in a γ-ray cascades depends on the direction of the first, sorting data into angular correlation groups can yield information about the underlying structures [66].

Particle detectors can be used in coincidence with HPGe detectors to select events with a specific excitation energy or behavior, which eliminates other unwanted transitions from the spectra [69]. Investigations of the Pygmy-Dipole-Resonance and DSAM base lifetime measurements profit greatly from this procedure [70].

With simulations, coincidence efficiencies can be checked, and the correctness of the analysis software procedure confirmed. They can also be used to develop and test new experimental setups and analysis methods.

CHAPTER 12.

IMPLEMENTATION

G4Horus is a GEANT4 [4] based C++ application. All GEANT4 applications implement and provide three main components: Physics, geometry, and actions.

The project was started with GEANT4 version 10.2 and later upgraded to 10.4.

A predefined physics lists can supply all interactions. It is not necessary to create the physics from smallest components — a fragile process that can sometimes be found in legacy applications. Most physics lists use the same standard electromagnetic physics, which, given the geometrical uncertainties, should be sufficient for this use case. There should be no advantage in using the specialized high precision models for x-rays and γ-rays with energies below 20 keV. G4Horus uses the `Shielding` physics list by default, because it includes a radioactive decay database. Thus, the decay of radioactive sources can be simulated easily.

12.1. SETUP GEOMETRY

As the name suggest, the main experimental setup covered in this project is the high-efficiency γ-ray spectrometer HORUS [67]. It provides 14 mounting points, named `Ge00` to `Ge13`, for detectors arranged in a cubic geometry around the center. In addition, the Cologne Clover Counting Setup used for activation methods is implemented as well [87]. Other setups, like the Cologne Plunger for lifetime measurement, could be supported as well.

The concept of an experimental setup was abstracted into a base class `Setup`, which provides the common detector placement logic via `PlaceDetector`. The individual setups then derive from this base class and provide the Θ and ϕ coordinates of the mounting points and physical structures, if needed.

In the center of HORUS, different target chambers can be installed, for example the target chamber for nuclear astrophysics. Different versions of the SONIC target chamber [69] are available, complete with their particle detector mounting points. Version 3 of SONIC uses CAD based geometry, see Section 12.3 and Figure 12.1.

For each experiment, the user builds the geometry in `DetectorConstruction`, an example is given below. Within a single line, a detector is identified by its id, mounted to a named position, and equipped with an active BGO anti-Compton shield or passive filter materials. Each detector that is supposed to be recording data is then additionally added to a list of active volumes. The whole process of creating all required geometry information is thus reduced to a handful of clearly arranged lines of code, and can be done within minutes:

```
auto horus = new Horus(worldLV);
horus->PlaceDetector("elek",   "Ge00", 17. * cm, {BGO::tSMALLNOSE, "BGO00"});
horus->PlaceDetector("609502", "Ge01",  7. * cm, {{"G4_Cu", 2. * mm}});
horus->PlaceDetector("73954",  "Ge02",  7. * cm);
// ...

auto sonic = new SonicV3(worldLV);
sonic->PlaceDetector("PIPS", "Si00", 45.25 * mm);
sonic->PlaceDetector("PIPS", "Si01", 45.25 * mm);
sonic->PlaceDetector("PIPS", "Si02", 45.25 * mm);
// ...
```

This method requires recompilation on any geometry change. In principle, it is possible to build a messenger system to use Geant4 macros for setup creation at runtime. However, such an additional abstraction layer would take direct control away from the user, preventing him to place other volumes, e.g., a target, in the simulated world. The resulting potential improvement in usability was not deemed worth the control loss, and thus not implemented.

12.2. DETECTOR GEOMETRY

Several types of detectors are implemented in G4Horus, which are derived from a common `Detector` class. This base class provides basic operations to be placeable by the `Setup` class, such that they can be mounted appropriately. `PIPS` particle detectors directly derive from this base class.

For HPGe detectors, several different crystal types exist. A common `HPGe` base class provides implementation of the cylindrical aluminum hull, while the derived `HPGeCoaxial`, `HPGeClover`, and `HPGeHexagonal` classes implement the respective inner structures. Initial parameters for most HPGe detectors were taken from the manufacturer data sheets and gathered in `DetectorLibrary`, a factory class that instantiates the correct detector from its identifier. A total of 22 HPGe parameter sets are available currently.

While all HPGe detectors used here are technically coaxial detectors, the `HPGeCoaxial` implements the unaltered detector shape, a cylinder with a drilled hole from the back. Data sheets provided by the manufacture are reasonably detailed and include diameter, length, volume, and distance to the end cap. Educated guesses had to be made for the dimensions of the hole drilled for the cooling finger.

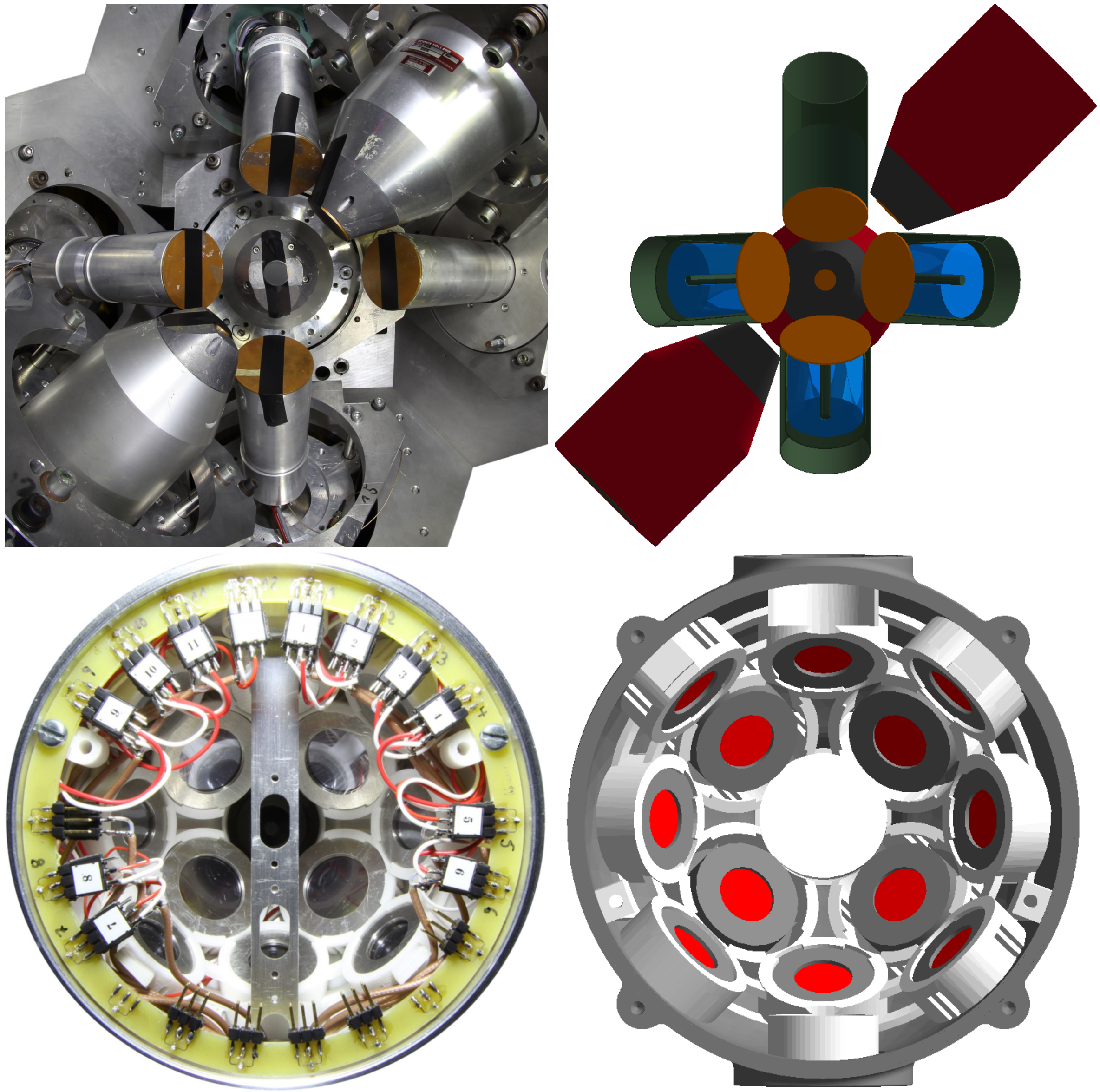

Figure 12.1.: Experimental setups and their implementation in G4Horus. Top: One hemisphere of the high-efficiency γ-ray spectrometer HORUS, equipped with HPGe detectors, BGO anti-Compton shields, and filters. Bottom: The target chamber SONIC V3, equipped with PIPS particle detectors under backward angles. To reproduce the intricate details at minimum effort, chamber and detector frame are imported into Geant4 directly from CAD files, see Section 12.3. (Photos by S. G. Pickstone, 2018. Used with permission [88].)

The crystals implemented by `HPGeHexagonal` are cut to semi-hexagonal conical shapes and encapsulated in hermetically closed aluminum cans of the same shape [89]. This type is used also in EUROBALL [90] and is the predecessor to the six-fold segmented encapsulated MINIBALL [91] detectors. The dimensions that each crystal should have are identical apart from of the length, which can vary and is noted in the data sheets.

The implementation was tested with ^{226}Ra, ^{56}Co, and ^{27}Al(p,γ)^{28}Si calibration data and used for a ^{92}Mo(p,γ)^{93}Tc experiment for nuclear astrophysics [68]. For most detectors, only few changes were necessary to reproduce the absolute FEP efficiency at energies over 500 keV. While it was not necessary to reproduce the shape at low energies for this experiment, an effort was made to bring these in line as well. Some of the encapsulated detectors showed an experimental efficiency up to 30 % lower as simulated over the full energy range.

At the front of the germanium crystal, a dead layer is created due to boron doping. In the manufacturer's datasheets, it is often listed with a thickness of <0.5 µm germanium. This layer is immobile and should not change, even over 25 years of service [92]. Thus, it is technically wrong to treat it as a free parameter. However, it is extremely effective at bringing the low energy part of the efficiency curve in accord with the measured data. With an increase of up to 2 mm in extreme cases, good agreement could be reached for most detectors over the full energy range. A dedicated study conducted by a University in Vietnam used a high-precision x-ray radiography to determine the exact shape of a HPGe crystal, and then varied the dead layer in the simulation. They achieved the best match with a measured ^{152}Eu spectrum for a dead layer thickness of 2.14 mm [75].

On the other hand, the lithium doping of the core can diffuse further into the detector over time, creating further dead layers in the order of few mm. In addition, the crystals are passivated at the end, creating further, not precisely specified, dead layers. Even the best geometric model will hardly be able to model all these inactive zones in the crystals. In addition, damages or imperfections, e.g., distortions of the electric field, are unknown and not detectable by x-ray radiography. These effects can influence the efficiency of the crystal significantly, to the point where the efficiency is no longer fully proportional to the crystal volume. In the initial study of the semi-hexagonal conical encapsulated detectors, efficiency differences of up to 13 % for identical germanium volumes were observed [89, p. 33].

No solution was found that fully satisfies all constraints. Detector parameters and distances were changed to match the measured efficiencies, even if the documented crystal weights were undercut.

BGO shields for active Compton suppression were implemented as measured, with two different types of lead front pieces. Energy deposited in these detectors is converted to a veto signal afterwards, which requires `ntuple` or `soco` output. For determining the HPGe FEP efficiency, it is not required to record veto detector data, and they can be used passively.

The two HPGe Clover detectors of the Cologne Clover Counting Setup with four crystals each were re-implemented with dimensions from prior work [82], without exact knowledge of all dimensions. In a related work, it was found in good agreement for γ-ray energies over 400 keV, with the common deviation of the low energy efficiency peak [93]. A high-precision geometry model of this setup is currently not required, see Section 11.2.

In addition, active anti-Compton BGO-shields exist for these clover detectors but are neither used nor implemented here. For further developments like additional background reduction or new usage concepts, it could be beneficial to implement the entire system, including the mounting rails, the thick lead walls, veto detectors, and the high-precision crystal geometry.

12.3. CAD based geometry

Most modern mechanical structures are created using Computer Aided Design (CAD) software, and then build with Computer Numerical Control (CNC) milling machines or even 3D printers. For this thesis, methods of using the existing geometry descriptions in Geant4 were investigated.

In general, geometry in Geant4 (and other Monte Carlo systems) is implemented using basic shapes like boxes and spheres. These must be created, rotated, intersected, and placed without visual interfaces by writing C++ code. While this is feasible for simple structures, the limit of complexity is reached extremely quickly. More complicated structures, e.g., detector mounts, are simply skipped and not implemented at all. While this is fine for many cases, investigations of, e.g., background sources and propagation, are blocked or meaningless without all physical structures placed completely and accurately. For example, SONIC's detector mount inside the (also partially CNC-build) aluminum chamber was made using selective laser sintering. Its structure is too intricate to build from basic geometrical components using C++ in a timely manner.

Not using data (CAD-files) that already exist *anyway* can also be described as a massive waste of time and effort, independently of the complexity of the models. Even if these do not exist yet, it should be significantly faster and less error prone to create them with any CAD program instead of writing C++ code.

The idea of using these files is not new, but there is no widely adopted solution. There are two main concepts of creating Geant4 compatible volumes: Automatic conversion to basic shapes and operations or usage of tessellated and tetrahedragonal geometric shapes.

These converted shapes can, if necessary, be stored in the intermittent `GDML`-format (Geometry Description Markup Language). Conversion to basic shapes can either be performed with plugins in the CAD program itself, for example in FreeCAD [94] or CATIA [95], or stand-alone by trying to match basic shapes to the compound [96].

Complex shapes can be represented by tessellating their surface in small triangles. Geant4 and `GDML` natively support this type of volume, and some precomputed CAD file types (`stl`, `ply`) can be converted either standalone [97], or by embedding the converter into the GEANT4-based application and performing the conversion at runtime. In addition, instead of just describing the surface, the whole volume can be split into many small volumes with tetrahedral shapes using a Delaunay-based algorithm [98]. The CADMesh software package supports creating tessellated and tetrahedral meshes in GEANT4 [99, 100].

Simple shapes created natively and via CADMesh have been compared for simulation speed and accuracy in G4Horus. γ-rays were shot at a water target in the shape of a box or a sphere, and then detected by HPGe detectors [101]. For a box, the simulation of the tetrahedral shape took 1.5(1) times and the tessellated 1.3(1) times the time of the native shape, while for a sphere, only a small slowdown to 1.1(1) was observed for the tetrahedral version. Spectra deviated about 5 percent from the native for all cases. Version 3 of the SONIC chamber was implement using CADMesh, including the intricate detector mount. While the slowdown compared to a simple shape is massive (x 10), every detail can be represented if required, see Figure 12.1. Further investigations of performance and reliability of this method must be performed.

In the future, it would be advisable to find a solution that is ready for everyday production usage. Due to its massive advantages in development speed, ease of use and flexibility, CAD based simulation geometry should be proposed to be officially supported by the GEANT4 collaboration. To reduce the slowdown of simulations, a hybrid approach might be feasible: Convert structures to simple shapes where possible and use tessellated shapes for the remnants. In a new Monte Carlo code, only tessellated shapes could be supported and used exclusively with GPUs.

12.4. ACTIONS

All actions are initially dispatched by the `ActionInitialization` management class. At runtime, it parses the parameters passed to the executable and selects one out of three output types.

`hist` Histograms are the simplest output type. For each active detector, the deposited energy is collected and filled into the respective histogram, usually at 1 keV per bin. The implementation uses the ROOT-compatible classes from GEANT4.

`ntuple` If coincidence data is required, ROOT ntuples can be used. Here, a table-like structure with a row for each detector is filled with a column for each event. For simple efficiency simulations, this is extraordinarily inefficient as almost all data will be zero. Even with compression, several gigabytes of data be accumulated quickly. This implementation relies on classes delivered with GEANT4 as well.

`soco` SOCO-v2 files are an intermediate format to store event. They are normally produced by SOCO-v2 after calibration and event-building. Its data types, an output management class and the respective actions have been implemented in G4Horus. The format is very efficient for the data produced here, and a full simulation will produce only a few hundred megabytes of data. This simulated data can then be analyses with the same algorithms as real experimental data, just like discussed in Chapter 8.

Primary particles can either be generated by the basic GEANT4 `ParticleGun` to generate single, mono-energetic γ-rays for efficiency determination or by new specialized generators for, e.g., pγ-reactions.

All components are built with multi-threading in mind. The main servers at the Institute for Nuclear Physics in Cologne provide 32 cores, which can be efficiently saturated with the simulations.

The executable can either run in visual mode, where the geometry can be examined in 3D, or batch mode for the actual simulation.

Chapter 13.

Results and applications

13.1. High energy γ-ray efficiency

After the detector implementation described in Section 12.2, the FEP efficiency from 0.5 MeV to 10 MeV could be described satisfactorily. In addition, the SEP and DEP efficiency with and without veto was investigated, which also matched the experimental values, see Figure 13.1. These additional efficiencies were required to determine the total and partial cross sections of the ^{92}Mo(p,γ)^{93}Tc reaction [68].

As this project was released as Open-Source from the beginning, it can easily be used for other experiments [88, 102], including external groups [103, p. 55].

13.2. Coincidence data

Experiments performed with the HORUS spectrometer are typically recorded with the same software used for MINIBALL experiments. The listmode data is precompiled to events using the event builder of SOCO-v2, and then either processes with the SOCO-v2 sorting algorithms converted to ROOT and further processed with ROOT macros. G4Horus supports writing SOCO-v2 compatible event files to investigate γγ, pγ, and other types of experiments. With clean simulated data, analysis routines can be validated, and new methods tested. This follows the same concept is discussed in Section 4.3, however instead of combining everything into a single package like R3BRoot, the individual components are standalone. The data flow is shown in Figure 13.2.

Events simulated for the ^{92}Mo(p,p'γ) reaction were used as a proof-of-concept. Data was sorted into γγ- and pγ- matrices, shown in Figure 13.3.

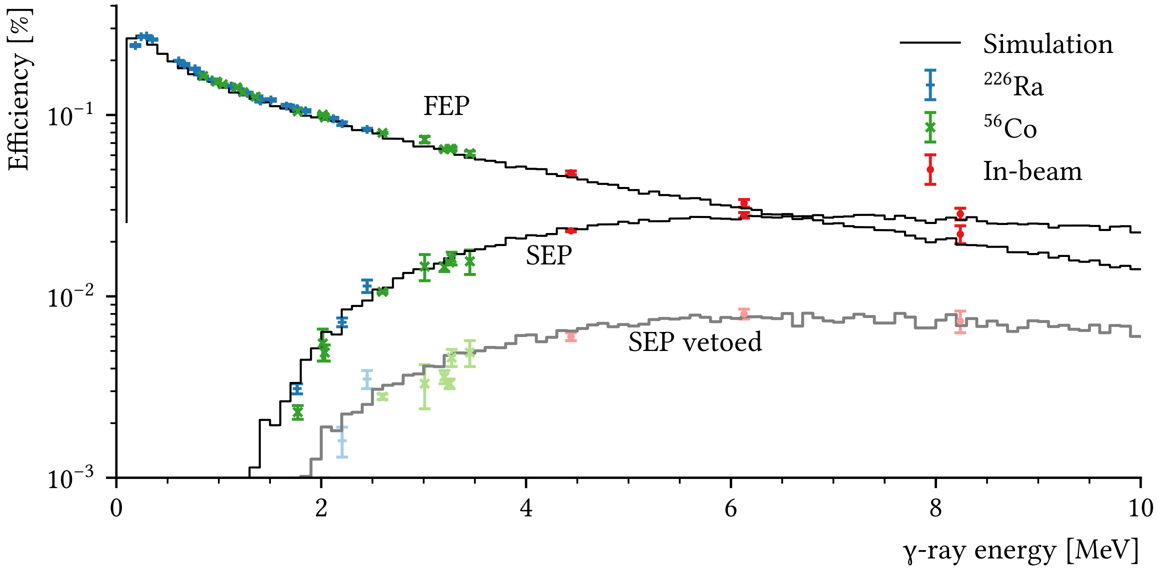

Figure 13.1.: Full energy peak (FEP), single escape peak (SEP) efficiency, and vetoed SEP efficiency for one HORUS anti-Compton shielded HPGe detector. Experimental data has been obtained from standard sources and in-beam reactions (^{27}Al(p,γ)^{28}Si, ^{12}C(p,p'), ^{19}F(p,α)^{16}O, scaled to FEP). Note that from 7 MeV onward, it is more efficient to use the SEP for data analysis if possible, as it carries the same information as the FEP. The BGO-type active anti-Compton shield is also highly effective at detecting the 511 keV annihilation photons, reducing the SEP efficiency by a factor of 3.8(2) for the calibration source, which is well reproduced by the simulation with 3.6(2) for the whole energy range. The efficiencies were used to determine total and partial cross sections for the radiative proton capture on ^{92}Mo [68].

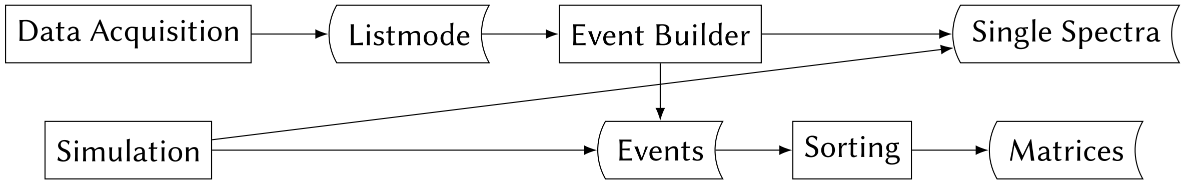

Figure 13.2.: Simplified data flow for experiments with SONIC @ HORUS. Experimental data recorded by the data acquisition is stored in the so-called listmode format, from which SOCO-v2 builds events and extracts non-coincidence spectra. The events can then be further processed, either by the SOCO-v2 sorting suite or other sorting software. G4Horus does not only provide the same type of spectra for efficiency calibration, but also events that can be used to test the sorting algorithms and develop new experiments and methods.

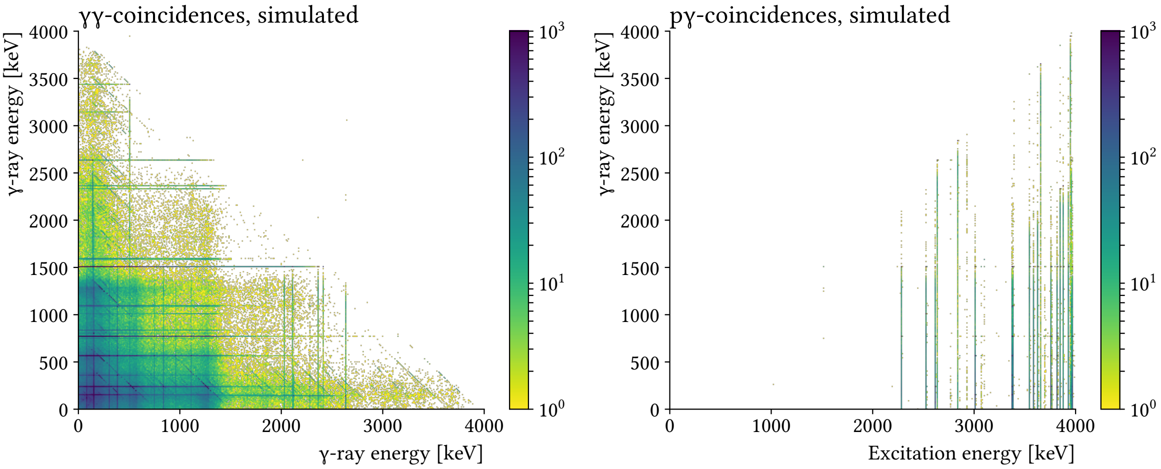

FIGURE 13.3.: Simulated γγ- and pγ-matrices for ^{92}Mo. The level scheme was implemented manually in G4Horus and populated by a custom primary particle generator, which also sends out the scattered proton with the remaining energy. The SOCO events were first converted to ROOT files and then sorted with a simple ROOT script. The matrices can be gated to reveal, e.g., all transition to the ground state, see [69].

13.3. FILTERS AND PASSIVE SHIELDING

Some experiments are count rate limited, that is the beam current must be decreased such that the HPGe detectors and the corresponding data acquisition are not overwhelmed by events. In this case, it could be beneficial to filter out unwanted γ-rays before they even enter the detector. Especially for experiments trying to observe the Pygmy Dipole Resonance and the primary transitions from capture reactions, low-energetic γ-rays are often not desirable.

Copper and lead absorbers can be placed in front of the detector end cap to filter out these unwanted γ-rays. A study was conducted to investigate the impact of different filter thicknesses on the efficiency curve. Here, the total detection (TD) efficiency must be considered, as no signal in the detector should be detected at all - the γ-rays must be completely absorbed in the filter. The properties of the filter should be optimized such that the TD efficiency for $E_\gamma < 500$ keV is reduced significantly while the FEP efficiency for $E_\gamma > 1$ MeV should, at best, not be affected.

Filter thicknesses from 0 mm to 20 mm for solid copper and lead absorbers were placed in front of a HPGe detector with a dead layer of 2 mm. G4Horus automatically pulls the detector back, such that a constant distance from the target to the front of the absorber is kept. Selected efficiency curves divided by the unfiltered efficiency are shown in Figure 13.4.

In experiments conducted at HORUS, 2 mm copper filters are commonly used. The simulations

TABLE 13.1.: Effect of copper and lead filters on the efficiency at specific energies. For each thickness of the absorber d, the efficiency is normalized to the efficiency without absorber: $\kappa = \epsilon(d)/\epsilon(0)$.

Material	d [mm]	κ_{TD}(100 keV) [%]	κ_{TD}(200 keV) [%]	$\overline{\kappa_{FEP}}$([2 MeV, 10 MeV]) [%]
Cu	1	70.0	90.7	95.7(7)
	2	48.6	82.0	91.6(8)
	3	33.7	73.9	87.8(10)
Pb	1	0.2	34.1	93.6(8)
	2	0.0	11.5	87.7(10)
	3	0.0	4.0	82.1(13)

show that these do reduce the FEP efficiency for 100 keV γ-rays by up to 50 % while only reducing the FEP efficiency at high energies by (9(1) %. If higher suppression or suppression at higher energies is required however, simply increasing the thickness will not produce acceptable results, as the γ-rays are not fully absorbed. Here, the TD decouples from the FEP efficiency already at low energies, i.e., Compton scattered γ-rays are detected.

Using lead absorbers with a thickness of 1 mm to 2 mm is significantly more effective at suppressing the TD efficiency with a comparable impact at higher energies (7(1) % to 13(1) %), see Table 13.1.

In addition, all currently unshielded detectors should be wrapped in 1 mm to 2 mm of lead, to prevent stray γ-rays from entering the detector from the side. A combination of copper and might also be viable for added structural integrity.

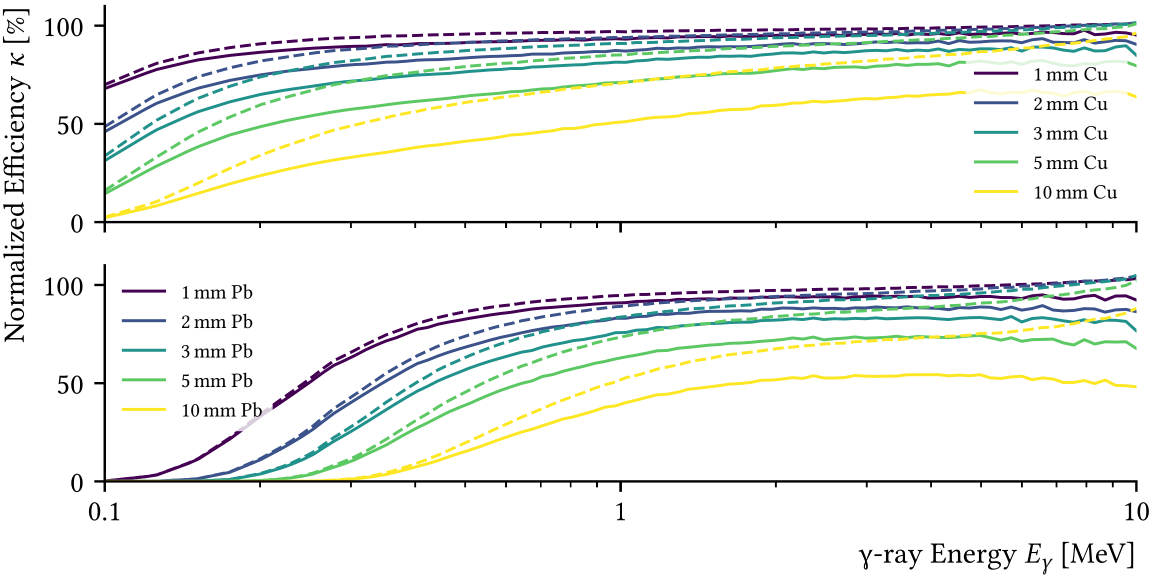

Figure 13.4.: Effect of copper and lead filters on the efficiency at specific energies. For each thickness of the absorber d, the full energy peak efficiency (solid) and total detection efficiency (dashed) is normalized to the efficiency without absorber: $\kappa = \epsilon(d)/\epsilon(0)$.

CHAPTER 14.

SUMMARY AND OUTLOOK

G4Horus simulates the full-energy-peak efficiency of experiments performed at HORUS. With minimal knowledge and effort, results can be produced quickly due to the included detector geometries and mounting procedure. In addition, the simulation of single- and double-escape-peak efficiencies as well as $\gamma\gamma$ and at particle-γ coincidences are available.

In the future, the existing base can be extended to study specific experiments, an overview over the development is shown in Figure 14.1. One such extension could be lifetime measurements with pγ-coincidence DSAM (doppler shift attenuation method). Once the accuracy and applicability of the stopping procedure and in-flight decay in GEANT4 has been verified, the response of the setup to different stoppers, beam energies and level lifetimes could be analyzed and optimized. Transfer experiments with particle identification using the ΔE-E version of SONIC could be studied beforehand to investigate the theoretical coincidence efficiency and test the analysis algorithms.

The implementation of the HPGe detectors is still the main weak point. All detectors, especially newly acquired, should be characterized meticulously by measuring and simulating:

- Standard calibration sources, like ^{133}Ba, ^{152}Eu, ^{226}Ra, ^{60}Co and ^{56}Co.
- Highly collimated sources and different positions around the detector, including from behind.
- Short lived sources created by activation. Recommendation: ^{66}Ga, which can be created locally at the FN-Tandem accelerator via a (p,n) reaction on ^{66}Zn, which has a natural abundance of $\approx 27\,\%$ and is an unproblematic material to work with.
- Decay of ^{24}Al, created by activating ^{24}Mg using a pulsed beam. The β-slider [64] could reduce the exposure of the HPGe crystals to damaging neutrons. ^{24}Al should also be recommended for admission by the DDEP.

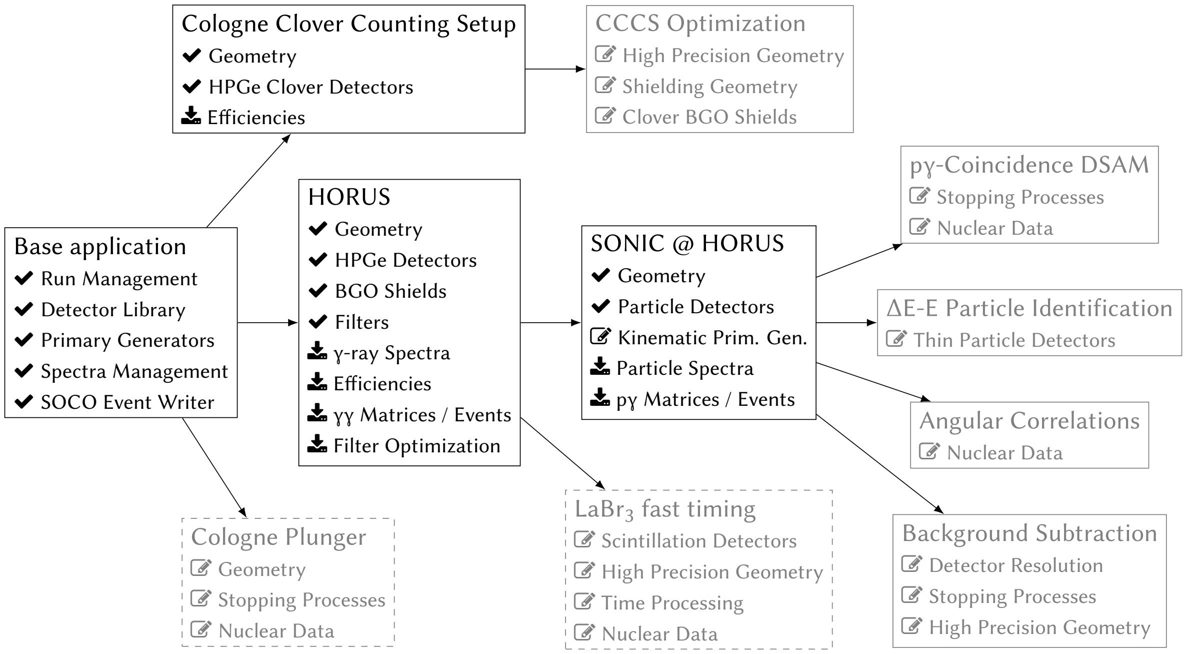

FIGURE 14.1.: G4Horus development tree. Experimental use cases with their ✓ implemented and ✎ possible components and the available ⬇ output. Researching new components can unlock support for several types of experiments in the future.

PART III.

APPENDIX

Appendix A.

NeuLAND

A.1. Top 10 reaction products

Table A.1.: Top 10 reactions for incoming neutrons with an kinetic energy of 600 MeV in 30 NeuLAND double planes using the `QGSP_INCLXX_HP` and `QGSP_BERT` physics lists, excluding γ-rays. Note that for all reactions listed here, at least one neutron is emitted and most reactions also create protons or involve the destruction of carbon atoms. Elastic scattering on protons only contributes 1.4 % or 1.7 %, respectively.

`QGSP_INCLXX_HP`			`QGSP_BERT`		
Rank	Reaction products	[%]	Rank	Reaction products	[%]
1	n, n, n, p, p, ^{4}He, ^{4}He	6.6	1	n, p, ^{11}B	9.7
2	n, p, ^{11}B	5.7	2	n, n, ^{11}C	7.5
3	n, n, p, d, ^{4}He, ^{4}He	5.2	3	n, n, n, p, p, ^{4}He, ^{4}He	5.4
4	n, n, ^{11}C	4.4	4	n, n, p, ^{10}B	4.1
5	n, n, p, ^{10}B	2.4	5	n, n, n, p, p, ^{8}Be	3.6
6	n, p, ^{4}He, ^{7}Li	2.4	6	n, p, ^{11}C, π^-	2.3
7	n, n, ^{4}He, ^{7}Be	2.0	7	n, n, p, d, ^{4}He, ^{4}He	2.2
8	n, n, p, ^{4}He, ^{6}Li	1.7	8	**n, p**	1.7
9	n, n, p, p, d, t, ^{4}He	1.6	9	n, ^{12}C	1.7
10	**n, p**	1.4	10	n, n, p, d ^{8}Be	1.7
8467 individual ejectile sets		99.2	4560 individual ejectile sets		98.9

A.2. NEUTRON ENERGY FROM ELASTIC SCATTERING

A neutron is scattering on a proton:

$$\mathbf{P}_N + \mathbf{P}_P = \mathbf{P}'_N + \mathbf{P}'_P \tag{A.1}$$

$$(\mathbf{P}_N + \mathbf{P}_P)^2 = (\mathbf{P}'_N + \mathbf{P}'_P)^2 \tag{A.2}$$

$$\mathbf{P}_N^2 + 2\mathbf{P}_N \cdot \mathbf{P}_P + \mathbf{P}_P^2 = \mathbf{P}'^2_N + 2\mathbf{P}'_N \cdot \mathbf{P}'_P + \mathbf{P}'^2_P \tag{A.3}$$

The scattering is elastic, i.e., $\mathbf{P}^2 = m_0^2 c^4 = \mathbf{P}'^2$:

$$\mathbf{P}_N \cdot \mathbf{P}_P = \mathbf{P}'_N \cdot \mathbf{P}'_P \tag{A.4}$$

Eliminating the four-momentum of the scattered neutron: $\mathbf{P}'_N = \mathbf{P}_N + \mathbf{P}_P - \mathbf{P}'_P$

$$\mathbf{P}_N \cdot \mathbf{P}_P = (\mathbf{P}_N + \mathbf{P}_P - \mathbf{P}'_P) \cdot \mathbf{P}'_P \tag{A.5}$$

In the laboratory system, the proton is at rest before the collision: $\mathbf{P}_P = (Kc^{-1}, \vec{0}) = (m_0 c, \vec{0})$.

$$(E_N c^{-1}, \vec{p}_N) \cdot (m_0 c, \vec{0}) = \mathbf{P}_N \cdot \mathbf{P}'_P + \mathbf{P}_P \cdot \mathbf{P}'_P - \mathbf{P}'^2_P \tag{A.6}$$

$$E_N m_0 = E_N E'_P c^{-2} - \vec{p}_N \cdot \vec{p}'_P + E'_P m_0 - m_0^2 c^2 \tag{A.7}$$

$$= E_N E'_P c^{-2} - p_N p'_P \cos\theta_{NP'} + E'_P m_0 - m_0^2 c^2 \tag{A.8}$$

Where $\theta_{NP'}$ is the angle between the direction of the incoming neutron and the scattered proton. With $p = \sqrt{E^2 c^{-2} - m_0^2 c^2}$ and $m_N \approx m_P$:

$$\sqrt{E_N^2 c^{-2} - m_0^2 c^2}\sqrt{E'^2_P c^{-2} - m_0^2 c^2}\cos\theta_{NP'} = (E_N c^{-1} + m_0 c)(E'_P c^{-1} - m_0 c) \tag{A.9}$$

$$(E_N c^{-1} - m_0 c)(E'_P c^{-1} + m_0 c)\cos^2\theta_{NP'} = (E_N c^{-1} + m_0 c)(E'_P c^{-1} - m_0 c) \tag{A.10}$$

$$\frac{E'_P + m_0 c^2}{E'_P - m_0 c^2}\cos^2\theta_{NP'} = \frac{E_N + m_0 c^2}{E_N - m_0 c^2} \tag{A.11}$$

Solving for E_N using that $a = \frac{x+b}{x-b} \Rightarrow x = \frac{a+1}{a-1}b$:

$$E_N(E'_P, \theta_{NP'}) = \frac{a+1}{a-1} m_0 c^2 \quad \text{with} \quad a = \frac{E'_P + m_0 c^2}{E'_P - m_0 c^2}\cos^2\theta_{NP'} \tag{A.12}$$

One can obtain a formula that only depends on the kinetic energy $K = E - m_0 c^2$ of the scattered proton and the angle $\theta_{NP'}$

$$K_N(K'_P, \theta_{NP'}) = \left(\frac{a+1}{a-1} - 1\right) m_0 c^2 \quad \text{with} \quad a = \frac{K'_P + 2m_0 c^2}{K'_P}\cos^2\theta_{NP'} \tag{A.13}$$

$$K_N(K'_P, \theta_{NP'}) = \frac{2m_0 c^2 K'_P}{2m_0 c^2 \cos^2\theta_{NP'} - K'_P \sin^2\theta_{NP'}} \tag{A.14}$$

A.3. Protobuf data structure for NeuLAND events

```
syntax = "proto2";
package Neuland;

message Digi {
	optional int32 id = 1;
	optional float tl = 2;
	optional float tr = 3;
	optional float e = 4;
}

message Pixel {
	optional int32 x = 1;
	optional int32 y = 2;
	optional int32 z = 3;
	optional float e = 4;
	optional float t = 5;
}

message Neutron {
	optional int32 x = 1;
	optional int32 y = 2;
	optional int32 z = 3;
	optional float t = 4;
}

message Event {
	optional int32 runID = 1;
	optional int32 eventID = 2;
	repeated Pixel pixels = 3;
	repeated Neutron neutrons = 4;
	repeated Digi digis = 5;
}
```

Listing 3.: Protobuf data structure for NeuLAND events. An event contains its run and event number, and flexible-width storage for three data types: Digis, which are the hits in NeuLAND, identified by scintillator id, with the trigger time of the left and right scintillator, and the energy. Pixels are similar to Digis, but the position is converted to indices in a 50x50x60 grid. Neutrons, which are the primary neutron interaction points in NeuLAND with their grid-position, energy, and time information; the size of this storage is the multiplicity to determine.

Appendix B.

G4Horus

Table B.1.: Recommended radio nuclides for detector calibration with γ-ray emissions over 3 MeV by the Decay Data Evaluation Project (DDEP) [81] with the number of γ-ray lines usable for calibration purposes, half-life, highest γ-ray energy and the respective intensity. Note that only ^{266}Ra has a half-life of over one year, and is only listed due to the emissions of its daughter ^{214}Bi, with which it is expected to be in equilibrium. ^{56}Co stands out with its storable half-live and high energy transitions. A (p,n) activation of an enriched ^{66}Zn target creates ^{66}Ga, which can then be moved to the detectors in need of calibration. The decay of ^{24}Al is not (yet) recommended by the DDEP, data taken from ENSDF [80]. It can be produced in place with a (p,n) reaction on ^{24}Mg [69].

Nuclide	Cal. Points	Half-Life [s]	$E_{\gamma,\mathrm{max}}$ [keV]	$I_{\gamma,\mathrm{max}}$ [%]
Zn-63	66	$2.300(6) \times 10^{3}$	3101.3(4)	0.0007(2)
Ni-57	23	$1.293(20) \times 10^{5}$	3177.27(5)	0.015(4)
Bi-214	214	$1.188(6) \times 10^{3}$	3183.57(40)	0.0011(5)
Ra-226	257	$5.049(22) \times 10^{10}$	3183.57(40)	0.0011(5)
Y-88	7	$9.2128(43) \times 10^{6}$	3218.426(22)	0.0071(20)
Sc-44	5	$1.429(14) \times 10^{4}$	3301.35(6)	0.0017(2)
La-140	38	$1.450\,29(18) \times 10^{5}$	3319.52(24)	0.0039(3)
Mn-56	10	$9.2836(17) \times 10^{3}$	3369.84(4)	0.17(1)
Rh-106	87	$3.01(3) \times 10^{1}$	3401.8(9)	0.000 012 5(19)
Co-56	46	$6.6732(22) \times 10^{6}$	3611.8(8)	0.0084(4)
Rb-82	45	$7.591(27) \times 10^{1}$	3956(1)	0.000 090(15)
Tc-94m	59	$3.11(6) \times 10^{3}$	4136.2(3)	0.007(1)
Na-24	6	$5.3849(7) \times 10^{4}$	4237.84(3)	0.000 84(10)
Br-76	165	$5.80(7) \times 10^{4}$	4605.7(7)	0.015(8)
Ga-66	145	$3.416(25) \times 10^{4}$	5005.6(3)	0.001 24(18)
Al-24	44	2.053(4)	9943.5(15)	0.027(6)

List of Figures

List of Tables

BIBLIOGRAPHY

[1] H. Geiger and E. Marsden, “On a Diffuse Reflection of the α-Particles,” Proc. R. Soc. Lond. A **82**, 495 (1909) DOI: `10.1098/rspa.1909.0054`.

[2] E. Rutherford, “LXXIX. The scattering of α and β particles by matter and the structure of the atom,” Lond. Edinb. Dubl. Phil. Mag. **21**, 669 (1911) DOI: `10.1080/14786440508637080`.

[3] F. James, “Monte Carlo theory and practice,” Rep. Prog. Phys. **43**, 1145 (1980) DOI: `10.1088/0034-4885/43/9/002`.

[4] S. Agostinelli et al., “Geant4—a simulation toolkit,” Nucl. Instrum. Methods Phys. Res., Sect. A **506**, 250 (2003) DOI: `10.1016/S0168-9002(03)01368-8`.

[5] P. Giubellino, “Status of the FAIR Project,” DPG Spring Meeting, Muenster, Mar. 28, 2017.

[6] *Technical Report for the Design, Construction and Commissioning of NeuLAND*, Available at `https://edms.cern.ch/document/1865739/1`, Accessed: 2018-08-01 (2011).

[7] *FAIR CDR - An International Accelerator Facility for Beams of Ions and Antiprotons*, Available at `https://fair-center.de/fileadmin/fair/publications_FAIR/FAIR_CDR.pdf`, Accessed: 2018-08-01 (2001).

[8] H. Geissel et al., “The Super-FRS project at GSI,” Nucl. Instrum. Methods Phys. Res., Sect. B **204**, 71 (2003) DOI: `10.1016/S0168-583X(02)01893-1`.

[9] P. Spiller and G. Franchetti, “The FAIR accelerator project at GSI,” Nucl. Instrum. Methods Phys. Res., Sect. A **561**, 305 (2006) DOI: `10.1016/j.nima.2006.01.043`.

[10] A. Herlert, “NUSTAR - The teenage years: Towards operation at FAIR,” Hyperfine Interact. **238**, 35 (2017) DOI: `10.1007/s10751-017-1411-0`.

[11] A. Herlert, “The NUSTAR program at FAIR,” EPJ Web Conf. **71**, 00064 (2014) DOI: `10.1051/epjconf/20147100064`.

[12] R. Krücken, “The NuSTAR facilty at FAIR,” J. Phys. G Nucl. Part. Phys. **31**, S1807 (2005) DOI: `10.1088/0954-3899/31/10/077`.

[13] M. Destefanis, “The PANDA experiment at FAIR,” Nucl. Phys. B - Proc. Suppl. **245**, 199 (2013) DOI: `10.1016/j.nuclphysbps.2013.10.040`.

[14] W. Erni et al., “Physics Performance Report for PANDA: Strong Interaction Studies with Antiprotons,” ArXiv e-prints **0903.3905** (2009).

[15] T. Stöhlker et al., “APPA at FAIR: From fundamental to applied research,” Nucl. Instrum. Methods Phys. Res., Sect. B **365**, 680 (2015) DOI: `10.1016/j.nimb.2015.07.077`.

[16] V. Friese, “The CBM experiment at GSI/FAIR,” Nucl. Phys. A **774**, 377 (2006) DOI: `10.1016/j.nuclphysa.2006.06.018`.

[17] B. Friman et al., eds., *The CBM Physics Book*, Vol. 814, Lecture Notes in Physics (Springer Berlin Heidelberg, 2011), ISBN: 9783642132926, DOI: `10.1007/978-3-642-13293-3`.

[18] T. Blaich et al., "A large area detector for high-energy neutrons," Nucl. Inst. Methods Phys. Res. A **314**, 136 (1992) DOI: `10.1016/0168-9002(92)90507-Z`.

[19] D. M. Rossi et al., "Coulomb excitation of exotic nuclei at the R^{3}B-LAND setup," J. Phys. Conf. Ser. **420**, 012072 (2013) DOI: `10.1088/1742-6596/420/1/012072`.

[20] D. Cortina-Gil et al., "CALIFA, a Dedicated Calorimeter for the R^{3}B/FAIR," Nucl. Data Sheets **120**, 99 (2014) DOI: `10.1016/j.nds.2014.07.017`.

[21] D. Körper, private communication, 2018.

[22] T. Baumann, A. Spyrou, and M. Thoennessen, "Nuclear structure experiments along the neutron drip line," Reports Prog. Phys. **75**, 036301 (2012) DOI: `10.1088/0034-4885/75/3/036301`.

[23] K. Boretzky, private communication, 2018.

[24] K. Boretzky et al., "Construction and Test of a Large NeuLAND Prototype Array," GSI Sci. Rep. 2012, 190 (2013) DOI: `10.15120/GR-2013-1`.

[25] K. Boretzky et al., "NeuLAND - from prototypes to double-planes," GSI Sci. Rep. 2013, 346 (2014) DOI: `10.15120/GR-2014-1`.

[26] J. L. Rodríguez-Sánchez et al., "Dissipative effects in fission by using complete kinematics measurements," GSI Sci. Rep. 2015, 118 (2016) DOI: `10.15120/GR-2016-1`.

[27] Y. Yano, "The RIKEN RI Beam Factory Project: A status report," Nucl. Instrum. Methods Phys. Res., Sect. B **261**, 1009 (2007) DOI: `10.1016/j.nimb.2007.04.174`.

[28] T. Kubo, "In-flight RI beam separator BigRIPS at RIKEN and elsewhere in Japan," Nucl. Instrum. Methods Phys. Res., Sect. B **204**, 97 (2003) DOI: `10.1016/S0168-583X(02)01896-7`.

[29] Y. Shimizu et al., "SAMURAI project at RIBF," in J. phys. conf. ser. Vol. 312, SECTION 5 (Sept. 2011), p. 052022, DOI: `10.1088/1742-6596/312/5/052022`.

[30] J. Kahlbow et al., "Experimental campaign using the NeuLAND demonstrator at SAMURAI," GSI Sci. Rep. 2017, in press.

[31] K. Boretzky et al., "NeuLAND - from double-planes to the demonstrator," GSI Sci. Rep. 2014, 200 (2015) DOI: `10.15120/GR-2015-1`.

[32] *Data-analysis software*, `https://www.gsi.de/en/work/research/nustarenna/nustarenna_divisions/nuclear_reactions/activities/r3b_project_group/software/analysis_software.htm`, Accessed: 2018-05-01.

[33] R. Plag, *The unofficial guide to the unofficial version of land02*, `http://web-docs.gsi.de/~rplag/land02/`, Accessed: 2018-05-01.

[34] V. Wagner, "Multi-Neutronen-Detektion beim R^{3}B-Experiment an FAIR mit verbesserter Detektorantwort," Bachelorthesis (TU Darmstadt, 2014).

[35] V. Wagner, "Automatisierte Synchronisierung und Energiekalibrierung des NeuLAND-Detektors für das R^{3}B-Expertiment an der Facility for Antiproton and Ion Research FAIR," Masterthesis (TU Darmstadt, 2016).

[36] C. A. Douma et al., "Design studies for the NeuLAND VETO detector," J. Phys. Conf. Ser. **1024**, 012027 (2018) DOI: `10.1088/1742-6596/1024/1/012027`.

[37] H. T. Johansson et al., "GGLAND — command line simulations," GSI Sci. Rep. 2013, 154 (2014) DOI: `10.15120/GR-2014-1`.

[38] R. Tanaka, *Smsimulator*, `http://be.nucl.ap.titech.ac.jp/~nebula/simulator.php`, Accessed: 2018-06-01.

[39] M. Al-Turany et al., "The FairRoot framework," J. Phys. Conf. Ser. **396**, 022001 (2012) DOI: `10.1088/1742-6596/396/2/022001`.

[40] A. Rybalchenko and M. Al-Turany, "FairMQ status," GSI Sci. Rep. 2016, 365 (2017) DOI: `10.15120/GR-2017-1`.

[41] F. E. James, "Monte Carlo phase space," in (CERN, 1968), 41 p.

[42] W. Luo et al., "Implementation of the n-body Monte-Carlo event generator into the Geant4 toolkit for photonuclear studies," Nucl. Instrum. Methods Phys. Res., Sect. A **849**, 49 (2017) DOI: `10.1016/j.nima.2017.01.010`.

[43] J. F. Ziegler, "The background in detectors caused by sea level cosmic rays," Nucl. Instruments Methods **191**, 419 (1981) DOI: `10.1016/0029-554X(81)91039-9`.

[44] S. Haino et al., "Measurements of primary and atmospheric cosmic-ray spectra with the BESS-TeV spectrometer," Phys. Lett. B **594**, 35 (2004) DOI: `10.1016/J.PHYSLETB.2004.05.019`.

[45] M. A. Szelezniak et al., *Charged Particle Detection*, 2007.

[46] M. Heil, private communication, 2018.

[47] Y. Kondo, private communication, 2018.

[48] J. Kahlbow, private communication, 2018.

[49] T. N. Taddeucci et al., "Zero-degree cross sections for the ^{7}Li(p,n)^{7}Be (g.s.+0.43 MeV) reaction in the energy range 80–795 MeV," Phys. Rev. C **41**, 2548 (1990) DOI: `10.1103/PhysRevC.41.2548`.

[50] J. Kahlbow et al., "NeuLAND demonstrator at SAMURAI : commissioning and efficiency studies," RIKEN Accel. Prog. Rep **49**, 17 (2016).

[51] J. Kahlbow et al., "Efficiency study of the NeuLAND demonstrator," GSI Sci. Rep. 2016, 211 (2017) DOI: `10.15120/GR-2017-1`.

[52] E. Mendoza et al., "New evaluated neutron cross section libraries for the GEANT4 code," 2012 (2012).

[53] A. Adinetz et al., "Triplet Finder: On the way to triggerless online reconstruction with GPUs for the PANDA experiment," J. Comput. Sci. **10**, 317 (2015) DOI: `10.1016/j.jocs.2015.03.010`.

[54] L. Bianchi et al., "Online tracking algorithms on GPUs for the PANDA experiment at FAIR," in J. phys. conf. ser. Vol. 664, 8 (Dec. 2015), p. 082006, DOI: `10.1088/1742-6596/664/8/082006`.

[55] W. S. McCulloch and W. Pitts, "A logical calculus of the ideas immanent in nervous activity," Bull. Math. Biophys. **5**, 115 (1943) DOI: `10.1007/BF02478259`.

[56] D. Hebb, *The Organization of Behavior: A Neuropsychological Theory* (Taylor & Francis, 2002), ISBN: 9781410612403.

[57] D. Barber, *Bayesian Reasoning and Machine Learning* (Cambridge University Press, 2012), ISBN: 9780521518147.

[58] E. Alpaydin, *Machine Learning: The New AI* (The MIT Press, 2016), ISBN: 9780262529518.

[59] S. Shalev-Shwartz and S. Ben-David, *Understanding Machine Learning: From Theory to Algorithms* (Cambridge University Press, 2014), ISBN: 9781107057135.

[60] D. Silver et al., "Mastering the game of Go without human knowledge," Nature **550**, 354 (2017) DOI: `10.1038/nature24270`.

[61] M. Polleryd, "Neutron Reconstruction using Neural Networks," Masterthesis (Chalmers University of Technology, 2017).

[62] *Protocol buffers*, `https://developers.google.com/protocol-buffers/`, Accessed: 2018-08-01.

[63] H. R. Kerzner, *Project management: a systems approach to planning, scheduling, and controlling* (Wiley, 2009), isbn: 9780470278703.

[64] A. Linnemann, “Das HORUS-Würfelspektrometer und Multiphononanregungen in ^{106}Cd,” Dissertation (University of Cologne, 2005).

[65] S. Pascu et al., “Detailed spectroscopy of quadrupole and octupole states in ^{168}Yb,” Phys. Rev. C - Nucl. Phys. **91**, 034321 (2015) doi: `10.1103/PhysRevC.91.034321`.

[66] C. Fransen et al., “Low-spin γ-ray spectroscopy of the (critical-point?) nucleus ^{122}Ba,” Phys. Rev. C - Nucl. Phys. **69**, 6 (2004) doi: `10.1103/PhysRevC.69.014313`.

[67] L. Netterdon et al., “The γ-ray spectrometer HORUS and its applications for nuclear astrophysics,” Nucl. Instrum. Methods Phys. Res., Sect. A **754**, 94 (2014) doi: `10.1016/j.nima.2014.04.025`.

[68] J. Mayer et al., “Partial cross sections of the ^{92}Mo(p,γ) reaction and the γ strength in ^{93}Tc,” Phys. Rev. C **93**, 045809 (2016) doi: `10.1103/PhysRevC.93.045809`.

[69] S. G. Pickstone et al., “Combining γ-ray and particle spectroscopy with SONIC@HORUS,” Nucl. Instrum. Methods Phys. Res., Sect. A **875**, 104 (2017) doi: `10.1016/J.NIMA.2017.09.016`.

[70] A. Hennig et al., “Lifetime measurement of excited low-spin states via the (p,p’γ) reaction,” Nucl. Instrum. Methods Phys. Res., Sect. A **794**, 171 (2015) doi: `10.1016/j.nima.2015.05.024`.

[71] S. G. Pickstone et al., “Study of the Pygmy Dipole Resonance in (p,p’γ) and (d,pγ) experiments with SONIC@HORUS,” in Epj web conf. Vol. 93 (2015), p. 01053, isbn: 9782759817948, doi: `10.1051/epjconf/20159301053`.

[72] J. C. Hardy et al., “Precise efficiency calibration of an HPGe detector: source measurements and Monte Carlo calculations with sub-percent precision,” Appl. Radiat. Isot. **56**, 65 (2002) doi: `10.1016/S0969-8043(01)00168-3`.

[73] P.-A. Söderström et al., “Interaction position resolution simulations and in-beam measurements of the AGATA HPGe detectors,” Nucl. Instrum. Methods Phys. Res., Sect. A **638**, 96 (2011) doi: `10.1016/J.NIMA.2011.02.089`.

[74] S. Baccouche et al., “Application of the Monte Carlo method for the efficiency calibration of CsI and NaI detectors for γ-ray measurements from terrestrial samples,” Appl. Radiat. Isot. **70**, 227 (2012) doi: `10.1016/J.APRADISO.2011.07.008`.

[75] H. D. Chuong et al., “Estimating thickness of the inner dead-layer of n-type HPGe detector,” Appl. Radiat. Isot. **116**, 174 (2016) doi: `10.1016/J.APRADISO.2016.08.010`.

[76] G. Giubrone et al., “Calculation of Coincidence Summing Correction Factors for an HPGe detector using GEANT4,” J. Environ. Radioact. **158-159**, 114 (2016) doi: `10.1016/J.JENVRAD.2016.04.008`.

[77] U. Rizwan et al., “A method for establishing absolute full-energy peak efficiency and its confidence interval for HPGe detectors,” Nucl. Instrum. Methods Phys. Res., Sect. A **802**, 102 (2015) doi: `10.1016/J.NIMA.2015.08.071`.

[78] R. Breier, M. Laubenstein, and P. Povinec, “Monte Carlo simulation of background characteristics of a HPGe detector operating underground in the Gran Sasso National Laboratory,” Appl. Radiat. Isot. **126**, 188 (2017) doi: `10.1016/J.APRADISO.2016.12.039`.

[79] A. Sauerwein et al., “Determination of ^{141}Pr(α,n)^{144}Pm cross sections at energies of relevance for the astrophysical p process using the γγ coincidence method,” Phys. Rev. C **84**, 045808 (2011) doi: `10.1103/PhysRevC.84.045808`.

[80] *Archived ensdf files*, `https://www.nndc.bnl.gov/ensarchivals/`, Accessed: 2018-05-01.

[81] A. Pluquet, *Recommended data by the Decay Data Evaluation Project working group*, 2013.

[82] A. Hennig, "Aufbau und Test eines Aktivierungsmessplatzes für Experimente der Nuklearen Astrophysik," Diplomathesis (University of Cologne, 2011).

[83] E. Hoemann, "Automatisierte Energie- und Effizienzkalibrierung von HPGe Detektoren," Bachelorthesis (University of Cologne, 2016).

[84] M. Wilhelm et al., "The response of the Euroball Cluster detector to γ-radiation up to 10 MeV," Nucl. Instrum. Methods Phys. Res., Sect. A **381**, 462 (1996) doi: `10.1016/S0168-9002(96)00793-0`.

[85] G. L. Molnár, Z. Révay, and T. Belgya, "Wide energy range efficiency calibration method for Ge detectors," Nucl. Instrum. Methods Phys. Res., Sect. A **489**, 140 (2002) doi: `10.1016/S0168-9002(02)00902-6`.

[86] H. L. Scott and T. Lusby, "Intensity measurements of the γ-ray decay of ^{28}Si via the ^{27}Al(p,γ)^{28}Si Ep = 992 keV resonance," Nucl. Instruments Methods **131**, 517 (1975) doi: `10.1016/0029-554X(75)90443-7`.

[87] P. Scholz et al., "Measurement of the ^{187}Re(α,n)^{190}Ir reaction cross section at sub-Coulomb energies using the Cologne Clover Counting Setup," Phys. Rev. C - Nucl. Phys. **90**, 065807 (2014) doi: `10.1103/PhysRevC.90.065807`.

[88] S. G. Pickstone, "Upgrading the particle spectrometer SONIC and (p,p'γ) coincidence measurements on Mo-92, Mo-94, and Ni-60," Dissertation (University of Cologne, 2018), isbn: 9783843937740.

[89] H. G. Thomas, "Entwicklung eines Germanium-CLUSTER-Detectors für das Gamma-Spektrometer EUROBALL," Dissertation (University of Cologne, 1995).

[90] J. Simpson, "The Euroball Spectrometer," Zeitschrift für Phys. A Hadron. Nucl. **358**, 139 (1997) doi: `10.1007/s002180050290`.

[91] N. Warr et al., "The Miniball spectrometer," Eur. Phys. J. A **49**, 40 (2013) doi: `10.1140/epja/i2013-13040-9`.

[92] J. Eberth, private communication, 2018.

[93] M. Körschgen, "Test einer Untergrundabschirmung und Untersuchung von Summeneffekten an einem Cloverauszählaufbau," Bachelorthesis (University of Cologne, 2017).

[94] E. Delage, *Cad-gdml on freecad*, `http://cad-gdml.in2p3.fr/`, Accessed: 2018-06-01.

[95] S. Belogurov et al., "CATIA-GDML geometry builder," J. Phys. Conf. Ser. **331**, 032035 (2011) doi: `10.1088/1742-6596/331/3/032035`.

[96] T. Stockmanns, "STEP-to-ROOT – from CAD to Monte Carlo Simulation," J. Phys. Conf. Ser. **396**, 022050 (2012) doi: `10.1088/1742-6596/396/2/022050`.

[97] A. Tykhonov, *Cad-to-geant4-converter*, `https://github.com/tihonav/cad-to-geant4-converter`, Accessed: 2018-06-01.

[98] H. Si and Hang, "TetGen, a Delaunay-Based Quality Tetrahedral Mesh Generator," ACM Trans. Math. Softw. **41**, 1 (2015) doi: `10.1145/2629697`.

[99] C. M. Poole et al., "Fast tessellated solid navigation in GEANT4," IEEE Trans. Nucl. Sci. **59**, 1695 (2012) doi: `10.1109/TNS.2012.2197415`.

[100] C. M. Poole et al., "A CAD interface for GEANT4," Australas. Phys. Eng. Sci. Med. **35**, 329 (2012) doi: `10.1007/s13246-012-0159-8`.

[101] E. Hoemann, private communication, 2018.

[102] P. Scholz, "Exploring statistical properties of nuclei for explosive stellar nucleosynthesis," Dissertation (University of Cologne, 2018), isbn: 9783843937849.

[103] P. Erbacher, "Nucleosynthesis of nuclei near the N = 50 neutron shell closure," Dissertation (Johann Wolfgang Goethe-Universität, 2018).

[104] J. Mayer et al., “Neutron reconstruction with NeuLAND in FAIR Phase 0,” GSI Sci. Rep. 2016, 212 (2017) DOI: `10.15120/GR-2017-1`.

DANKSAGUNG

Zuerst möchte ich Prof. Dr. Andreas Zilges für die Möglichkeit bedanken, diese Dissertation in seiner Arbeitsgruppe anzufertigen. Ich schätze die Arbeitsatmosphäre in der Gruppe, die Vielzahl an Konferenzen und insbesondere die Experimente in Deutschland und Japan sehr.

Ich möchte mich außerdem bei Prof. Dr. Ströher für die Übernahme des Korreferats sowie bei Prof. Dr. Saur für den Prüfungskommissionsvorsitz bedanken.

Allen ehemaligen und aktuellen Mitgliedern der Arbeitsgruppe Zilges möchte ich für die gute Zusammenarbeit danken. Insbesondere danke ich hier Dr. Lars Netterdon, Philipp Scholz und Felix Heim, ohne die die vielen Experimente an HORUS nicht möglich gewesen wären. Außerdem danke ich Dr. Mark Spieker, Dr. Andreas Hennig, Simon Glynn Pickstone, Michael Weinert, Sarah Prill und Miriam Müscher für die Experimente, Datenaufnahme und -analyse mit SONIC. Diese Projekte beruhen auf den Arbeiten von Dr. Janis Endres, Dr. Anne Endres, Dr. Vera Derya und Dr. Michael Elvers, denen dafür ebenso mein Dank gebührt.

Die meisten Mitglieder der AG Zilges haben mich mindestens einmal, meistens öfter, zum NeuLAND-Bauen am GSI begleitet. Ohne diese Hilfe wäre der Detektor sicherlich nicht einsatzfähig. Hier danke ich, neben den oben bereits genannten Personen, insbesondere auch Julius Wilhelmy, Michelle Färber und Elena Hoemann für ihren Einsatz.

Micheal Weinert, Elena Hoemann, Dr. Nigel Warr, Nima Saed-Samii und Nils Bruch danke ich weiterhin auch für Ihre Unterstützung meiner Softwareprojekte.

Mein Dank gebührt an dieser Stelle auch Dr. Christoph Fransen, Claus Müller-Gatermann und den Beschleunigeroperateuren sowie der Elektronik- und Beschleunigerwerkstatt für ihre Hilfe bei den Experimenten am HORUS Spektrometer sowie Dr. Karl-Oskar Zell und Dr. Andrey Blazhev für ihre Expertise in der Targetherstellung.

Des Weiteren danke ich dem NeuLAND-Team am GSI, allen voran Dr. Konstanze Boretzky für die vielen Diskussionen und die Organisation aller NeuLAND-Belange. Ich danke Dr. Dmytro Kresan und Christiaan Douma für die Zusammenarbeit an R3BRoot, Dr. Igor Gašparić und Dr. Michael Heil für die Beantwortung meiner vielen Fragen und Daniel Körper für die tatkräftige Unterstützung vor Ort.

Auch der Gruppe von Prof. Dr. Thomas Aumann danke ich für die Arbeit an NeuLAND. Insbesondere danke ich Julian Kahlbow für die Analyse von NeuLAND@SAMURAI, sowie Vadim Wagner für seine Beiträge zu R3BRoot und der Zusammenarbeit in Japan.

ERKLÄRUNG

Ich versichere, dass ich die von mir vorgelegte Dissertation selbständig angefertigt, die benutzten Quellen und Hilfsmittel vollständig angegeben und die Stellen der Arbeit – einschließlich Tabellen, Karten und Abbildungen –, die anderen Werken im Wortlaut oder dem Sinn nach entnommen sind, in jedem Einzelfall als Entlehnung kenntlich gemacht habe; dass diese Dissertation noch keiner anderen Fakultät oder Universität zur Prüfung vorgelegen hat; dass sie – abgesehen von unten angegebenen Teilpublikationen – noch nicht veröffentlicht worden ist, sowie, dass ich eine solche Veröffentlichung vor Abschluss des Promotionsverfahrens nicht vornehmen werde. Die Bestimmungen der Promotionsordnung sind mir bekannt. Die von mir vorgelegte Dissertation ist von Prof. Dr. Andreas Zilges betreut worden.

Teile dieser Arbeit wurden bereits veröffentlicht:

J. Mayer et al., "Partial cross sections of the ^{92}Mo(p,γ) reaction and the γ strength in ^{93}Tc," Phys. Rev. C **93**, 045809 (2016) DOI: `10.1103/PhysRevC.93.045809`

J. Mayer et al., "Neutron reconstruction with NeuLAND in FAIR Phase 0," GSI Sci. Rep. 2016, 212 (2017) DOI: `10.15120/GR-2017-1`

J. Kahlbow et al., "Experimental campaign using the NeuLAND demonstrator at SAMURAI," GSI Sci. Rep. 2017, in press

Köln, im August 2018